Title

Neutrino flavor transformation in core-collapse supernovae

Permalink

https://escholarship.org/uc/item/9p60h8bw

Authors

Cherry, John F.
Cherry, John F.

Publication Date

2012

UNIVERSITY OF CALIFORNIA, SAN DIEGO

Neutrino Flavor Transformation in Core-Collapse Supernovae

A dissertation submitted in partial satisfaction of the
requirements for the degree
Doctor of Philosophy

in

Physics

by

John F. Cherry Jr.

Committee in charge:

Professor George M. Fuller, Chair
Professor Bruce Driver
Professor Brian Keating
Professor Michael Norman
Professor Nolan Wallach

2012

The dissertation of John F. Cherry Jr. is approved, and it is acceptable in quality and form for publication on microfilm and electronically:

Chair

University of California, San Diego

2012

DEDICATION

To my parents, who made this all possible.

EPIGRAPH

Codeine... bourbon.
—Tallulah Bankhead

TABLE OF CONTENTS

Signature Page iii

Dedication iv

Epigraph v

Table of Contents vi

List of Figures viii

List of Tables xvii

Acknowledgements xviii

Vita and Publications xix

Abstract of the Dissertation xx

Chapter 1 Neutrinos in Supernovae 1
- 1.1 The Engine of the Explosion 1

Chapter 2 Neutrino Flavor Transformation 6
- 2.1 Neutrino Masses and Mixing 6
- 2.2 Neutrinos in Vacuum 8
- 2.3 Schrödinger-like Formalism 10
- 2.4 Isospin Formalism 12

Chapter 3 Simulation Methodology 15
- 3.1 Physical Setup 16
- 3.2 Theory of Calculation 20
- 3.3 Integration Algorithm 22

Chapter 4 Core-Collapse Supernovae 26
- 4.1 Introduction 26
- 4.2 Neutronization Burst Signal 32
  - 4.2.1 Overview 33
  - 4.2.2 Sensitivity to Neutrino Mass-Squared Differences 39
  - 4.2.3 Variation of θ_{13} 41
- 4.3 Density Fluctuation Effects 45
  - 4.3.1 Neutrino Flavor Transformation With and Without Matter Fluctuations 46
  - 4.3.2 Theory 52

4.3.3 Analysis 59
4.4 Luminosity Variation Effects 69
4.4.1 Analysis of Flavor Evolution of the ν_e's 69
4.4.2 Dependence on L_ν 70
4.4.3 Spectral Swap Formation 74
4.4.4 Expected Signal 76

Chapter 5 The Neutrino Halo 89
5.1 Issues with Neutrino Scattering 89
5.1.1 Direction Changing Scattering 89
5.1.2 The Safety Criterion 91
5.1.3 Implicit Calculation of the Halo 94
5.2 Flavor Transformation During the Accretion and SASI phases 99
5.2.1 Flavor Transformation is now a Boundary Value Problem 100
5.2.2 Multi-dimensionality 101
5.2.3 Multi-composition 103
5.2.4 Dispersion and Interference 104
5.2.5 Compounding Unknowns 105

Bibliography 110

LIST OF FIGURES

Figure 2.1: The precession of NFIS $\mathbf{s}_{\mathrm{i}}$ about the effective external field $\mathbf{H}_{\mathrm{i}}$. 14

Figure 3.1: A cartoon illustration of the neutrino emission from the surface of a protoneutron star. Neutrinos emerge from the neutrinosphere, a hard spherical shell with radius R_ν. The neutrino emission trajectories are characterized by ϑ, the angle relative to the normal of the neutrinosphere surface at the location where they are emitted. Both neutrinos i and j stream outward until their trajectories intersect at a distance r from the center of the protoneutron star, with intersection angle θ_{ij}. This intersection angle sets the strength of the neutrino-neutrino neutral current forward scattering interaction that these neutrinos both experience at this location. 17

Figure 4.1: Left panel: electron neutrino survival probability $P_{\nu_{\mathrm{e}}\nu_{\mathrm{e}}}$ (color/shading key at top left) for the inverted mass hierarchy is shown as a function of cosine of emission angle, $\cos\vartheta_{\mathrm{R}}$, and neutrino energy, E in MeV, plotted at a radius of $r = 5000\,\mathrm{km}$. Right: mass basis (key top right, inset) emission angle-averaged neutrino energy distribution functions versus neutrino energy, E. The dashed curve gives the initial ν_{e} emission angle-averaged energy spectrum. Movies of this simulation can be found at the URL in Ref. [1]. Each frame of the movie shows a representation of the neutrino survival probability in various different bases at a fixed radius above the core. Each successive frame is 1 km further out from the initial radius of $r_{\mathrm{init}} = 900\,\mathrm{km}$ out to the final radius $r = 5000\,\mathrm{km}$. 35

Figure 4.2: Emission angle-averaged neutrino energy distribution functions versus neutrino energy plotted in the neutrino mass basis for the 3 × 3 multi-angle calculation of neutrino flavor evolution. Results shown at a radius of $r = 5000\mathrm{km}$. In this simulation, a small (10%) admixture of all other species of neutrinos and anti-neutrinos are included. 36

Figure 4.3: Left panel: electron neutrino survival probability $P_{\nu_{\rm e}\nu_{\rm e}}$ (color/shading key at top left) for the normal mass hierarchy is shown as a function of cosine of emission angle, $\cos\vartheta_{\rm R}$, and neutrino energy, E in MeV, plotted at a radius of $r = 5000\,{\rm km}$. Right: mass basis (key top right, inset) emission angle-averaged neutrino energy distribution functions versus neutrino energy, E. The dashed curve gives the initial $\nu_{\rm e}$ emission angle-averaged energy spectrum. Movies of this simulation can be found at the URL in Ref. [1]. Each frame of the movie shows a representation of the neutrino survival probability in various different bases at a fixed radius above the core. Each successive frame is 1 km further out from the initial radius of $r_{\rm init} = 900\,{\rm km}$ out to the final radius $r = 5000\,{\rm km}$. 37

Figure 4.4: This calculation of the flavor evolution of neutrinos in the inverted mass hierarchy was conducted with values of $\Delta m^2_\odot = 7.6 \times 10^{-5}\,{\rm eV}^2$ and $\Delta m^2_{\rm atm} = -2.4 \times 10^{-3}\,{\rm eV}^2$. Left panel: electron neutrino survival probability $P_{\nu_{\rm e}\nu_{\rm e}}$ (color/shading key at top left) for the inverted mass hierarchy is shown as a function of cosine of emission angle, $\cos\vartheta_{\rm R}$, and neutrino energy, E in MeV, plotted at a radius of $r = 5000\,{\rm km}$. Right: mass basis (key top right, inset) emission angle-averaged neutrino energy distribution functions versus neutrino energy, E. The dashed curve gives the initial $\nu_{\rm e}$ emission angle-averaged energy spectrum. 39

Figure 4.5: This calculation of the flavor evolution of neutrinos in the normal mass hierarchy was conducted with values of $\Delta m^2_\odot = 7.6 \times 10^{-5}\,{\rm eV}^2$ and $\Delta m^2_{\rm atm} = 2.4 \times 10^{-3}\,{\rm eV}^2$. Left panel: electron neutrino survival probability $P_{\nu_{\rm e}\nu_{\rm e}}$ (color/shading key at top left) for the normal mass hierarchy is shown as a function of cosine of emission angle, $\cos\vartheta_{\rm R}$, and neutrino energy, E in MeV, plotted at a radius of $r = 5000\,{\rm km}$. Right: mass basis (key top right, inset) emission angle-averaged neutrino energy distribution functions versus neutrino energy, E. The dashed curve gives the initial $\nu_{\rm e}$ emission angle-averaged energy spectrum. . . 40

Figure 4.6: Emission angle-averaged electron neutrino flux Φ_ν (key top right, inset) for the normal neutrino mass hierarchy is shown as a function of neutrino energy E in MeV. The dashed curve gives the initial $\nu_{\rm e}$ emission angle-averaged neutrino flux. The shaded region gives the predicted flux in a single-angle calculation, and the thick line shows the flux predicted by the multi-angle calculation. These calculations of electron neutrino flux are done using $\Delta m^2_\odot = 7.6 \times 10^{-5}\,{\rm eV}^2$ and $\Delta m^2_{\rm atm} = -2.4 \times 10^{-3}\,{\rm eV}^2$ and $\theta_{13} = 0.1$. 42

Figure 4.7: Emission angle-averaged electron neutrino flux Φ_ν (key top right, inset) for the inverted neutrino mass hierarchy is shown as a function of neutrino energy E in MeV. The dashed curve gives the initial ν_{e} emission angle-averaged neutrino flux. The shaded region gives the predicted flux in a single-angle calculation, and the thick line shows the flux predicted by the multi-angle calculation. These calculations of electron neutrino flux are done using $\Delta m^2_\odot = 7.6 \times 10^{-5}\,\mathrm{eV}^2$ and $\Delta m^2_{\mathrm{atm}} = -2.4 \times 10^{-3}\,\mathrm{eV}^2$ and $\theta_{13} = 0.1$. 43

Figure 4.8: Emission angle-averaged neutrino energy distribution functions versus neutrino energy plotted in the neutrino mass basis for the 3×3 multi-angle calculation of neutrino flavor evolution. This calculation employs a significantly reduced value of $\theta_{13} = 1.0 \times 10^{-3}$. This mixing angle is associated with flavor transformation at the $\Delta m^2_{\mathrm{atm}}$ scale. Results shown at a radius of $r = 5000$km. . 44

Figure 4.9: The electron number density for two matter profiles plotted as functions of radius in the resonance region for the $\Delta m^2_{\mathrm{atm}}$ mass state splitting. The solid line indicates the original matter density profile of Refs. [2, 3], called Bump. The dashed-dotted line indicates the artificial density profile with the bump artificially removed, called No Bump. 48

Figure 4.10: The scale height of the neutrino-electron forward scattering potential evaluated at the MSW resonance location for each neutrino energy. The solid line indicates the first MSW resonance scale height of neutrinos moving through the original matter density profile of Refs. [2, 3], while the dashed line indicates the scale heights of the multiple resonances. The dash-dotted line indicates the MSW resonance scale heights of neutrinos moving through the No Bump density profile. 49

Figure 4.11: Bump. Left panel: electron neutrino survival probability $P_{\nu_{\mathrm{e}}\nu_{\mathrm{e}}}$ (color/shading key at top left) for the normal mass hierarchy is shown as a function of cosine of emission angle, $\cos\vartheta_{\mathrm{R}}$, and neutrino energy, E in MeV, plotted at a radius of $r = 5000\,\mathrm{km}$. Right: mass basis (key top right, inset) emission angle-averaged neutrino energy distribution functions versus neutrino energy, E. The dashed curve gives the initial ν_{e} emission angle-averaged energy spectrum. A kink in the density profile used, taken from Refs. [2, 3], leads to multiple MSW resonances for low energy neutrinos. 50

Figure 4.12: No Bump. Left panel: electron neutrino survival probability $P_{\nu_e \nu_e}$ (color/shading key at top left) for the normal mass hierarchy is shown as a function of cosine of emission angle, $\cos\vartheta_R$, and neutrino energy, E in MeV, plotted at a radius of $r = 5000\,\mathrm{km}$. Right: mass basis (key top right, inset) emission angle-averaged neutrino energy distribution functions versus neutrino energy, E. The dashed curve gives the initial ν_e emission angle-averaged energy spectrum. The kink in the density profile taken from Refs. [2, 3], has been artificially removed from the density profile used in this simulation. 51

Figure 4.13: The electron neutrino survival probability as a function of neutrino energy shown at the final radius $r = 5000\,\mathrm{km}$. The solid line indicates the survival probability for neutrinos after moving through the Bump profile, while the dashed line indicates the survival probability for neutrinos after moving through the No Bump profile. 52

Figure 4.14: Left panel: the combined matter and neutrino self-coupling forward scattering potentials experienced by radially emitted neutrinos as a function of radius. Right: the combined matter and neutrino self-coupling forward scattering potentials experienced by tangentially emitted neutrinos as a function of radius. The dotted and dashed-dotted lines indicate the upper and lower neutrino energies, respectively, to experience multiple neutrino-background enhanced MSW resonances in the desynchronized limit. 55

Figure 4.15: Bump: The opening angle α between the collective NFIS and $\mathbf{H}_{\mathrm{MSW}}$ for the Bump profile, plotted as a function of $|\mathbf{H}_{\mathrm{MSW}}| / |\mathbf{H}_{\mathrm{v}}|$ as the system moves through resonance. The idealized NFIS (dotted-dashed line) shows the evolution of $\mathbf{S}^{(0)}$ in the absence of any neutrino self-coupling. The solid line and dashed line show the evolution of $\mathbf{S}$ as calculated in multi-angle and single-angle simulations respectively, including the neutrino self-coupling potentials. The dotted line shows the evolution of $\mathbf{S}$ as calculated for a neutronization burst with $L_\nu \approx 0.1\,L_{\nu_e}$ for all neutrino species other than ν_e. Note that the qualitative behavior of $\mathbf{S}$ for the mutli-angle, single-angle, and mixed flux treatments are quite similar. 61

Figure 4.16: No Bump: The opening angle α between the collective NFIS and $\mathbf{H}_{\mathrm{MSW}}$ for the No Bump profile, plotted as a function of $|\mathbf{H}_{\mathrm{MSW}}| \,/\, |\mathbf{H}_{\mathrm{v}}|$ as the system moves through resonance. The idealized NFIS (dotted-dashed line) shows the evolution of $\mathbf{S}^{(0)}$ in the absence of any neutrino self-coupling. The solid line and dashed line show the evolution of $\mathbf{S}^{(0)}$ as calculated in multi-angle and single-angle simulations respectively, including the neutrino self-coupling potentials. The dotted line shows the evolution of $\mathbf{S}$ as calculated for a neutronization burst with $L_\nu \approx 0.1\, L_{\nu_{\mathrm{e}}}$ for all neutrino species other than ν_{e}. Note that the qualitative behavior of $\mathbf{S}$ for the mutli-angle, single-angle, and mixed flux treatments are quite similar. 62

Figure 4.17: The average alignment of individual neutrino polarization vectors, $\mathbf{s}_\omega$, with the collective polarization vector, $\mathbf{S}$. The solid black line shows the "Bump" profile from Refs. [2, 3] and the dotted red line shows the modified "No Bump" profile. The shaded region indicates the physical position of the Helium burning shell density feature present in the Bump profile. . . . 64

Figure 4.18: No Bump: The precession of the collective polarization vector, $\mathbf{S}$, and the zeroth order effective field $\mathbf{S}^{(0)}$, about the $\hat{\mathbf{e}}^{\mathrm{f}}_{\mathrm{z}}$ axis as neutrinos move through resonance in the No Bump profile. The solid line shows the azimuthal angle, $\phi_{\mathbf{S}}$, for the collective polarization vector $\mathbf{S}$. The dashed-dotted line shows the azimuthal angle, $\phi_{\mathbf{S}^{(0)}}$, for the zeroth order effective field $\mathbf{S}^{(0)}$. The dotted line shows the value of θ_{m} for $\mathbf{S}$ and $\mathbf{S}^{(0)}$ for reference, with a diamond symbol located at $\theta_{\mathrm{m}} = \pi/4$ where the system is at resonance. 65

Figure 4.19: Bump: The precession of the collective polarization vector, $\mathbf{S}$, and the zeroth order effective field $\mathbf{S}^{(0)}$, about the $\hat{\mathbf{e}}^{\mathrm{f}}_{\mathrm{z}}$ axis as neutrinos move through resonance in the Bump profile. The solid line shows the azimuthal angle, $\phi_{\mathbf{S}}$, for the collective polarization vector $\mathbf{S}$. The dashed-dotted line shows the azimuthal angle, $\phi_{\mathbf{S}^{(0)}}$, for the zeroth order effective field $\mathbf{S}^{(0)}$. The dotted line shows the value of θ_{m} for $\mathbf{S}$ and $\mathbf{S}^{(0)}$ for reference, with a diamond symbol located at $\theta_{\mathrm{m}} = \pi/4$ where the system is at resonance. The shaded region indicates the physical position of the Helium burning shell density feature present in the Bump profile. 66

Figure 4.20: The final neutrino mass state emission energy spectra for calculations of the flavor transformation in the neutronization neutrino burst of an O-Ne-Mg core-collapse supernova. Each panel shows the results for a different possible burst luminosity, ranging from $L_\nu = 10^{54} - 10^{52}\,\mathrm{erg\,s^{-1}}$, with identical Fermi-Dirac energy distributions. 80
Figure 4.21: The probability for electron neutrinos in the neutronization neutrino burst of an O-Ne-Mg core-collapse supernova to hop out of the (initial) heavy mass eigenstate, $1 - P_{\mathrm{H}}$, plotted as a function of inverse neutrino energy. Each panel shows the results for a different possible burst luminosity, ranging from $L_\nu = 10^{54} - 10^{52}\,\mathrm{erg\,s^{-1}}$, with identical Fermi-Dirac energy distributions. 81
Figure 4.22: High luminosity evolution ($L_0 = 10^{53}\,\mathrm{erg\,s^{-1}}$): The opening angle α between the collective NFIS $\mathbf{S}^{(0)}$ and $\mathbf{H}_{\mathrm{MSW}}$, plotted as a function of $|\mathbf{H}_{\mathrm{MSW}}|\,/\,|\mathbf{H}_{\mathrm{v}}|$ as the system moves through resonance. The idealized NFIS (solid line) shows the evolution of $\mathbf{S}^{(0)}$ in the ideal, strong neutrino self-coupling case. The dashed line, dot-dashed line, and dotted line show the evolution of $\mathbf{S}$ as calculated for neutrino luminosities $10L_0$, $\sqrt{10}L_0$, and L_0 respectively. 82
Figure 4.23: Moderate luminosity evolution ($L_0 = 10^{53}\,\mathrm{erg\,s^{-1}}$): The opening angle α between the collective NFIS $\mathbf{S}^{(0)}$ and $\mathbf{H}_{\mathrm{MSW}}$, plotted as a function of $|\mathbf{H}_{\mathrm{MSW}}|\,/\,|\mathbf{H}_{\mathrm{v}}|$ as the system moves through resonance. The idealized NFIS (solid line) shows the evolution of $\mathbf{S}^{(0)}$ in the ideal, strong neutrino self-coupling case. The dashed line, dot-dashed line, and dotted line show the evolution of $\mathbf{S}$ as calculated for neutrino luminosities L_0, $0.8\,L_0$, and $0.6\,\mathrm{L}_0$ respectively. 83
Figure 4.24: Low luminosity evolution ($L_0 = 10^{53}\,\mathrm{erg\,s^{-1}}$): The opening angle α between the collective NFIS $\mathbf{S}^{(0)}$ and $\mathbf{H}_{\mathrm{MSW}}$, plotted as a function of $|\mathbf{H}_{\mathrm{MSW}}|\,/\,|\mathbf{H}_{\mathrm{v}}|$ as the system moves through resonance. The idealized NFIS (solid line) shows the evolution of $\mathbf{S}^{(0)}$ in the ideal, strong neutrino self-coupling case. The dashed line, dot-dashed line, and dotted line show the evolution of $\mathbf{S}$ as calculated for neutrino luminosities $0.4\,L_0$, $10^{-1/2}\,L_0$, and $10^{-1}\,\mathrm{L}_0$ respectively. 84

Figure 4.25: The expected signal from the neutronization burst of Ref. [4], in the normal neutrino mass hierarchy, created by integrating the final emission angle averaged neutrino spectral energy distribution and fluxes over the first 30 ms of the neutrino burst signal. Left: Scaled neutrino number flux, summed over all neutrino flavors, shown in the vacuum mass basis. Right: Scaled antineutrino number flux, summed over all neutrino flavors, shown in the vacuum mass basis. 85
Figure 4.26: The expected signal from the neutronization burst of Ref. [5], in the normal neutrino mass hierarchy, created by integrating the final emission angle averaged neutrino spectral energy distribution and fluxes over the first 30 ms of the neutrino burst signal. Left: Scaled neutrino number flux, summed over all neutrino flavors, shown in the vacuum mass basis. Right: Scaled antineutrino number flux, summed over all neutrino flavors, shown in the vacuum mass basis. 85
Figure 4.27: The expected signal from the neutronization burst of Ref. [4], in the inverted neutrino mass hierarchy, created by integrating the final emission angle averaged neutrino spectral energy distribution and fluxes over the first 30 ms of the neutrino burst signal. Left: Scaled neutrino number flux, summed over all neutrino flavors, shown in the vacuum mass basis. Right: Scaled antineutrino number flux, summed over all neutrino flavors, shown in the vacuum mass basis. 86
Figure 4.28: The expected signal from the neutronization burst of Ref. [5], in the inverted neutrino mass hierarchy, created by integrating the final emission angle averaged neutrino spectral energy distribution and fluxes over the first 30 ms of the neutrino burst signal. Left: Scaled neutrino number flux, summed over all neutrino flavors, shown in the vacuum mass basis. Right: Scaled antineutrino number flux, summed over all neutrino flavors, shown in the vacuum mass basis. 86
Figure 4.29: The expected signal from the neutronization burst of Ref. [4], in the normal neutrino mass hierarchy, created by integrating the final emission angle averaged neutrino spectral energy distribution and fluxes over the first 30 ms of the neutrino burst signal. Left: Scaled neutrino number flux, summed over all neutrino flavors, shown in the neutrino flavor basis. Right: Scaled antineutrino number flux, summed over all neutrino flavors, shown in the neutrino flavor basis. 87

Figure 4.30: The expected signal from the neutronization burst of Ref. [5], in the normal neutrino mass hierarchy, created by integrating the final emission angle averaged neutrino spectral energy distribution and fluxes over the first 30 ms of the neutrino burst signal. Left: Scaled neutrino number flux, summed over all neutrino flavors, shown in the neutrino flavor basis. Right: Scaled antineutrino number flux, summed over all neutrino flavors, shown in the neutrino flavor basis. 87
Figure 4.31: The expected signal from the neutronization burst of Ref. [4], in the inverted neutrino mass hierarchy, created by integrating the final emission angle averaged neutrino spectral energy distribution and fluxes over the first 30 ms of the neutrino burst signal. Left: Scaled neutrino number flux, summed over all neutrino flavors, shown in the neutrino flavor basis. Right: Scaled antineutrino number flux, summed over all neutrino flavors, shown in the neutrino flavor basis. 88
Figure 4.32: The expected signal from the neutronization burst of Ref. [5], in the inverted neutrino mass hierarchy, created by integrating the final emission angle averaged neutrino spectral energy distribution and fluxes over the first 30 ms of the neutrino burst signal. Left: Scaled neutrino number flux, summed over all neutrino flavors, shown in the neutrino flavor basis. Right: Scaled antineutrino number flux, summed over all neutrino flavors, shown in the neutrino flavor basis. 88

Figure 5.1: Supernova neutrino emission geometry. 90
Figure 5.2: Solid lines show matter density profiles and dashed lines the corresponding Neutrino Bulb (1 %) safety criteria from Eq. 5.2. Black lines are for the late-time neutrino driven wind environment [6], green lines the neutronization burst O-Ne-Mg core-collapse environment [2, 3], and red lines the Fe-core-collapse shock revival environment [7]. 93
Figure 5.3: Left: Color scale indicates the density within the shock front in a 15 $M_\odot$ progenitor core-collapse supernova 500 ms after core bounce, during the shock revival epoch [7]. Right: Effect of the scattered neutrino halo for the matter distribution at Left. Color scale indicates the ratio of the sum of the maximum (no phase averaging) magnitudes of the constituents of the neutrino-neutrino Hamiltonian, $|\hat{H}_{\nu\nu}^{\mathrm{bulb}}|+|\hat{H}_{\nu\nu}^{\mathrm{halo}}|$, to the contribution from the neutrinosphere $|\hat{H}_{\nu\nu}^{\mathrm{bulb}}|$. 95

Figure 5.4: Fractional contribution of inward directed neutrinos (dashed line) and outward directed neutrinos (solid line) to the magnitude of the halo neutrino potential $|\mathbf{H}_{\nu\nu}^{\text{halo}}|$ at fixed radius, using the density profile and neutrino emission spectra of Ref. [8]. . . 102
Figure 5.5: (Color Online) The isosurfaces for $\kappa r \geq 1$ using the density profile (shown in black) and neutrino emission spectra of Ref. [8]. The halo neutrinos originating inside the current radial coordinate are considered to be co-evolving with neutrinos from the core. Red: $\langle A \rangle = 56$, Blood Orange: $\langle A \rangle = 28$, Orange: $\langle A \rangle = 12$, Tangerine: $\langle A \rangle = 4$, Yellow: $\langle A \rangle = 1$, Green: $\langle A \rangle = 1$ with no halo neutrinos propagating backwards in radial coordinate, Blue: no halo potential. 106

LIST OF TABLES

Table 5.1: The conditions under which dispersion from the neutrino halo and dispersion from the bulb neutrinos will interfere constructively or destructively. Note that the neutrino emission spectra of Ref. [8] lies in the upper right box. 105

Table 5.2: The conditions under which dispersion from the neutrino halo and dispersion from the matter potential will interfere constructively or destructively. Note that the neutrino emission spectra and matter potential of Ref. [8] lies in the upper right box. . . . 105

ACKNOWLEDGEMENTS

It has been a long (occasionally bumpy) road to the completion of my Ph.D. thesis, and there are a great many people who have touched my life and my career who deserve my thanks for their support. Chief among them is my advisor, Professor George Fuller, whose careful guidance and wisdom has taught me the difference between solving physics problems, and thinking *physically* about the universe. It was George's guidance that taught me everything from how to search for interesting problems, conduct my basic research, how to craft my papers and communicate my ideas, to navigating the politically and socially thorny landscape of modern science. Thank you, George, it is the legacy of your teachings that I will carry with me throughout my career, and I hope that I make you proud.

I would like to thank my collaborators and co-authors at Los Alamos National Laboratory, Joe Carlson and Alex Friedland. Joe, in particular, is the original author of the neutrino flavor transformation code that I have spent so much time working with. Without his help and insight, I never would have gotten my flavor transformation project off of the ground. Alex's input on the Neutrino Halo papers has been crucial, and his brilliance and attention to detail has made diamonds out of the lumps of coal that I initially wrote.

A great deal of thanks is also owed to several more of my co-authors: Huaiyu Duan, of the University of New Mexico, Albuquerque; Yong-Zhong Qian, of the University of Minnesota, Minneapolis; and Meng-Ru Wu, also of the University of Minnesota, Minneapolis. They have each contributed mightily to supporting and guiding my research, and now with the publication of this thesis, to our understanding of the O-Ne-Mg core-collapse neutronization neutrino burst signal.

Much thanks also goes to my fellow graduate students Chad Kishimoto, Wendel Misch, Rick Wagner, and Alexey Vlasenko, who is also a co-author of mine. They have all been an indispensable help answering my questions, playing foil to my crazy ideas, challenging my notions of physics with their own crazy ideas, and the quite serious business of drinking beer.

I am grateful to my parents, who have supported me through thick and thin my entire life. I love you both. This Ph.D. thesis is dedicated to you.

Chapter 4, in part, is a reprint of material has appeared in Physical Review D, 2010-2012. Cherry, J. F., Wu, M.-R., Carlson, J., Duan, H., Fuller, G. M., and Qian, Y.-Z., the American Physical Society, 2010-2012. The dissertation author was the primary investigator and author of these papers.

Chapter 5, in part, is a reprint of material has appeared in Physical Review Letters, 2012 and material that will be shortly submitted to Physical Review D, 2012. Cherry, J. F.; Carlson, J.; Friedland, A.; Fuller, G. M.; Vlasenko, A., the American Physical Society, 2012. The dissertation author was the primary investigator and author of these papers.

VITA

2003	B. S. in Physics, University of California, San Diego
2003-2005	Product Engineer, Quantum Design, San Diego
2005-2006	Graduate Teaching Assistant, University of California, San Diego
2006-2012	Graduate Student Researcher, University of California, San Diego
2005-2012	Ph. D. in Physics, University of California, San Diego

PUBLICATIONS

Cherry, J. F., Fuller, G. M., Carlson, J., Duan, H., and Qian, Y.-Z.,
“Multi-Angle Simulation of Flavor Evolution in the Neutronization Neutrino Burst from an O-Ne-Mg Core-Collapse Supernova,”
Phys. Rev. D **82**, 085025 (2010).
[arXiv:astro-ph.HE/1006.2175]

Cherry, J. F., Wu, M.-R., Carlson, J., Duan, H., Fuller, G. M., and Qian, Y.-Z.,
“Density Fluctuation Effects on Collective Neutrino Oscillations in O-Ne-Mg Core-Collapse Supernovae, ”
Phys. Rev. D **84**, 105034 (2011).
[arXiv:astro-ph.HE/1108.4064]

Cherry, J. F., Wu, M.-R., Carlson, J., Duan, H., Fuller, G. M., and Qian, Y.-Z.,
“Neutrino Luminosity and Matter-Induced Modification of Collective Neutrino Flavor Oscillations in Supernovae, ”
Phys. Rev. D **In press** (2012).
[arXiv:astro-ph.HE/1109.5195]

Cherry, J. F., Carlson, J., Friedland, A., Fuller, G. M., Vlasenko, A.,
“Neutrino scattering and flavor transformation in supernovae, ”
Phys. Rev. Let. **In press** (2012).
[arXiv:astro-ph.HE/1203.1607]

Cherry, J. F., Carlson, J., Friedland, A., Fuller, G. M., Vlasenko, A.,
“On the efficacy of the linearized stability analysis, ”
Phys. Rev. D **Pre-print** (2012).

ABSTRACT OF THE DISSERTATION

Neutrino Flavor Transformation in Core-Collapse Supernovae

by

John F. Cherry Jr.

Doctor of Philosophy in Physics

University of California, San Diego, 2012

Professor George M. Fuller, Chair

Ever since a collection of 19 flickers of Cherenkov radiation in neutrino detectors around the world have been linked to SN 1987a, the physics community has been certain that neutrinos are the pivotal actors in core-collapse supernovae. SN1987a confirmed Jim Wilson and Sterling Colgate's basic picture of the collapsed core of a massive star shining with neutrinos of all kinds, radiating with a luminosity of $10^{53}\,\mathrm{erg\ s^{-1}}$. At a stroke neutrinos provided a mechanism by which nature could explode an object as massive as a star and produce the heavy elements that we find all around us. Like all great discoveries, however, the neutrino burst of SN 1987a raised more questions than it answered. Neutrinos are known to change their lepton flavor as a purely quantum mechanical process in vacuum and in the sun and the earth, and our experimental knowledge of this process leads us

to an inexorable conclusion: neutrinos will change their flavor states in supernovae, as well.

One of the most deucedly difficult problems in neutrino astrophysics for the last few decades has been the question of how neutrino flavor transforms in the supernova environment. The intense flux of neutrinos from the core of a supernova is so numerous that the interactions of neutrinos with one another is strong enough to create a quantum mechanical coupling of their flavor evolution histories, so that the flavor states of all neutrinos are non-linearly related to one another. This non-linear coupling of neutrino flavor states can have fascinating consequences, leading to collective flavor transformation phenomena, where all neutrinos emerging from the core begin to change flavor simultaneously. The dynamics of these non-linear effects can provide great insight into as yet unconstrained sectors of neutrino physics. Likewise, should the details of neutrino flavor mixing be worked out before the next galactic supernova, the understanding of neutrino flavor transformation might act as a neutrino telescope, allowing an observer to probe the depths of an exploding star.

However, supernovae are environments that test the limits of our physical understanding. A cherished paradigm within the supernova neutrino community, the “neutrino bulb” model, has been found to be critically flawed early in the explosion. The collapsed core is not the only source of neutrinos which are *important* for flavor transformation. The early epochs of supernovae posses a “halo” of neutrinos, which have scattered inwards from the outer reaches of the explosion envelope. These halo neutrinos carry with them quantum information about the flavor transformation that has transpired elsewhere in the star, and can dominate the flavor evolution of neutrinos emerging from the core. This alters the fundamental nature of the problem of neutrino flavor transformation in supernovae, and will require all new approaches to address.

Chapter 1

Neutrinos in Supernovae

1.1 The Engine of the Explosion

For more than thirty years it has been strongly suspected that neutrinos are the engine that drives the explosion of core-collapse supernovae [9, 10, 11]. Direct observation of neutrinos from Supernova 1987a validated the general features of this picture of the supernova explosion mechanism. Due to the tremendous complexity of the supernova environment it has only been within the last decade that a clear picture has emerged of how the explosion is ultimately achieved [12]. While the details of the decades of research that have lead to the current understanding of the core-collapse supernova explosion could scarcely be fit into this introduction, there is a brief back-of-the-envelope style calculation which will swiftly reveal why neutrinos, which interact so very weakly with matter, are the power house of the explosion and why it is so important that one understands their behavior in this environment.

When the core of a massive star burns its nuclear fuel to iron, it has exhausted its ability to generate more thermal energy to provide pressure support against gravitational collapse. The core is initially supported by degenerate electron pressure, which would be unstable to gravitational collapse except for a small fraction of electrons which are thermally excited above the top of the Fermi sea, which can provide slightly more pressure support [13]. As the core isothermally contracts, the Fermi energy of the degenerate electrons increases and fraction of electrons that can be excited above the top of the Fermi sea shrinks [13]. The core of the star again becomes gravitationally unstable, having reached a mass of $\sim 1.4\, M_\odot$ and a radius of $\sim R_\oplus$, and collapses in free fall for about $\sim 1\, s$ to an proto-neutrino star (PNS) which is (a few) $\times 10\,\mathrm{km}$ in radius [13].

The inner ($\sim 0.8\, M_\odot$) portion of the core stops suddenly when the density reaches slightly more than nuclear density, $\rho \approx 2.5 \times 10^{14}\,\mathrm{g\ cm^{-3}}$, and neutron degeneracy pressure swiftly overwhelms the kinetic energy of infall, which triggers a brief compression and rebound [9]. This sudden halt and rebounding of the inner core acts like a piston, launching a bounce shock that propagates outward [9].

Core-collapse supernovae are, first and foremost, the explosion of massive stars, and in order to achieve an explosion one must identify a source of energy which can gravitationally unbind the star. The characteristic unit of energy for this problem is called the "Bethe", $1\,\mathrm{B} = 10^{51}\,\mathrm{erg} = 6.24 \times 10^{56}\,\mathrm{MeV}$, which is roughly the energy required to unbind a $15\, M_\odot$ gravitationally bound star. The initial bounce shock has (a few)$\times 1\,\mathrm{B}$ energy (which can vary depending on the prescription used for the neutron star equation of state), and was initially thought to drive the explosion, but there is a complication. The initial bounce shock, like all shocks, creates a discontinuous entropy profile where the entropy spikes suddenly on the inside of the shock. This spike in entropy, from $\sim 1\, k_\mathrm{B}$/baryon pre-shock, to $\sim 10\, k_\mathrm{B}$/baryon post-shock, shifts nuclear statistical equilibrium (NSE) to favor free nucleons and alpha particles over heavy nuclei [11]. This forces the bounce shock to devote energy to dissociating heavy nuclei, and some $0.6\, M_\odot$ of iron, layers of silicon, neon and magnesium, and carbon and oxygen must be photo-dissociated. The binding energy of a single nucleon within a nucleus is $\sim 8\,\mathrm{MeV}$ per nucleon, yielding the figure that photo-dissociation of iron requires $1\,\mathrm{B}$ per $0.1\, M_\odot$, which quickly saps the energy of the bounce shock, causing it to stall at $r \sim 150\,\mathrm{km}$ [11].

This is, both literally and figuratively, the time for neutrinos to shine. There is a tremendous amount of gravitational binding energy that has been converted to thermal energy by the collapse of the core,

$$\Delta U = G M_\mathrm{core}^2 \left(\frac{1}{r_\mathrm{PNS}} - \frac{1}{R_\oplus} \right) \tag{1.1}$$

in the Newtonian limit (general relativistic corrections to this are $O\,(10\%)$). Taking the radius of the PNS to be $r_{\mathrm{PNS}} \approx 10\,\mathrm{km}$ gives the result that $\Delta U \approx 900\,\mathrm{B}$, which is a tremendous pool of thermal energy. Neutrinos became trapped within the core once the density during the collapse exceeded $\rho \sim 10^{12}\,\mathrm{g\ cm^{-3}}$ [9], and have since been in thermal equilibrium with the matter of the newly formed PNS, now at a temperature of $T \sim 10\,\mathrm{MeV}$ [9]. Because the core is at such a high temperature, neutrino pairs are produced in equilibrium via a number of weak interaction channels, such as nuclear de-excitation and positron-electron annihilation.

The newly collapsed core is an extremely hot ball of matter, and as such will begin to undergo Kelvin-Helmholtz contraction. The timescale for this contraction is set by the shortest diffusion timescale of particles trapped within the core, e.g. the core contracts at the same rate as whichever particles can diffuse out of the core the fastest, and the energy of the core is radiated at that rate. The Kelvin-Helmholtz timescale is then,

$$t_{\mathrm{KH}} = \frac{\Delta U}{L}\ , \tag{1.2}$$

where L is the luminosity of the core as it contracts.

Neutrinos in the core have relatively long mean free paths, owing to their low cross section to scatter with matter, $\sigma \approx G_{\mathrm{F}}^2 E_\nu^2$ [14], where $G_{\mathrm{F}} = 1.166 \times 10^{-11}\,\mathrm{MeV^{-2}}$ is the weak coupling constant. With neutrinos in thermal equilibrium $\langle E_\nu \rangle \sim 10\,\mathrm{MeV}$, and matter in the core as stated previously $\rho \approx 2.5 \times 10^{14}\,\mathrm{g\ cm^{-3}}$, one finds that the neutrino mean free path is,

$$l = \frac{1}{\rho\sigma} \approx 10\,\mathrm{cm}\ . \tag{1.3}$$

This macroscopic mean free path (c.f. the mean free path of photons and phonons $\sim 1\,\mathrm{fm}$) means that neutrinos can diffuse out of the core on relatively short timescales. For a random walk out of the proto-neutron star, $r_{\mathrm{PNS}} = \sqrt{N}l$, where N is the number of scatterings along the path. Again with $r_{\mathrm{PNS}} \approx 10\,\mathrm{km}$, this gives $N = 10^{10}$. Taking neutrinos to travel at the speed of light, c, the diffusion time for escaping the core will be,

$$t_{\mathrm{diff}} = \frac{Nl}{c} \approx 10\,\mathrm{s}\ . \tag{1.4}$$

The neutrino diffusion timescale is much, much shorter than any other energy transport mechanism inside the PNS. As a result, $t_{\mathrm{diff}} = t_{\mathrm{KH}}$, and the

PNS cools primarily by radiating tremendous quantities of neutrinos. Solving Equation 1.2 for the luminosity reveals that the core shines with neutrinos at a truly titanic luminosity of $L_\nu \approx 100\,\mathrm{B}\ \mathrm{s}^{-1} = 1 \times 10^{53}\,\mathrm{erg}\ \mathrm{s}^{-1}$.

It is not enough to explode the star that the PNS is intensely luminous in neutrinos, those neutrinos must interact with matter on their way out and deposit enough of their energy to revive the bounce shock and power the explosion. With the advent of multi-dimensional hydrodynamics, it was discovered that the neutrinos do, indeed, couple $\sim 1\%$ of their energy back into the supernova envelope as stream outward [15]. There are a number of processes which contribute to this energy deposition, but there are two main channels that contain the bulk of the energy deposition rate [11],

$$\nu_\mathrm{e} + n \rightarrow p^+ + e^- \tag{1.5}$$

$$\bar{\nu}_\mathrm{e} + p^+ \rightarrow n + e^+ \ . \tag{1.6}$$

However, neutrinos are famous for their ability to change their lepton "flavor" in flight. As can be seen above, the lepton flavor of the neutrinos participating in those processes is definite. Any changes in neutrino flavor states can alter the number and spectral energy distribution of the neutrinos which can participate in those two interactions. In this sense, the entire picture of the neutrino driven supernova explosion is dependent on a concrete knowledge of the neutrino flavor states within the supernova. Furthermore, the final nucleosynthesis products of the explosion depend on the neutron to proton ratio in the ejecta. These two main energy deposition channels also have the byproduct of altering the p^+/n ratio.

The entire explosion mechanism depends on diverting a small fraction of this neutrino energy into heating to drive revival of the stalled core bounce shock [16, 17, 18, 12, 19, 20, 21] creating a supernova explosion and setting the conditions for the synthesis of heavy elements [12, 22, 20, 23, 21]. However, the way neutrinos interact in this environment depends on their flavors, necessitating calculations of neutrino flavor transformation. These calculations show that neutrino flavor transformation has a rich phenomenology, including collective oscillations [24, 25, 26, 27, 28, 6, 29, 30, 31, 32, 33, 34, 35, 36, 37, 38, 39, 40, 41, 42, 43, 44, 45, 46, 47, 48, 49, 50, 51], which can affect important aspects of supernova physics

[52, 6, 29, 32, 33, 34, 35, 36, 4, 40, 41, 42, 53, 54, 44, 45, 55]. For example, neutrino-heated heavy element r-process nucleosynthesis [56, 57, 58, 59, 60] and potentially supernova energy transport above the core and the explosion itself [25, 61, 50] could be affected.

Chapter 2

Neutrino Flavor Transformation

2.1 Neutrino Masses and Mixing

Neutrino flavor oscillations in vacuum arise because the weak interaction (flavor) eigenstates for these particles $|\nu_\alpha\rangle$ are not coincident with their energy (mass) eigenstates $|\nu_\mathrm{i}\rangle$. Here $\alpha = \mathrm{e}, \mu, \tau$ and $i = 1, 2, 3$ refer to the flavor states and mass eigenvalues m_i, respectively. In vacuum the energy eigenstates are related to the flavor eigenstates by the Maki-Nakagawa-Sakata (MNS) matrix U: $|\nu_\alpha\rangle = \sum_i U^*_{\alpha\mathrm{i}} |\nu_i\rangle$; where $U_{\alpha\mathrm{i}}$ are the elements of the unitary transformation matrix. This transformation has four free parameters: three mixing angles, $\theta_{12},\ \theta_{13},\ \theta_{23}$, and a CP-violating phase δ. Each of the mixing angles defines a unitary matrix for mixing of states by that angle, U_ij, with the definition c_{ij} and s_{ij} are the cosine and sine of the appropriate mixing angle θ_{ij}. These matrices are individually given by,

$$U_{12} = \begin{pmatrix} c_{12} & s_{12} & 0 \\ -s_{12} & c_{12} & 0 \\ 0 & 0 & 1 \end{pmatrix} , \tag{2.1}$$

$$U_{13} = \begin{pmatrix} c_{13} & 0 & s_{13}e^{-i\delta} \\ 0 & 1 & 0 \\ -s_{13}e^{i\delta} & 1 & c_{13} \end{pmatrix} , \tag{2.2}$$

$$\text{and } U_{23} = \begin{pmatrix} 1 & 0 & 0 \\ 0 & c_{23} & s_{23} \\ 0 & -s_{23} & c_{23} \end{pmatrix} . \tag{2.3}$$

These individual matrices can be used to describe mixing between the neutrino flavors sharing two particular mass states, or they can be used to form the full MNS matrix is,

$$U = U_{23}U_{13}U_{12} = \begin{pmatrix} c_{12}c_{13} & s_{12}c_{13} & s_{13}e^{-i\delta} \\ -s_{12}c_{23} - c_{12}s_{13}s_{13}e^{i\delta} & c_{12}c_{23} - s_{12}s_{13}s_{13}e^{i\delta} & c_{13}s_{12} \\ s_{12}s_{23} - c_{12}s_{13}c_{13}e^{i\delta} & c_{12}s_{23} - s_{12}s_{13}c_{13}e^{i\delta} & c_{13}c_{23} \end{pmatrix} . \tag{2.4}$$

Solar, atmospheric, reactor, and accelerator neutrino experiments have measured two of these parameters: $\sin^2\theta_{12} \approx 0.32$, $\sin^2\theta_{23} \approx 0.50$ [62]. The best current experimental constraints suggest that $\sin^2 2\theta_{13} = 0.091 \pm 0.021$ (2σ error) [63]. The CP-violating phase δ remains unconstrained.

Neutrino flavor oscillation in vacuum arises because a neutrino is created in a pure flavor state by the weak interaction, and thus it is in a superposition of mass eigenstates. As the neutrino propagates through space, the different mass eigenstates build up quantum mechanical phase at different rates owing to the distinct momenta associated with each mass eigenstate for a single neutrino. For a relativistic neutrino, or any relativistic particle for that matter, the difference in momentum between two distinct mass states (setting $\hbar = c = 1$) is simply $\Delta m^2/2E$, where E is the energy of the particle and Δm^2 is the difference in the mass squared values of the two mass eigenstates.

The neutrino mass-squared differences are defined as $\Delta m^2_{\text{ij}} = m^2_{\text{i}} - m^2_j$, and as dictated by the requirement for unitarity, there are three neutrinos mass states for the three active flavors of neutrinos. So long as no two mass states are degenerate, this mandates two mass squared splittings, which have been measured. For historical reasons they are named the "solar" and "atmospheric" mass squared splittings, $\Delta m^2_{\odot}$ and Δm^2_{atm}, respectively. However, the ordering (hierarchy) of the neutrino mass-squared differences remains undetermined. There are two possible configurations for a set of three mass states with two mass-squared splittings. The "normal" mass hierarchy has the solar neutrino mass-squared split below the atmospheric split. In this case the vacuum mass states are ordered from lowest to highest as m_1, m_2, and m_3, with $\Delta m^2_\odot = m_2^2 - m_1^2$ and $\Delta m^2_{\rm atm} = m_3^2 - m_2^2$. By contrast, the "inverted" mass hierarchy is where the solar neutrino mass-squared split lies above the atmospheric split. In this scheme the vacuum mass states are ordered from lowest to highest as m_3, m_1, and m_2, with $\Delta m^2_\odot = m_2^2 - m_1^2$ and $\Delta m^2_{\rm atm} = m_1^2 - m_3^2$.

In what follows I refer to neutrino mixing at a particular point as being on the "$\Delta m^2_\odot$ scale" or "$\Delta m^2_{\rm atm}$ scale". By this it is meant that the neutrino flavor transformation at this point is taking place mostly through $\nu_{\rm e} \rightleftharpoons \nu_{\mu,\tau}$ mixing in that part of the unitary transformation corresponding to $\Delta m^2_\odot$ or $\Delta m^2_{\rm atm}$, respectively. This terminology is a holdover from the standard adiabatic MSW case, where $\Delta m^2_\odot/2E_\nu$ and $\Delta m^2_{\rm atm}/2E_\nu$ essentially pick out density regions and neutrino energies E_ν where mixing is large (i.e., MSW resonance at $\Delta m^2/2E_\nu \approx \sqrt{2}G_{\rm F}n_{\rm e}$, where $n_{\rm e}$ is the net electron number density).

2.2 Neutrinos in Vacuum

To set the stage for things to come, let's examine the evolution in a vacuum of a single neutrino with a simplified, two mass state and two lepton flavor system, say ν_1/ν_2 and $\nu_{\rm e}/\nu_\tau$. The association of the neutrino flavor states with the mass eigenstates will then be,

$$|\nu_{\rm e}\rangle = \quad \cos\theta|\nu_1\rangle + \sin\theta|\nu_2\rangle \ , \tag{2.5}$$

$$|\nu_\tau\rangle = \ -\sin\theta|\nu_1\rangle + \cos\theta|\nu_2\rangle \ , \tag{2.6}$$

where θ is the mixing angle in vacuum. A neutrino in state $|\Psi\rangle$ which is some superposition of the above states will propagate in vacuum according to the Schrödinger equation for a free particle,

$$i\frac{\partial|\Psi\rangle}{\partial t} = \hat{H}|\Psi\rangle \ . \tag{2.7}$$

The Hamiltonian operator in Equation 2.7 is the usual Hamiltonian operator for a free, relativistic particle,

$$\hat{H} = \left(\hat{p}^2 + \hat{m}^2\right)^{(1/2)} \ , \tag{2.8}$$

where $\hat{p}$ and $\hat{m}$ are the momentum and mass eigenvalue operators, respectively, defined as $\hat{p}|\nu_1\rangle = p|\nu_1\rangle$ and $\hat{m}|\nu_1\rangle = m_1|\nu_1\rangle$. In the limit that the rest masses of the neutrino states are much less than the momentum, Equation 2.8 becomes,

$$\hat{H} \approx \hat{p} + \hat{m}^2/2\hat{p}\ . \tag{2.9}$$

The eigenvalues of this Hamiltonian are defined as $\hat{H}|\nu_1\rangle = E_1|\nu_1\rangle$.

Examining the mass eigenbasis representation of our composite neutrino state, $|\Psi_{\mathrm{m}}\rangle = a|\nu_1\rangle + b|\nu_2\rangle$, one finds that Equation 2.7 is,

$$i\frac{\partial|\Psi_{\mathrm{m}}\rangle}{\partial t} = \left[\left(p + \frac{m_1^2 + m_2^2}{4p}\right)\hat{I} + \frac{\Delta m_{21}^2}{4p}\begin{pmatrix} -1 & 0 \\ 0 & 1 \end{pmatrix}\right]|\Psi_{\mathrm{m}}\rangle\ , \tag{2.10}$$

where $\hat{I}$ is the identity matrix, and the separation between diagonal and traceless portions of $\hat{H}$ has been made explicit. Solutions to Equation 2.10 are plane wave solutions of the form,

$$|\Psi\left(t\right)\rangle = \cos\theta|\nu_1\rangle e^{-\frac{i}{\hbar}E_1 t} + \sin\theta|\nu_2\rangle e^{-\frac{i}{\hbar}E_2 t}\ , \tag{2.11}$$

for a neutrino that was created in an initial state of $|\Psi\left(t = 0\right)\rangle = |\nu_{\mathrm{e}}\rangle$. The traceless portion of the Hamiltonian is crucial, as it creates a relative phase build up between the components of $|\Psi\left(t\right)\rangle$. Any source of phase which adds equally to the evolution of the components of $|\Psi\left(t\right)\rangle$ will not change the relative amplitudes of the separate pieces of the state, and thus not affect any observables. This is the reason the traceless portion of the Hamiltonian is the source of all neutrino flavor transformation.

Calculating the probability that a neutrino in state $|\Psi\left(t\right)\rangle$ will be measured in a given flavor state is now a simple matter of taking an inner product. The probability of finding our electron neutrino at some time later in a τ flavor state is,

$$P_{\nu_{\mathrm{e}}\nu_\tau} = |\langle\nu_\tau|\Psi\left(t\right)\rangle|^2 = \sin^2 2\theta \sin^2\left(\frac{\Delta m_{21}^2}{4p}t\right)\ . \tag{2.12}$$

Similarly, the probability of finding the neutrino in its initial electron flavor state is,

$$P_{\nu_{\mathrm{e}}\nu_{\mathrm{e}}} = |\langle\nu_{\mathrm{e}}|\Psi\left(t\right)\rangle|^2 = 1 - \sin^2 2\theta \sin^2\left(\frac{\Delta m_{21}^2}{4p}t\right)\ . \tag{2.13}$$

2.3 Schrödinger-like Formalism

Neutrinos can undergo flavor state oscillations in medium as well as in vacuum. The principle equations of motion which describe this flavor evolution are fundamentally similar to the example just shown for neutrino propagating in vacuum. Principally, only the traceless portions of the neutrino propagation Hamiltonians will contribute to neutrino flavor conversion. As a result, this is referred to as the Schrödinger-like formalism, because the equations of motion resemble the Schrödinger equation, with the exception that they are formally traceless, so that they do not describe the proper motion of neutrino quantum states, only the disposition of neutrino flavor state content.

For the supernova environment above a proto-neutron star, the neutrinos are nearly all free streaming, owing to the sharp decrease in neutrino optical depth just above the surface of the proto-neutron star (details of how this comes about will be provided in the relevant chapters). In this regime one can therefore neglect the contribution of inelastic neutrino scattering processes to the forward scattering of supernova neutrinos. Consequently one follows only coherent, elastic neutrino interactions. In this limit one can make the mean-field, coherent forward-scattering approximation, where neutrino flavor evolution is governed by a Schrödinger-like equation of motion [64, 24]. For example, one can represent the flavor state of neutrino i by $|\psi_{\nu,\mathrm{i}}\rangle$. As in the last section, the evolution of this flavor state in the mean field coherent limit is then

$$i\frac{\partial|\psi_{\nu,\mathrm{i}}\rangle}{\partial t} = \hat{H}|\psi_{\nu,\mathrm{i}}\rangle \tag{2.14}$$

where t is an affine parameter along neutrino i's world line and $\hat{H}$ is the appropriate flavor-changing Hamiltonian along this trajectory: $\hat{H} = \hat{H}_{\mathrm{vac}} + \hat{H}_{\mathrm{mat}} + \hat{H}_{\nu\nu}$. Here $\hat{H}_{\mathrm{vac}}$, $\hat{H}_{\mathrm{mat}}$, and $\hat{H}_{\nu\nu}$ are the vacuum, neutrino-electron/positron charged current forward exchange scattering, and neutrino-neutrino neutral current forward exchange scattering (neutrino self-coupling) contributions, respectively, to the overall Hamiltonian. In the neutrino flavor state basis, the vacuum Hamiltonian can be expressed as,

$$\hat{H}_{\rm vac} = \frac{1}{2E_\nu} \times U \begin{pmatrix} -\frac{\Delta m^2_{21}+\Delta m^2_{31}}{3} & 0 & 0 \\ 0 & \frac{2\Delta m^2_{21}-\Delta m^2_{31}}{3} & 0 \\ 0 & 0 & \frac{2\Delta m^2_{31}-\Delta m^2_{21}}{3} \end{pmatrix} U^\dagger \ , \tag{2.15}$$

for a neutrino of energy E_ν. Likewise, the neutrino-matter coherent forward scattering Hamiltonian is written in the neutrino flavor basis as,

$$\hat{H}_{\rm mat} = \begin{pmatrix} -\frac{2\sqrt{2}G_{\rm F}n_{\rm e}}{3} & 0 & 0 \\ 0 & \frac{\sqrt{2}G_{\rm F}n_{\rm e}}{3} & 0 \\ 0 & 0 & \frac{\sqrt{2}G_{\rm F}n_{\rm e}}{3} \end{pmatrix} \ , \tag{2.16}$$

where $G_{\rm F} = 1.16637 \times 10^{-11}\,{\rm MeV}^{-2}$ is Fermi's coupling constant and $n_{\rm e}$ is the local number density of electrons.

The coherent neutrino-neutrino forward exchange scattering Hamiltonian $\hat{H}_{\nu\nu}$ produces vexing nonlinear coupling of flavor histories for neutrinos on intersecting trajectories. This is the pivotal complication encountered when attempting to calculate the evolution of the supernova neutrino flavor field. Note that $\hat{H}_{\nu\nu}$ gives rise to both flavor-diagonal and off-diagonal potentials. In turn, each of these potentials is neutrino intersection angle-dependent, reflecting the $V-A$ structure of the underlying current-current weak interaction Hamiltonian in the low momentum transfer limit. For neutrinos in state l on a trajectory with unit tangent vector k_l, the neutrino self-coupling Hamiltonian is given by a sum over neutrinos and antineutrinos m:

$$\begin{aligned} \hat{H}_{\nu\nu,l} &= \sqrt{2}\,G_{\rm F} \sum_m \left(1 - \hat{k}_l \cdot \hat{k}_m\right) n_{\nu,m} \left|\psi_{\nu,m}\right\rangle \left\langle\psi_{\nu,m}\right| \\ - & \sqrt{2}\,G_{\rm F} \sum_m \left(1 - \hat{k}_l \cdot \hat{k}_m\right) n_{\bar\nu,m} \left|\psi_{\bar\nu,m}\right\rangle \left\langle\psi_{\bar\nu,m}\right| \end{aligned} \tag{2.17}$$

where $\hat{k}_m$ is the unit trajectory tangent vector for neutrino or antineutrino m. Here $n_{\nu,m}$ is the local number density of neutrinos in state m.

2.4 Isospin Formalism

Another convenient formalism for treating the flavor transformation of neutrinos is found by employing a geometric object known as the “Neutrino Flavor Isospin” , or NFIS (pronounced Noo-Fiss). Using a technique that dates back to Pauli, it is possible to map a two flavor neutrino state $|\psi_\nu\rangle$ from the SU(2) column vector representation into a spin 1/2, SO(3) spinor object, the NFIS.

Explicitly the flavor state of neutrino i is:

$$|\psi_{\nu,\mathrm{i}}\rangle \equiv \begin{pmatrix} a_{\nu_\mathrm{e}} \\ a_{\nu_\mu} \end{pmatrix} , \tag{2.18}$$

where a_{ν_e} is the complex amplitude for a neutrino to be in the electron flavor state, and a_{ν_μ} is the amplitude for the neutrino to be in the muon flavor state, with the standard normalization convention that $|a_{\nu_\mathrm{e}}|^2 + |a_{\nu_\mu}|^2 = 1$. For anti-neutrinos, it is conventional to define the flavor state column vector for anti-neutrino i as,

$$|\psi_{\bar{\nu},\mathrm{i}}\rangle \equiv \begin{pmatrix} -a_{\bar{\nu}_\mu} \\ a_{\bar{\nu}_\mathrm{e}} \end{pmatrix} , \tag{2.19}$$

where again $a_{\bar{\nu}_\mathrm{e}}$ and $a_{\bar{\nu}_\mu}$ are the amplitudes for the anti-neutrino to be in the electron and muon flavor states, respectively.

With these two definitions, one can map the individual neutrino flavor states into a NFIS spinor, $\mathbf{s}_{\nu(\bar{\nu})}$ for neutrinos (anti-neutrinos), which formally represents the expectation value of the Pauli spin operator. For neutrino i, this is defined as,

$$\mathbf{s}_{\nu,\mathrm{i}} \equiv \langle\psi_{\nu,\mathrm{i}}|\frac{\sigma}{2}|\psi_{\nu,\mathrm{i}}\rangle = \frac{1}{2}\begin{pmatrix} 2\mathrm{Re}\left(a^*_{\nu_\mathrm{e}} a_{\nu_\mu}\right) \\ 2\mathrm{Im}\left(a^*_{\nu_\mathrm{e}} a_{\nu_\mu}\right) \\ |a_{\nu_\mathrm{e}}|^2 - |a_{\nu_\mu}|^2 \end{pmatrix} , \tag{2.20}$$

and for anti-neutrino i,

$$\mathbf{s}_{\bar{\nu},\mathrm{i}} \equiv \langle\psi_{\bar{\nu},\mathrm{i}}|\frac{\sigma}{2}|\psi_{\bar{\nu},\mathrm{i}}\rangle = -\frac{1}{2}\begin{pmatrix} 2\mathrm{Re}\left(a_{\bar{\nu}_\mathrm{e}} a^*_{\bar{\nu}_\mu}\right) \\ 2\mathrm{Im}\left(a_{\bar{\nu}_\mathrm{e}} a^*_{\bar{\nu}_\mu}\right) \\ |a_{\bar{\nu}_\mathrm{e}}|^2 - |a_{\bar{\nu}_\mu}|^2 \end{pmatrix} , \tag{2.21}$$

where σ are the Pauli spin matrices.

Using the NFIS formalism, the neutrino flavor states are now a part of an SO(3) flavor basis where the projection of the NFIS vector onto the z axis, denoted by the unit vector $\hat{\mathbf{e}}^{\mathrm{f}}_{\mathrm{z}}$, gives a direct measure of the probability for the neutrino to occupy either flavor state. The x-y plane in the NFIS flavor basis, defined by $\hat{\mathbf{e}}^{\mathrm{f}}_{\mathrm{x}}$ and $\hat{\mathbf{e}}^{\mathrm{f}}_{\mathrm{y}}$, preserve completely the complex phase information in the original state $|\psi_\nu\rangle$. The particular choice of convention for constructing $\mathbf{s}_{\nu(\bar{\nu})}$ was made so the the equation of motion for the evolution of these NFISs can be written in a unified fashion.

Analogs for the neutrino coherent forward scattering Hamiltonians can be constructed for the SO(3) symmetry group by applying the same transformation used on the neutrino flavor states to the Hamiltonian matrices. The vacuum Hamiltonian for neutrino i becomes the vector,

$$\mathbf{H}_{\mathrm{V,i}} \equiv \omega_n \left(-\hat{\mathbf{e}}^{\mathrm{f}}_{\mathrm{x}} \sin 2\theta_{\mathrm{V}} + \hat{\mathbf{e}}^{\mathrm{f}}_{\mathrm{z}} \cos 2\theta_{\mathrm{V}}\right), \tag{2.22}$$

where $\omega_n = \pm\Delta m^2/2E_n$ is the neutrino flavor state vacuum oscillation frequency, with + chosen for neutrinos and − chosen for anti-neutrinos. The neutrino-matter forward scattering Hamiltonian becomes the matter potential vector $\mathbf{H}_{\mathrm{e}}$,

$$\mathbf{H}_{\mathrm{e}} \equiv -\sqrt{2} G_{\mathrm{F}} n_{\mathrm{e}} \hat{\mathbf{e}}^{\mathrm{f}}_{\mathrm{z}}. \tag{2.23}$$

Finally, the neutrino-neutrino neutral current forward scattering Hamiltonian for neutrino l on trajectory $\hat{k}_l$ becomes the neutrino self-coupling vector,

$$\mathbf{H}_{\nu\nu,l} \equiv = \mu_\nu \sum_m \left(1 - \hat{k}_l \cdot \hat{k}_m\right) n_{\nu,m}\, \mathbf{s}_m\,, \tag{2.24}$$

where $\mu_\nu \equiv -2\sqrt{2} G_{\mathrm{F}}$ and the sum on m runs over all neutrino and anti-neutrino NFISs, $\mathbf{s}_m$.

Formulating the coherent forward scattering potentials in this fashion allows us to write the equation of motion for the flavor evolution of individual neutrinos and anti-neutrinos as the precession a single NFIS $\mathbf{s}_{\mathrm{i}}$ around an effective external field:

$$\frac{d}{dt}\mathbf{s}_{\mathrm{i}} = \mathbf{s}_{\mathrm{i}} \times \mathbf{H}_{\mathrm{i}}\,, \tag{2.25}$$

where the effective external field $\mathbf{H}_{\rm i} = \mathbf{H}_{\rm V,i} + \mathbf{H}_{\rm e} + \mathbf{H}_{\nu\nu,\rm i}$. As $\mathbf{s}_{\rm i}$ precesses around $\mathbf{H}_{\rm i}$, shown in Fig. 2.1, the projection of the NFIS along the $\hat{\mathbf{e}}^{\rm f}_{\rm z}$ axis will oscillate, following the changing flavor content of the neutrino or anti-neutrino flavor state.

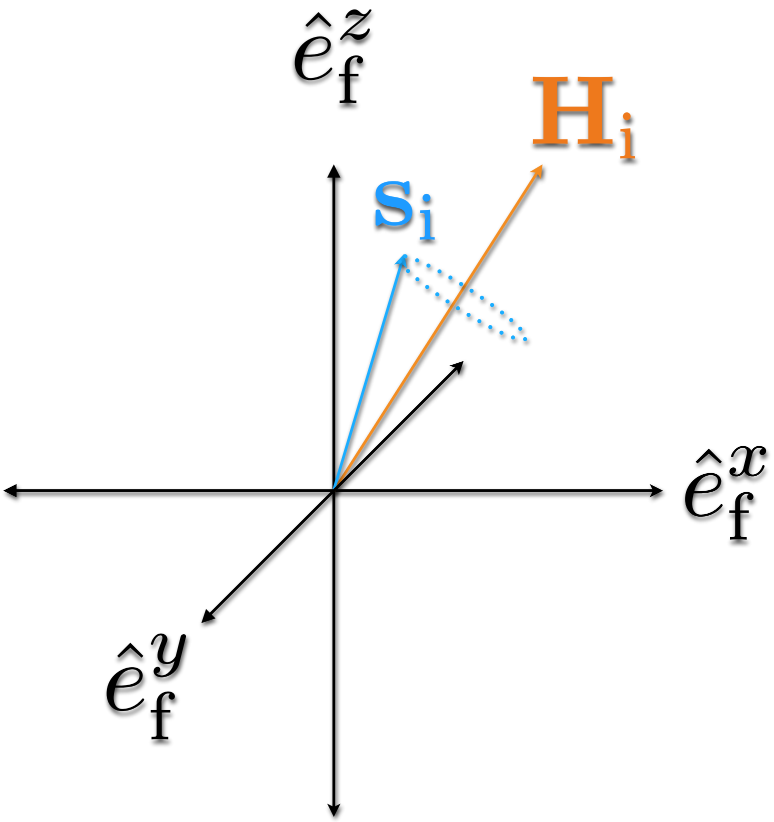

Figure 2.1: The precession of NFIS $\mathbf{s}_{\rm i}$ about the effective external field $\mathbf{H}_{\rm i}$.

Chapter 3

Simulation Methodology

The supernova environment is a physical system that is characterized by it's dynamic nature (it is an *explosion*, after all). From the point of view of a neutrino, however, the supernova itself is a static environment. Neutrinos emerging from the core have energies in the $\sim 10\,\mathrm{MeV}$ range. Comparing that energy to the neutrino rest mass energies, the sum of which are constrained to be something less than $\sim 1\,\mathrm{eV}$, it is readily apparent that these particles are ultra-relativistic. Thus the lapse of proper time experienced by a neutrino as it streams outward through the supernova envelope is miniscule compared to the timescale on which the supernova explosion evolves, which is $O\,(10\,\mathrm{ms})$. Therefore, as one follows the forward scattering evolution of neutrino flavor states along their world lines, the supernova environment appears fixed as one increments along the affine coordinate.

Thus, at a particular epoch of the supernova explosion, and with a specified matter density profile and specified initial neutrino fluxes and energy spectra, numerical calculation of the neutrino flavor field above the proto-neutron star can be accomplished with a self-consistent solution of Eq. 2.14, taking the supernova environment to be a static backdrop. This must include a prescription for treating $H_{\nu\nu}$ in Eq. 2.17, which couples flavor evolution on intersecting neutrino trajectories. In the past, this has been done by adopting the so-called "single-angle" approximation [56], where the flavor evolution along a specified neutrino trajectory (*e.g.,* the radial trajectory) is taken to apply along all other trajectories at corresponding values of the affine coordinate on those world lines. This work employs a “multi-angle” treatment, where neutrino flavor evolution histories are allowed to vary freely between different neutrino trajectories in the self-consistent evaluation of the Hamiltonian in Eq. 2.17. Though this approach is especially difficult to carry out computationally in a full, three active neutrino flavor mixing scheme, some supernova scenarios require such a treatment. To this end, numerical techniques have been developed to implement this approach, and the end result of this effort has been the BULB code, originally developed by Joe Carlson at LANL, which employs fine grained parallel computation to provide the necessary processing capacity to implement the multi-angle treatment.

3.1 Physical Setup

The primary difficulty in calculating the evolution of neutrino flavor states is the complicated structure of the neutrino-neutrino contributions to the overall forward scattering Hamiltonian. This portion of the Hamiltonian renders the problem nonlinear and geometry dependent, as the interactions which dictate flavor transformation amplitudes are themselves dependent on the local neutrino flavor states and intersection angles. This can potentially couple the flavor evolution histories of neutrinos moving along different trajectories, as shown in Figure 3.1. Following the flavor evolution of neutrino i, emitted from the neutrinosphere at an angle ϑ_{i} (measured from the outward unit normal), will entail knowing the flavor evolution histories and intersection angles of all of the other neutrinos j, each emitted at an angle ϑ_{j}, which cross its world line.

To make the geometric representation simple enough to be modeled with the current generation of supercomputers, the standard approach is to adopt a spherically symmetric “bulb” model (hence the name of the code). In this model, neutrinos are emitted semi-isotropically (isotropic in the outward radial direction of the surface) from a sharp spherical shell, which is referred to as the neutrinosphere. In three dimensions, it can be shown with a bit of algebra that the angle of intersection between two neutrino emission trajectories, θ_{ij}, in Figure 3.1

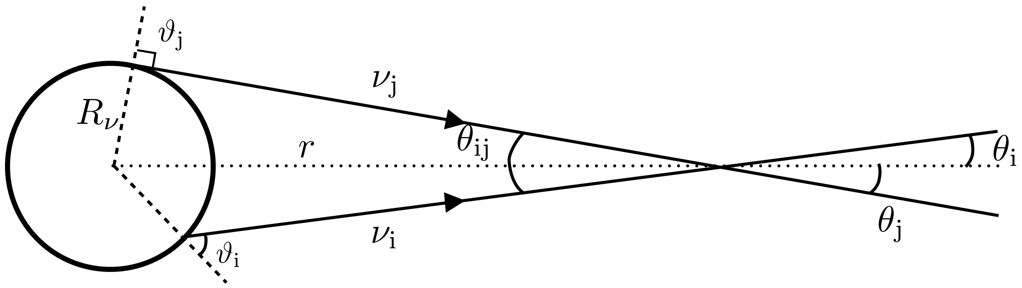

Figure 3.1: A cartoon illustration of the neutrino emission from the surface of a protoneutron star. Neutrinos emerge from the neutrinosphere, a hard spherical shell with radius R_ν. The neutrino emission trajectories are characterized by ϑ, the angle relative to the normal of the neutrinosphere surface at the location where they are emitted. Both neutrinos i and j stream outward until their trajectories intersect at a distance r from the center of the protoneutron star, with intersection angle $\theta_{\rm ij}$. This intersection angle sets the strength of the neutrino-neutrino neutral current forward scattering interaction that these neutrinos both experience at this location.

is,

$$\cos\theta_{\rm ij} = \cos\vartheta_{\rm i}\cos\vartheta_{\rm j} + \sin\vartheta_{\rm i}\sin\vartheta_{\rm j}\cos\left(\phi_{\rm i} - \phi_{\rm j}\right) \ , \tag{3.1}$$

where $\phi_{\rm i}$ and $\phi_{\rm j}$ are the azimuthal angles about the radial direction that describe the emission locations of neutrinos i and j. These angles are not included in Figure 3.1 because it is easy to show that integral over $(\phi_{\rm i} - \phi_{\rm j})$ causes the second term in Equation 3.1 to vanish, leaving the much more useful expression

$$\cos\theta_{\rm ij} = \cos\vartheta_{\rm i}\cos\vartheta_{\rm j} \ . \tag{3.2}$$

With a large number of neutrinos, following flavor evolution independently can rapidly expand to a dauntingly large problem, especially when considered as a ray-by-ray cartoon such as Figure 3.1. However, by solving the for the evolution of all neutrinos simultaneously at fixed radial coordinate, the flavor evolution of the neutrinos can indeed be found in a self consistent manner.

One more element remains to be included in the initial description of neutrino emission at the neutrinosphere, which is the spectral energy distribution of the neutrinos along each trajectory. Equation 2.17 shows that in addition to the relative neutrinos trajectories, one must know the local number density of neutrinos in each flavor state in order to full compute $\hat{H}_{\nu\nu,\mathrm{i}}$. The neutrinos within the core have scattered many times with the matter of the PNS, bringing all flavors of neutrinos into thermal equilibrium. Near the surface of the PNS, the neutrinos decouple at slightly different radii due to differences in the opacity of PNS material for different flavors of neutrinos [65]. This leaves the individual flavors of neutrinos with initial energy spectra that can be fit with either a black body or "pinched" spectral type [65], the latter being slightly more peaked around the average neutrino energy.

Therefore, one begins with a set of initial spectral energy distributions $f_\nu\left(E_\nu\right)$ for neutrinos of each flavor ν, and energy E_ν,

$$f_\nu\left(E_\nu\right) \equiv \frac{1}{F_2\left(\eta_\nu\right) T_\nu^3} \frac{E_\nu^2}{\exp\left(E_\nu/T_\nu - \eta_\nu\right) + 1} \ , \tag{3.3}$$

where

$$F_n\left(\eta\right) \equiv \int_0^\infty \frac{x^n \mathrm{d}x}{\exp\left(x - \eta\right) + 1} \tag{3.4}$$

is the Fermi integral of order n, η_ν is the degeneracy parameter, T_ν is the neutrino temperature for each individual species of neutrino. In order to compute the number density of neutrinos, we will also need the total neutrino luminosity emerging form the core for each flavor state, L_ν. The BULB code itself does not specify the equation of state for matter in the PNS, and neither does it treat the transport of neutrinos within the core. By necessity, the parameters which characterize the initial neutrino emission: η_ν, T_ν, and L_ν, are taken as external input.

The BULB code takes emission form the surface of the neutrinosphere to be isotropic, which is a reasonable treatment for thermal emission of neutrinos. This makes the number flux of neutrinos with a given energy and flavor passing through a surface of fixed radius, $j_\nu\left(E_\nu\right)$, simple to compute by dimensional analysis. At the neutrinosphere the rate of neutrino emission for a single flavor and energy will be,

$$\frac{L_\nu}{\langle E_\nu\rangle} f_\nu\left(E_\nu\right) = 4\pi R_\nu^2 \int_0^1 2\pi j_\nu\left(E_\nu\right)\cos\vartheta \;\mathrm{d}\left(\cos\vartheta\right) \;, \tag{3.5}$$

which gives the expression for the number flux,

$$j_\nu\left(E_\nu\right) = \frac{L_\nu}{4\pi^2 R_\nu^2 \langle E_\nu\rangle} f_\nu\left(E_\nu\right) \;. \tag{3.6}$$

Because it is the neutrino number density *at the point of intersection* which enters into the expression for $\hat{H}_{\nu\nu}$, we must make a brief change of coordinates to the space of intersection angles θ. The expression for the partial number density of neutrinos, at fixed energy and flavor, along a pencil of directions passing through the point of intersection is,

$$\mathrm{d}n_\nu\left(E_\nu\right) = j_\nu\left(E_\nu\right)\mathrm{d}\left(\cos\theta\right)\mathrm{d}\phi \;. \tag{3.7}$$

With some laborious basic geometry, this can be transformed back into the emission coordinates from the surface of the neutrinosphere, and has the form

$$\mathrm{d}n_\nu\left(E_\nu\right) = \frac{j_\nu\left(E_\nu\right)\cos\vartheta \mathrm{d}\left(\cos\vartheta\right) R_\nu^2}{r^2\left(\sqrt{1-\left(\sin\vartheta R_\nu/r\right)^2} - \cos\vartheta R_\nu/r\right)}\mathrm{d}\phi \;. \tag{3.8}$$

Now we have all of the tools needed to specify the the state of $\hat{H}_\nu\nu$ as the flavor states of neutrinos evolve outward in radius.

The last piece of the total forward scattering Hamiltonian which must be computed dynamically as the calculation moves outward in radius is the matter component, $\hat{H}_\mathrm{e}$. Using an input data file generated from hydrodynamic simulations of supernova, the BULB code interpolates a smooth density profile ρ which is a function of the radial coordinate r. The matter potential itself is dependent on the local number density of electrons, which must be specified in units of $ln\left(\mathrm{km}^{-3}\right)$. Because of the assumed spherical symmetry, neutrinos with different emission angles from the surface of the neutrinosphere will see the same matter potential. The matter potential does not affect all emission angles equally, due to difference in the instantaneous integration step size for different trajectories, and that will be discussed in the next section.

3.2 Theory of Calculation

Fundamentally, the problem that one is solving when working out the flavor evolution of neutrinos using the BULB code is an initial value problem along the radial coordinate. Starting at the neutrinosphere, this problem consists of 9×2 possible neutrino states (3×3 flavor mixing with ν and $\bar{\nu}$), and numerical convergence requires each of those states be divided into ~ 400 energy bins along with ~ 1000 angle bins [41]. Altogether, BULB is simultaneously solving $\sim 7.2 \times 10^6$ non-linearly coupled ordinary differential equations.

A minor distinction must be made before we continue. There are in fact two distinct position coordinates of which we must keep track: Δr, which is the step size of the calculation along radial coordinate, and Δt, which is the step size of the calculation along an individual neutrino emission trajectory. The end goal of the calculation is to compute the flavor evolution by stepping outward in steps of size Δr, but the individual evolution of neutrino flavor states must be performed along the world lines of neutrinos using the Δt step. The spherical symmetry of the calculation makes the relation between the two steps a simple geometric relation based on the emission geometry of the neutrino trajectory and the present radial coordinate,

$$\Delta t = \frac{\Delta r}{\cos\theta} \approx \frac{\Delta r}{\sqrt{1 - \left(\sin\vartheta R_\nu / r\right)^2}} \ , \tag{3.9}$$

which reflects the difference in path length between different neutrino emission trajectories between r and $r + \Delta r$.

The prescription for solving Equation 2.14 in this context is to apply the Magnus method. We will insist that there is some oscillatory solution that describes the evolution of the neutrino flavor states as they move through the supernova envelope,

$$\psi'_{\nu,\mathrm{i}}\left(t\right) = A\left(t\right)\psi_{\nu,\mathrm{i}}\left(t\right) \ , \tag{3.10}$$

where t labels the affine parameter along the neutrino's world line. This is a sound approximation outside the neutrinosphere, where we are performing the calculation, because the processes which violate total neutrino number (such as ν capture or emission) are rare due to the relatively low matter density.

The Magnus method allows us to select a step size which is small enough such that,

$$\psi_{\nu,\mathrm{i}}\left(t+\Delta t\right) \simeq \exp\left(-i\hat{H}_{\nu,\mathrm{i}}\Delta t\right)\psi_{\nu,\mathrm{i}}\left(t\right)\ . \tag{3.11}$$

In principle, this reduces the problem to a matter of exponentiating the Hamiltonian matrix, and selecting a step size Δr such that all of the neutrino trajectories have a sufficiently small Δt.

Sketching the prescription for exponentiating the Hamiltonian matrix, one solves the eigenvalue equations,

$$\sum_b \hat{H}_{ab}V_{bc} = \zeta_c V_{ac}, \quad a,b,c = 1,2,3\ , \tag{3.12}$$

where $a,\ b$ are the row and column indices of $\hat{H}_{\nu,\mathrm{i}}$ and V_{bc} is the bth component of the cth eigenvector of $\hat{H}_{\nu,\mathrm{i}}$, with associated eigenvalue ζ_c. Once that is accomplished, the exponential is then,

$$\exp\left(-i\hat{H}_{\nu,\mathrm{i}}\Delta t\right) = V\begin{pmatrix} \mathrm{e}^{-i\zeta_1\Delta t} & 0 & 0 \\ 0 & \mathrm{e}^{-i\zeta_2\Delta t} & 0 \\ 0 & 0 & \mathrm{e}^{-i\zeta_3\Delta t} \end{pmatrix} V^{\dagger}\ . \tag{3.13}$$

The difficulty arrises, in this case, from the dynamical behavior of $\hat{H}_{\nu,\mathrm{i}}$. It is entirely possible for the eigenvalues of $\hat{H}_{\nu,\mathrm{i}}$ to be degenerate, or nearly so. When this occurs, solution algorithms for Equation 3.12 which rely on the linear independence of the eigenvectors V_c have numerical difficulty. When the neutrino self coupling terms are included in $\hat{H}_{\nu,\mathrm{i}}$, the system of neutrinos can enter this state unexpectedly due to non-linear effects.

To resolve this issue, the BULB code uses a free FORTRAN 77 package called “zheevh3”, which is ©Joachim Kopp (2006). The zheevh3 package employs a two step approach to solving for the eigenvalues and eigenvectors of $\hat{H}_{\nu,\mathrm{i}}$.

First, zheevh3 computes the characteristic polynomial of $\hat{H}_{\nu,\mathrm{i}}$,

$$\det\left(\hat{\mathrm{H}}_{\nu,\mathrm{i}} - \zeta\mathrm{I}\right) = 0\ , \tag{3.14}$$

where I is the identity matrix. The Cardano method is then used to solve the resulting cubic equation for the eigenvalues, ζ. From Equation 3.12 it can be seen that the eigenvector V_c is orthogonal to the complex conjugates of of the row vectors of the matrix $\hat{H}_{\nu,\mathrm{i}} - \eta_c I$. Selecting two linearly independent row vectors of $\hat{H}_{\nu,\mathrm{i}} - \eta_c I$, which I shall call $Z^{(1)}$ and $Z^{(2)}$, the zheevh3 package computes two of the eigenvectors by taking

$$V_c = \frac{Z^{(1)} \times Z^{(2)}}{|Z^{(1)} \times Z^{(2)}|} \ . \tag{3.15}$$

The last eigenvector is computed simply by taking the cross product of the complex conjugates of the two previous eigenvectors.

This method has manifest issues if any of the eigenvalues happen to be degenerate, and so the zheevh3 package checks for this problem after computing each of the first two eigenvectors. If a problem is found, the second, computationally slower method of solving for the remaining eigenvectors is implemented. First the matrix $\hat{H}_{\nu,\mathrm{i}}$ is converted to a real, tridiagonal form using Householder rotations (because they are unitary). Then the QL method with implicit shifts is then applied to $\hat{H}_{\nu,\mathrm{i}}$. This is useful because if $\hat{H}_{\nu,\mathrm{i}}$ has eigenvalues of different absolute value then the QL transformation converges to a lower triangular form, with eigenvalues of $\hat{H}_{\nu,\mathrm{i}}$ appearing on the diagonal in increasing order of their absolute magnitude. If $\hat{H}_{\nu,\mathrm{i}}$ has an eigenvalues η_c which are degenerate, then the QL method still converges to a lower triangular form with the exception for a diagonal block matrix whose eigenvalues are η_c.

3.3 Integration Algorithm

Once the difficulties of computing the eigenvalues and eigenvectors of the neutrino forward scattering hamiltonian have been addressed, the actual work of solving our system of 7 million ordinary differential equations can begin. The BULB code parallelizes the work load of computing solutions by splitting the neutrino flavor states among different processes according to emission angle bin. Typically one or two bins per process, and one process per core. Because so much work must be done diagonalizing the Hamiltonian matrices, the full calculation itself tends to be CPU speed limited. The amount of neutrino flavor state data that is present on a single core is 110 kB per angle bin, which keeps the total amount of time spent transferring data relatively low, despite the fact that every node on the network must talk to every other node.

The BULB code employs a variation of Heun's method for solving ordinary differential equations. Neutrinos begin in the previously stored final state (or in pure flavor states at initialization), $\psi_{\mathrm{init}} = \psi^{(0)}$, for each energy and angle bin at the starting point r.

Step 1 The assumed final state of the first step of Heun's method is initialized as the initial state of the neutrinos, $\psi^{(0)} = \psi^{(1)}$, where $\psi^{(1)}$ will eventually become the state of neutrinos at $r + \Delta r$.

Step 2 All of the neutrino flavor states are gathered on process 0. The first neutrino self coupling potential is calculated, $\hat{H}^{(0)}_{\nu\nu}$ using the neutrino density matrix elements $\rho^{(0)}_{\nu\nu} = 1/2\left[\psi^{(0)}\mathrm{d}n_\nu\left(r,\vartheta\right) + \psi^{(1)}\mathrm{d}n_\nu\left(r+\Delta r,\vartheta\right)\right]$.

Step 3 The resulting list of elements of $\hat{H}^{(0)}_{\nu\nu}$ are then broadcast to all nodes. In this way, each node can now use the neutrino trajectory data that is unique to its own batch of neutrino emission angle bins to finish computing $\hat{H}_{\nu\nu}$, $\hat{H}_{\mathrm{V}}$, $\hat{H}_{\mathrm{e}}$, and Δt.

Step 4 Each node now computes the result of Equation 3.11 to obtain the actual $\psi^{(1)}$, at the radius $r + \Delta r$.

Step 5 The step size is now reduced to $\Delta r/2$.

Step 6 All of the neutrino flavor states are again gathered on process 0. The second neutrino self coupling potential is calculated, $\hat{H}^{(1)}_{\nu\nu}$ using the neutrino density matrix elements $\rho^{(1)}_{\nu\nu} = 1/2\left[\psi^{(0)}\mathrm{d}n_\nu\left(r,\vartheta\right) + \psi^{(1)}\mathrm{d}n_\nu\left(r+\Delta r/2,\vartheta\right)\right]$.

Step 7 Steps 3 and 4 are now repeated with $\hat{H}^{(1)}_{\nu\nu}$ and $\Delta r/2$ to obtain an interim set of neutrino flavor states, $\psi^{(2)}$, at radius $r + \Delta r/2$.

Step 8 Steps 2 and 3 are repeated again, using $\psi^{(2)}$ as the initial flavor state and $r + \Delta r/2$ as the starting location. A third neutrino self coupling Hamiltonian, $\hat{H}^{(2)}_{\nu\nu}$ is computed using the neutrino density matrix elements $\rho^{(2)}_{\nu\nu} = 1/2\left[\psi^{(2)}\mathrm{d}n_\nu\left(r+\Delta r/2,\vartheta\right) + \psi^{(0)}\mathrm{d}n_\nu\left(r+\Delta r,\vartheta\right)\right]$.

Step 9 Each node now computes the result of Equation 3.11 to obtain the final state after taking two half steps, $\psi^{(3)}$, at the radius $r + \Delta r$.

Step 10 Each node now checks the relative error between $\psi^{(1)}$ and $\psi^{(3)}$. To do so, the absolute difference between the electron flavor state components is compared for each energy bin on the node, $Err = |\langle \nu_\mathrm{e} | \psi^{(1)} \rangle|^2 - |\langle \nu_\mathrm{e} | \psi^{(3)} \rangle|^2$. If Err in any bin on any process is larger than the specified tolerance, typically 1×10^{-7}, the step size Δr is halved and the algorithm begins at the original starting point. If the Err is within tolerance, the new radius and flavor states are accepted and the algorithm starts again at the new radius.

This algorithm is iterated upon 10^5 to 10^6 times for each process in a typical calculation. As a result the state of the system of neutrino flavor states is not saved to disk after every iteration. The BULB code can be configured via input commands to save the present state after a specified number of iteration steps, or to save the present state after the code has progressed a specified distance along the radial coordinate. Typically, the fixed radial interval is used to specify disk writes, with a specified step size of $1 - 10\,\mathrm{km}$. This choice of step size is convenient for studying collective flavor oscillations of the neutrinos, which usually occur on length scales of (a few)$\times 10\,\mathrm{km}$.

When saving state, the BULB code appends data to three files:

he.sav Stores the present radius along with the $\hat{H}_\mathrm{V} + \hat{H}_\mathrm{e}$ Hamiltonian matrix. This matrix is neither complex nor emission angle dependent, but it is neutrino energy dependent, and as a result holds two ($\nu/\bar{\nu}$) 3×3 double precision float arrays of values for each neutrino energy.

hvv.sav Stores the present radius along with the $\hat{H}_{\nu\nu}$ Hamiltonian matrix. This matrix is the same for all neutrino energies, but is complex and emission angle dependent. This means that each emission angle bin has two ($\nu/\bar{\nu}$) 3×3 arrays where every element is specified by two double precision floats (the real and complex pieces of each array element).

wvdat.sav Stores the present radius along with the full flavor state of all neutrinos in the calculation. Each unique combination of energy and angle bins has two

$(\nu/\bar{\nu})$ 3×3 arrays of wave function data. Each row of the array represents the complex amplitude of a neutrino initially in one of the three active flavor states, and as such each element is composed of two double precision floats.

The BULB code also generates (and overwrites if it is pre-existing) a single data file that holds only the current wave function data for all neutrinos, wvdat.out, which is formatted in precisely the same fashion as wvdat.sav, but holds only data for the most recently saved state. This file can be renamed wvdat.in, and used as a restart point if the program is not completed within the wall clock time limit (or in the event of a crash).

The size of these data files on disk does require some care with respect to data handling. The size of a single snapshot of the wave function for all individual neutrino states is $\sim 110\,\mathrm{MB}$ with the typical number of energy and emission angle bins. This means that saving the state of the neutrinos every $1\,\mathrm{km}$ will produce a wvdat.sav file which is $\sim 0.5 - 1\,\mathrm{TB}$ for a typical calculation (the hvv.sav file is the next largest, and is a factor of a few hundred smaller).

Chapter 4

Core-Collapse Supernovae

4.1 Introduction

Presented here are the results of the first multi-angle, self-consistent, 3-flavor simulation of neutrino flavor evolution in the core collapse supernova environment. With an expected ultimate energy release of $\sim 0.1\,\mathrm{M}_\odot$ as neutrinos of all kinds, these supernovae have long been studied as potential sources of neutrinos which could provide probes of physics beyond the reach or scope of conventional terrestrial experiments, and neutrino flavor oscillations are the case in point. Though we already know a great deal about neutrino mass-squared differences and flavor mixing properties from experiments, there are still fundamental neutrino mixing physics unknowns, *e.g.,* the neutrino mass hierarchy, mixing angle θ_{13}, and CP violating phase δ. Assessing how the known and unknown neutrino flavor oscillation physics affects the core-collapse neutrino burst signature is a necessary step in understanding supernovae, as well as in gleaning insight into fundamental neutrino physics.

We have chosen to examine the neutrino emission from supernovae originating from stars in the mass range $\sim 8 - 12\,\mathrm{M}_\odot$. These supernova progenitors in this mass range are expected to be relatively common, comprising 25% or more of core collapse supernova events (taking the number of stars per unit mass to be $\propto m^{-2.35}$, using the Salpeter initial mass function). These relatively light supernova progenitors develop O-Ne-Mg cores, which do not achieve sufficient internal temperature to ignite oxygen burning. Due to the low mass (below $\sim 12\,M_\odot$), the inner core burns carbon and oxygen an order of magnitude more slowly than the cores of more massive progenitors, over $\sim 10^5$ years [2, 3]. As a result, there is a lull in nuclear burning at the center of the star, and the O-Ne-Mg core undergoes Kelvin-Helmholtz contraction, cooling efficiently via neutrino emission for $\sim 10^4$ years [2, 3].

Because the core is cooling and contracting for such a length of time, the degenerate electrons in the core transition to relativistic-degenerate electrons as the electron Fermi energy creeps above the electron rest mass. This causes the core to undergo gravitational collapse, triggered by depletion of electrons at the top of the Fermi sea (which are providing all of the pressure support) via electron capture on Ne and Mg isotopes. This collapse leaves a thin envelope above the proto-neutron star remnant, in contrast to the envelopes of more massive stars that have undergone the gravitational collapse of an Fe core.

The early collapse of the O-Ne-Mg core will have little impact on the initial phases of neutrino emission from the PNS. The entropy per baryon in the collapse of the O-Ne-Mg core is slightly lower than that of an Fe core, owing to the efficient pre-collapse cooling. This lower entropy per baryon provides more efficient electron capture as the core collapses [9], which shifts the slightly higher electron fraction, Y_e, of the O-Ne-Mg core to roughly the same value as that of an Fe core which is in the same stage of collapse, resulting in the cores of both cases possesing $Y_\mathrm{e} \approx 0.3$. When the collapsing core passes neutrino trapping density at $\rho \sim 10^{12}\,\mathrm{g\ cm^{-3}}$, the net lepton number in the core is frozen in place, even though neutronization of the core proceeds. Production of ν_e by electron capture cannot lower the lepton number of the core because the ν_e can no longer escape.

After the core of the O-Ne-Mg progenitor reaches bottom and launches a bounce shock, the neutrinosphere will only begin to shine once the shock has propagated out to the region where neutrinos decouple from the PNS matter. Bear in mind, the neutrino emission from the core is *thermal radiation*, so for a core with a neutrinosphere at temperature $T_\text{neutrinosphere}$, $L_\nu \propto T^4_\text{neutrinosphere}$. This means that the neutrinosphere will only begin to shine with its full luminosity after the shock front has propagated through and raised the local temperature to $T_{\text{neutrinosphere}} \sim 10\,\text{MeV}$. Once this transpires, the vast preponderance of lepton number that was trapped in the core is radiated away as an intense burst of ν_{e}.

The collapse of the core, with $Y_{\text{e}} \approx 0.3$, has trapped $\sim 3^{56}$ units of electron lepton flavor in the PNS, which are in the form of a sea of ν_{e}. It is these ν_{e} which are the first neutrinos to escape the core. If each of these neutrinos carry away the typical thermal energy of 10 MeV at the neutrinosphere surface, and the core radiates with the luminosity calculated in chapter 1, $L_\nu \sim 10^{53}\,\text{erg s}^{-1}$, this initial burst of pure ν_{e}, termed the "Neutronization Burst" will last $\sim 30 - 50\,\text{ms}$. This timescale is a result that is confirmed by much more detailed calculations of neutrino emission during the early stages the explosion [4, 5].

Progenitors of O-Ne-Mg core-collapse supernovae are characterized by a steep matter density gradient above the core, which may have shed most of the hydrogen envelope prior to core collapse due to pulsation and winds. These characteristics lead to two salient features of O-Ne-Mg core-collapse events. First, in contrast to the Fe core-collapse case, the bounce shock in models of these supernovae is not severely hindered by the pressure of material falling onto the core. Consequently, explosion by direct neutrino driven shock re-heateing is obtained [66, 67, 68]. Second, the steep matter gradient above the core allows neutrino self-coupling (neutral-current neutrino-neutrino forward exchange scattering) to engineer collective neutrino flavor transformation [24, 69, 70, 25, 71, 72, 56, 73, 74, 75, 27, 76, 77] during the early phase of neutrino emission, including shock break-out and the attendant neutronization neutrino burst [40, 78].

However, there is another consequence of the steep matter density gradient. A steep matter gradient necessitates accounting for the physics of the interference between neutrino flavor mixing scales. Essentially, Mikheyev-Smirnov-Wolfenstein (MSW) resonances can occur very near to each other in physical and energy space when the matter density profile drops off rapidly with radius. The near overlapping of resonances for the solar and atmospheric vacuum neutrino mass-squared differences, $\Delta m^2_{\odot} = 7.6 \times 10^{-5}\,\text{eV}^2$ and $\Delta m^2_{\text{atm}} = 2.4 \times 10^{-3}\,\text{eV}^2$, respectively, dictates that a full 3×3 flavor treatment must be employed. Because these resonances occur close to the core, and because in this case the number density of neutrinos emitted from the core will fall much more slowly than the local matter density, the anisotropic nature of the supernova environment necessitates a multi-angle simulation that includes trajectory-dependent neutrino self-coupling [6, 29, 32, 33, 34, 35, 40, 41, 46].

After the neutronization burst, the dynamics of Fe core-collapse supernova begin to diverge from that of the explosion of O-Ne-Mg progenitors. Unlike O-Ne-Mg cores, Fe cores are jacketed in layers of heavy elements that are the end products of burning shells further out in the envelope of the progenitor star. As was mentioned in Chapter 1, the photodissociation of these heavy elements as they stream inward saps the energy of the bounce shock at the rate of $\sim 8\,\mathrm{MeV}$ per baryon passed through the shock.

Neutrino heating of the shocked material is hampered by the naturally low cross section for Weak interactions. Further complicating the issue, the number of scattering processes which deposit neutrino energy into matter are also few in number. The largest number of targets exist for neutrino neutral current scattering off of free nucleons and heavy nuclei,

$$\nu + A\left(Z, N\right) \rightarrow \nu + A\left(Z, N\right) \ , \tag{4.1}$$

but because of the large differences between neutrino energies, $\sim 10\,\mathrm{MeV}$, and the target rest masses $\geq 1\,\mathrm{GeV}$, there is little to no momentum transfer to the target, and hence little heating.

The channel used to detect neutrinos in water Cherenkov detectors, which does deposit appreciable amounts of neutrino energy, involves charged current scattering of $\nu_{\mathrm{e}}/\bar{\nu}_{\mathrm{e}}$ on electrons. However, the extreme matter densities just above the surface of the PNS are electron degenerate, and as a result the neutrino-electron charged current scattering processes which change electron energy are strongly suppressed by Pauli blocking. This leaves two dominant neutrino heating processes,

$$\nu_{\mathrm{e}} + n \rightarrow p^{+} + e^{-} \tag{4.2}$$

$$\bar{\nu}_{\mathrm{e}} + p^{+} \rightarrow n + e^{+} \ , \tag{4.3}$$

which proceed via charged current neutrino/antineutrino capture on neutrons and protons, respectively.

The cross sections, σ, for the processes in Equations 4.3 and 4.3 scale as $\sigma \propto E_{\nu}^{2}$, where E_{ν} is the neutrino energy in each interaction [14]. Because these are capture processes, the energy deposited will be equal to the energy of the neutrino on the right hand side of both interactions, leading to the relation that the direct neutrino capture heating rate, H, at the point r outside the neutrinosphere will be

$$H \propto \frac{\rho X_{\mathrm{n}} L_{\nu_{\mathrm{e}}} \langle E_{\nu_{\mathrm{e}}}^{2} \rangle}{r^{2}} + \frac{\rho X_{\mathrm{p}} L_{\bar{\nu}_{\mathrm{e}}} \langle E_{\bar{\nu}_{\mathrm{e}}}^{2} \rangle}{r^{2}} \ , \tag{4.4}$$

where ρ is the local matter density, and the number fractions of neutrons and protons are X_{n} and X_{p}, respectively. The $1/r^{2}$ dependence of the heating rate is simply due to the geometric flux dilution of neutrinos after they emerge from the core.

The dependence of H on the radius means that location of the most effective neutrino heating will be close to the PNS, but there is a catch. The thermal creation of positron electron pairs can proceed when the temperature of matter reaches roughly E_{f}, the fermi energy for electrons. Most positron electron pairs will annihilate into photon pairs, which does not detract from the thermal energy in the shocked matter, but occasionally they will annihilate into $\nu/\bar{\nu}$ pairs which directly stream out of the star and steal away thermal energy. The rate for the cooling of the core, C, by this mechanism is

$$C \sim 1.4 \times 10^{20} \left(\frac{T}{2\,\mathrm{MeV}} \right)^{6} \mathrm{erg\ g^{-1}\ s^{-1}} \ , \tag{4.5}$$

where T is the local matter temperature [14]. Initially, the temperature within the shock front is near the point where the cooling computed from Equation 4.5 is only marginally lower than the heating rate computed from Equation 4.4. This leads to a situation where the different dependencies for the heating and cooling rates cause the formation of what has come to be called the “gain radius” , below which the rate of cooling by neutrino pair emission exceeds the heating rate by neutrino capture from the core. There is no net heating of the shock below the gain radius, which reduces the effective volume which can contribute additional thermal energy to revitalizing the shock front.

In 1D calculations, the gain radius grows outward steadily, which reduces the volume of the shock which is heated by neutrinos and means that as more matter is accreted onto the shock front, the neutrino heating is growing less and less efficient. As a result, 1D models of Fe core collapse supernovae do not successfully explode.

With the advent of computer models using multi-dimension hydrodynamics and radiation transport the neutrino explosion mechanism gained new life. A hydrodynamic phenomenon known as the Standing Accretion Shock Instability, "SASI", was discovered [12, 19]. The SASI is a dynamical phenomenon that arrises because shocks, such as the core-collapse supernova bounce shock, are perfect absorbers of sound waves. Once the bounce shock has stalled, random locations on the inner surface absorb more slightly more energy, causing different polar and azimuthal locations along surfaces of the stalled shock front to oscillate violently in radial coordinate. This oscillation drives turbulent mixing behind the shock, positively reinforcing the inhomogeneous heating which powers it, leading to the aptly named instability. This process of turbulent mixing behind the shock front also rapidly transports cold, unshocked matter down to the region above the PNS, while simultaneously ejecting neutrino heated matter in convective plumes out to the shock front where the hot matter deposits it's thermal energy. Critically, the cold matter transported close to the PNS is much more efficient at absorbing energy from the neutrino flux than hot matter. The un-shocked material is too cold to re-radiate thermal neutrinos at a rate above the rate at which it absorbs energy from the outward neutrino flux. This increases the overall volume of the "gain region", where the rate of energy deposition by the PNS neutrino flux is larger than the rate of energy loss due to cooling by thermal emission of $\nu - \bar{\nu}$ pairs.

The combination of these effects; rapid turbulent transport of hot/cold matter, more efficient neutrino heating, and expansion of the gain region, has lead to the discovery that $12 - 30\,M_{\odot}$ stars can obtain a delayed explosion through neutrino heating. However, these supernova models have largely omitted the physics of neutrino flavor transformation. The intense flux of neutrinos from the PNS produces an environment where neutrinos are so numerous that they contribute in a significant way to their own coherent forward scattering. This produces a non-linear coupling of neutrino flavor evolution histories that can produce large, collective neutrino flavor oscillations in matter density regimes that have previously been thought to suppress neutrino flavor evolution.

4.2 Neutronization Burst Signal

Nonlinear neutrino flavor transformation in supernovae is a subject in its infancy and, by necessity, much of the discussion in the supernova community is focused on technical issues on how to calculate it. To that end this section raises an important point, that a "standard" simplifying treatment of the problem, the widely used "single-angle" approximation, may not reproduce the results of more sophisticated "multi-angle" calculations.

Reference [40], which employs the single-angle approximation, found two flavor swaps in the normal mass hierarchy for the O-Ne-Mg core collapse neutronization burst, one for each mass-squared splitting, but only one flavor swap in the inverted mass hierarchy. The general features found in the results of Ref. [40] seem to agree with the semi-analytical analysis in Ref. [78]. Reference [43] has pointed out that in single-angle calculations, under some circumstances, a single mass-squared splitting can give rise to two spectral swaps. However, Ref. [79] demonstrated recently that full 3×3 simulations, as opposed to a sequence of 2×2 level crossings, may be necessary to understand the formation or suppression of these multiple flavor swaps.

As in Ref. [40], to better understand multi-angle effects in 3×3 neutrino flavor oscillation scenarios and to enable direct comparison between single-angle and multi-angle calculations, I have chosen to simulate the epoch of the neutronization neutrino burst. This corresponds to an epoch only some $\sim 10\,\mathrm{ms}$ after core bounce, when the shock wave propagates through the neutrino sphere. The total neutrino luminosity at this epoch is comprised predominantly, but not exclusively, of electron type neutrinos (ν_{e}) left over from core collapse-driven neutronization.

4.2.1 Overview

The results of our multi-angle, 3×3 simulations in a particular case are shown in Fig. 4.1 for the inverted neutrino mass hierarchy. I have used the values $\theta_{13} = 0.1$, $\theta_{12} = 0.6$, $\theta_{23} = \pi/4$, $\Delta m^2_{21} = 8.0 \times 10^{-5}\,\mathrm{eV}^2$, and $\Delta m^2_{32} = -3.0 \times 10^{-3}\,\mathrm{eV}^2$ for this particular calculation to facilitate comparison with the choice of mixing parameters in Refs. [40, 78]. Furthermore, I have taken the electron neutrino luminosity and spectral energy distribution to match what was used in [40], giving $L_{\nu_\mathrm{e}} = 10^{53}\,\mathrm{erg\ s}^{-1}$ and a Fermi-Dirac energy distribution fit to $\langle E_{\nu_\mathrm{e}} \rangle = 10\,\mathrm{MeV}$ and $\eta = 3$.

All of our simulations of the neutronization neutrino burst from an ONeMg core-collapse supernova begin at an initial radius of $r = 900\,\mathrm{km}$, where the matter density is still large enough that no flavor transformation has yet taken place. In order to compare our results directly with the results of Ref. [40], I use the density profile from the pre-collapse calculations in Refs. [2, 3] in a post-bounce epoch. However, the epoch in which I performed the calculations is $\sim 10\,\mathrm{ms}$ post-bounce, while the free-fall timescale at the radius (900 km) at which I begin the calculations is $\tau \sim 100\,\mathrm{ms}$, so there is not much time for non-homologous modifications to the density profile. Moreover, the material at this radius is likely falling more slowly than the free fall rate. In any case, the objective of our calculations is to compare single and multi-angle treatments of neutrino flavor transformation. Ultimately, neutrino flavor transformation simulations must be performed in a consistent supernova model.

We model the neutrino emission as originating from a uniform sphere at a radius of $R_\nu = 60\,\mathrm{km}$ above the core of the proto-neutron star. R_ν is the calculated radius of the "neutrinosphere", where the electron neutrino optical depth is equal to unity. It has been observed that the neutrinosphere radius is not a sharp surface, but instead is partially smeared out depending on neutrino energy as discussed in Ref. [80]. In the case of ONeMg core-collapse supernovae the matter density profile falls so swiftly with radius that this effect is small compared to the radius of the neutrinosphere itself and also the distance above the neutrino-sphere where significant flavor transformation takes place.

In subsection 4.2.2, results of calculations with more recent and accurate values for neutrino mass-squared differences presented. Figure 4.1 presents the electron flavor neutrino survival probability $P_{\nu_{\rm e}\nu_{\rm e}}$, as a function of the cosine of the emission angle $\vartheta_{\rm R}$. It also shows the vacuum mass basis angle-averaged neutrino energy spectra. All of these results are at a radius $r = 5000\,{\rm km}$. In the simulations used to generate this figure I have followed Ref. [40], and I have approximated the flavor content of the neutronization burst for the O-Ne-Mg core-collapse as pure $\nu_{\rm e}$.

Our simulations show that neutrino flavor evolution in the inverted mass hierarchy agrees with what was found in Ref. [40] in broad brush and also seems to agree with the explanation offered in Ref. [78]. A clear step-wise swap occurs between the ν_2/ν_1 mass states at $E_\nu \approx 11\,{\rm MeV}$. As with the single-angle results, there is no large-scale neutrino flavor transformation generated by mixing at the $\Delta m^2_{\rm atm}$ scale.

It has been noted that in the inverted neutrino mass hierarchy the neutrino flavor field is unstable, in analogy to the way a pendulum balanced in the inverted position would be [81, 33]. Flavor transformation in the other neutrino and anti-neutrino species is non-linearly coupled to mixing at the $\Delta m^2_{\rm atm}$ scale through the neutrino self-coupling potentials. This coupling provides the impetus that drives the $\Delta m^2_{\rm atm}$ flavor isospins away from their unstable equilibrium. However, the lack of any neutrino species besides $\nu_{\rm e}$ in the calculation shown in Fig. 4.1 prevents any perturbation of the "inverted flavor pendulum," leaving it essentially balanced. The inclusion of other neutrino and anti-neutrino species, which have energy luminosities $L \sim 0.1 L_{\nu_{\rm e}}$ at this epoch, does not significantly affect these results and conclusions. Figure 4.2 shows that relatively small numbers ($\sim 10\%$ admixture) of these neutrinos are not capable of destabilizing the $\Delta m^2_{\rm atm}$ neutrino flavor mixing.

Figure 4.3 shows the results of the multi-angle simulations in the normal mass hierarchy. I have used the same mixing parameters and initial conditions employed in the inverted neutrino mass hierarchy calculation, except that the sign of the atmospheric mass-squared difference has been reversed, $\Delta m^2_{32} = +3.0 \times$

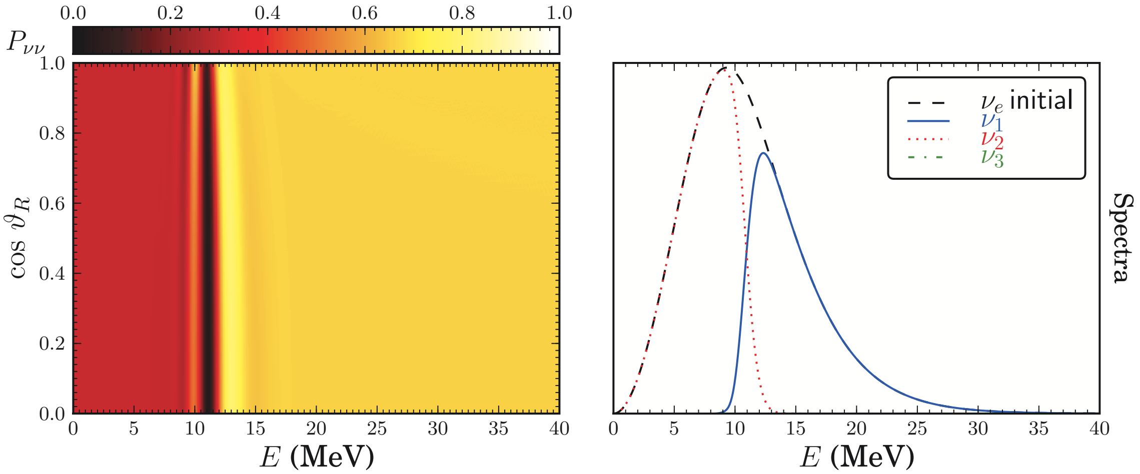

Figure 4.1: Left panel: electron neutrino survival probability $P_{\nu_e\nu_e}$ (color/shading key at top left) for the inverted mass hierarchy is shown as a function of cosine of emission angle, $\cos\vartheta_R$, and neutrino energy, E in MeV, plotted at a radius of $r = 5000\,\text{km}$. Right: mass basis (key top right, inset) emission angle-averaged neutrino energy distribution functions versus neutrino energy, E. The dashed curve gives the initial ν_e emission angle-averaged energy spectrum. Movies of this simulation can be found at the URL in Ref. [1]. Each frame of the movie shows a representation of the neutrino survival probability in various different bases at a fixed radius above the core. Each successive frame is 1 km further out from the initial radius of $r_{\text{init}} = 900\,\text{km}$ out to the final radius $r = 5000\,\text{km}$.

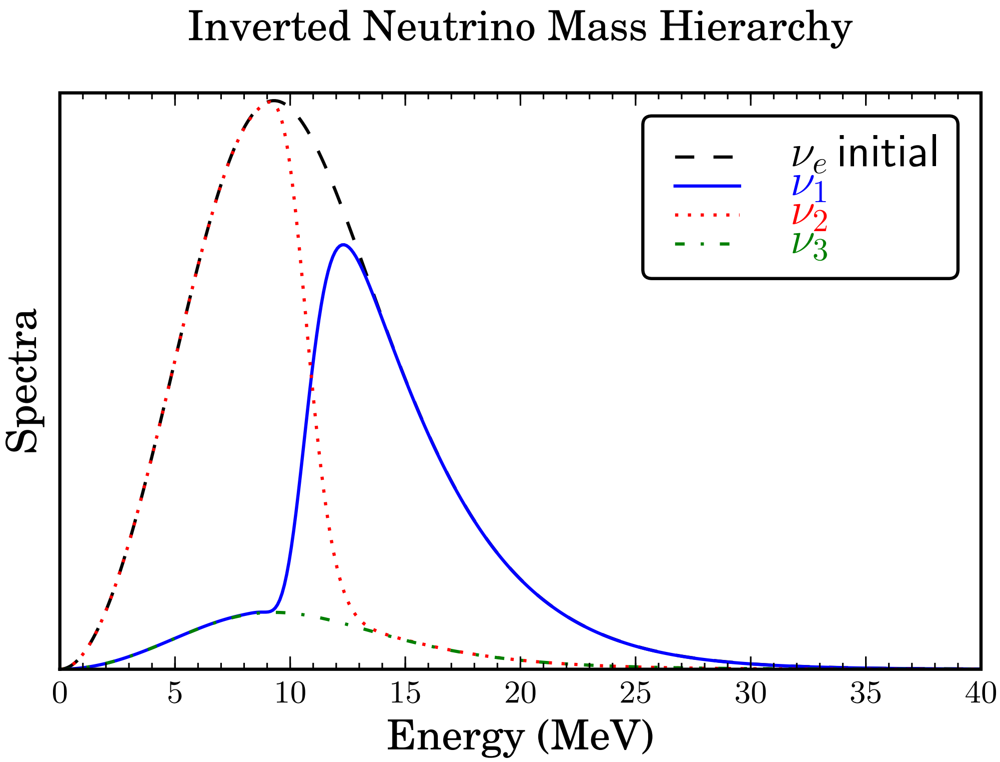

Figure 4.2: Emission angle-averaged neutrino energy distribution functions versus neutrino energy plotted in the neutrino mass basis for the 3×3 multi-angle calculation of neutrino flavor evolution. Results shown at a radius of $r = 5000$km. In this simulation, a small (10%) admixture of all other species of neutrinos and anti-neutrinos are included.

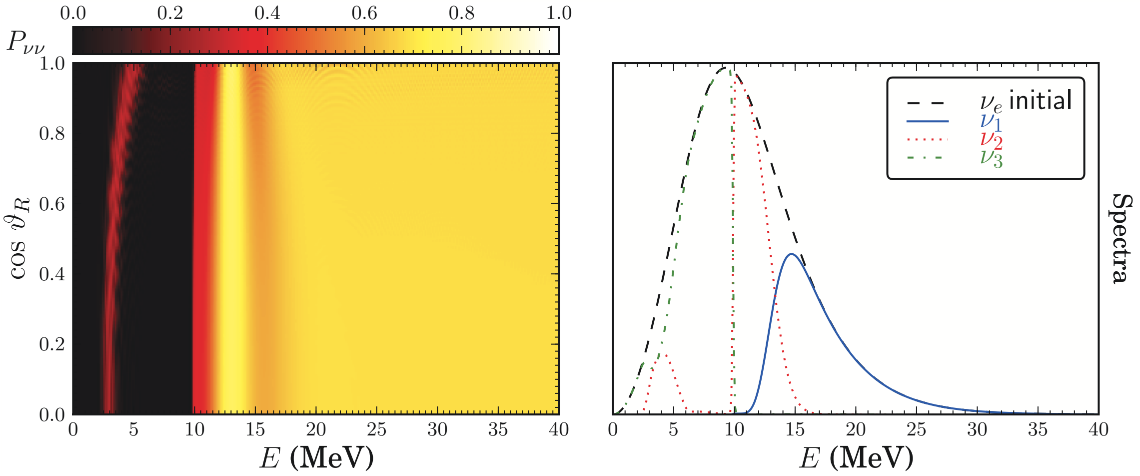

Figure 4.3: Left panel: electron neutrino survival probability $P_{\nu_e\nu_e}$ (color/shading key at top left) for the normal mass hierarchy is shown as a function of cosine of emission angle, $\cos\vartheta_R$, and neutrino energy, E in MeV, plotted at a radius of $r = 5000\,\text{km}$. Right: mass basis (key top right, inset) emission angle-averaged neutrino energy distribution functions versus neutrino energy, E. The dashed curve gives the initial ν_e emission angle-averaged energy spectrum. Movies of this simulation can be found at the URL in Ref. [1]. Each frame of the movie shows a representation of the neutrino survival probability in various different bases at a fixed radius above the core. Each successive frame is 1 km further out from the initial radius of $r_{\text{init}} = 900\,\text{km}$ out to the final radius $r = 5000\,\text{km}$.

$10^{-3}\,\mathrm{eV}^2$. Again, these calculations agree in broad brush with the results obtained for the single-angle simulations reported in Ref. [40]. In our multi-angle simulations the ν_3/ν_2 swap occurs at an energy of $E_\nu \approx 10\,\mathrm{MeV}$. This swap arises from the $\Delta m^2_{\mathrm{atm}}$ splitting. Our simulations show that the second swap, corresponding to ν_2/ν_1, is at an energy of $E_\nu \approx 13.5\,\mathrm{MeV}$. This swap arises from collective oscillations generated by mixing at the $\Delta m^2_\odot$ scale.

In the case of the multi-angle calculation, both of the flavor swaps observed in the normal neutrino mass hierarchy occur at lower energies than their counterparts in the single-angle calculations. Comparing the different simulations I find that for the ν_3/ν_2 swap $E^{\mathrm{multi-angle}}_{\mathrm{swap}} \approx 10.0\,\mathrm{MeV}$ and $E^{\mathrm{single-angle}}_{\mathrm{swap}} \approx 12.5\,\mathrm{MeV}$, and for the ν_2/ν_1 swap $E^{\mathrm{multi-angle}}_{\mathrm{swap}} \approx 13.5\,\mathrm{MeV}$ and $E^{\mathrm{single-angle}}_{\mathrm{swap}} \approx 15.0\,\mathrm{MeV}$.

Interestingly, the inverted neutrino mass hierarchy does not exhibit any change in the observed ν_2/ν_1 swap energy between the multi-angle and the single-angle calculations. The spectra I observe for the multi-angle calculations in the inverted neutrino mass hierarchy agree with the framework developed by Ref. [78]. In that work, a single-angle toy model calculation showed that the resultant spectra of the neutronization neutrino burst for an O-Ne-Mg core-collapse supernova was formed by an initial phase of non-adiabatic, synchronous MSW flavor transformation, followed by collective neutrino oscillations that form the swaps observed in the simulations.

The normal neutrino mass hierarchy case is quite different. The final spectra in Fig. 4.3 show that there are $\sim 10\%$ fewer neutrinos that remain in mass state 3. This implies that the flavor evolution in the multi-angle calculation was less adiabatic than that in the single-angle calculation.

To illustrate the importance of using full 3×3 flavor mixing in the case of an O-Ne-Mg core-collapse supernova, I have performed a 2×2 multi-angle calculation for each mixing scale in the normal neutrino mass hierarchy. Briefly, the swap energy of the $\Delta m^2_{\mathrm{atm}}$ mixing scale is $E_{\mathrm{swap}} \approx 10.0\,\mathrm{MeV}$ in our 2×2 multi-angle calculation, which corresponds closely with the swap energy found in the 3×3 multi-angle flavor mixing case. However, the swap energy of the $\Delta m^2_\odot$ mixing scale is found to be $E_{\mathrm{swap}} \approx 11.0\,\mathrm{MeV}$ for the 2×2 multi-angle calculation,

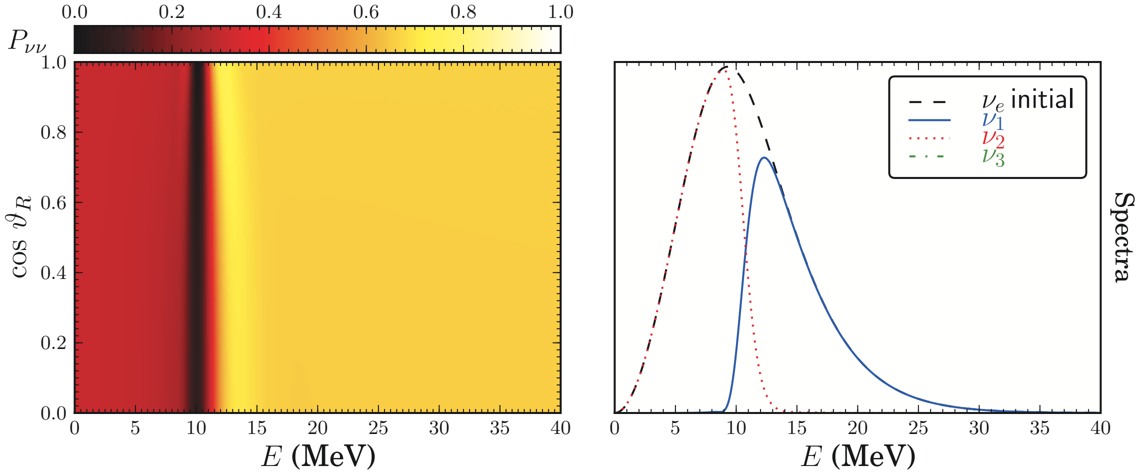

Figure 4.4: This calculation of the flavor evolution of neutrinos in the inverted mass hierarchy was conducted with values of $\Delta m^2_\odot = 7.6 \times 10^{-5}\,\mathrm{eV}^2$ and $\Delta m^2_{\mathrm{atm}} = -2.4 \times 10^{-3}\,\mathrm{eV}^2$. Left panel: electron neutrino survival probability $P_{\nu_e\nu_e}$ (color/shading key at top left) for the inverted mass hierarchy is shown as a function of cosine of emission angle, $\cos\vartheta_{\mathrm{R}}$, and neutrino energy, E in MeV, plotted at a radius of $r = 5000\,\mathrm{km}$. Right: mass basis (key top right, inset) emission angle-averaged neutrino energy distribution functions versus neutrino energy, E. The dashed curve gives the initial ν_{e} emission angle-averaged energy spectrum.

which is lower than the corresponding ν_2/ν_1 swap $E_{\mathrm{swap}} \approx 13.5\,\mathrm{MeV}$ of the 3×3 multi-angle calculation.

4.2.2 Sensitivity to Neutrino Mass-Squared Differences

Since the publication of the original set of papers on the neutronization neutrino burst of an O-Ne-Mg core-collapse supernova [40, 78], the experimental limits on $\Delta m^2_\odot$ and $\Delta m^2_{\mathrm{atm}}$ have been refined, resting currently at the values of $\Delta m^2_\odot = 7.6 \times 10^{-5}\,\mathrm{eV}^2$ and $\Delta m^2_{\mathrm{atm}} = 2.4 \times 10^{-3}\,\mathrm{eV}^2$ [62]. I have conducted a set of 3×3 multi-angle calculations to ascertain the effect the new experimental constraints would have on the flavor evolution history of the neutrinos released in the neutronization burst. Figure 4.4 shows the results of our calculations for neutrino flavor transformation in the inverted neutrino mass hierarchy. There is no significant change observed in the final state of neutrinos at a radius of $r = 5000\,\mathrm{km}$ relative to our earlier calculations with $\Delta m^2_{21} = 8.0 \times 10^{-5}\,\mathrm{eV}^2$.

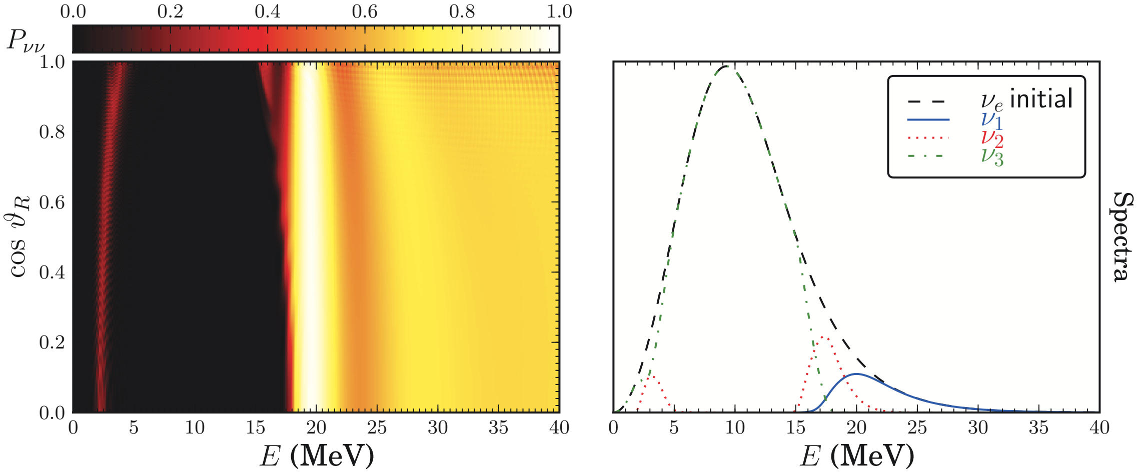

Figure 4.5: This calculation of the flavor evolution of neutrinos in the normal mass hierarchy was conducted with values of $\Delta m^2_{\odot} = 7.6 \times 10^{-5}\,\mathrm{eV}^2$ and $\Delta m^2_{\mathrm{atm}} = 2.4 \times 10^{-3}\,\mathrm{eV}^2$. Left panel: electron neutrino survival probability $P_{\nu_e\nu_e}$ (color/shading key at top left) for the normal mass hierarchy is shown as a function of cosine of emission angle, $\cos\vartheta_{\mathrm{R}}$, and neutrino energy, E in MeV, plotted at a radius of $r = 5000\,\mathrm{km}$. Right: mass basis (key top right, inset) emission angle-averaged neutrino energy distribution functions versus neutrino energy, E. The dashed curve gives the initial ν_e emission angle-averaged energy spectrum.

Figure 4.5 shows the results of our calculations for neutrino flavor transformation in the normal neutrino mass hierarchy with the latest mass-squared values. With the new neutrino mixing parameters there is an increase in the observed swap energies for mixing at both the $\Delta m^2_{\odot}$ and $\Delta m^2_{\mathrm{atm}}$ scales over the cases with the original mixing parameters adopted in [40]. The ν_3/ν_2 swap occurs at an energy of $E_\nu \approx 16.5\,\mathrm{MeV}$, while the ν_2/ν_1 swap is pushed even higher to an energy of $E_\nu \approx 19.0\,\mathrm{MeV}$, as opposed to $E_\nu \approx 10.0\,\mathrm{MeV}$ and $E_\nu \approx 13.5\,\mathrm{MeV}$ respectively.

Because detection and characterization of supernova neutrinos is the ultimate aim of research in this field, I have included Fig. 4.6 and Fig. 4.7 to show predictions for the flux of electron neutrinos emitted by the neutronization neutrino burst of an O-Ne-Mg core collapse supernova. Figure 4.6 shows the predictions of both the single-angle and multi-angle calculations for the normal neutrino mass hierarchy, while Fig. 4.7 shows the same for the inverted neutrino mass hierarchy.

4.2.3 Variation of θ_{13}

Of particular interest is the effect produced by a significantly decreased θ_{13} mixing angle. As has been found in previous work, reducing the value of θ_{13} can affect sensitively the energy of the flavor swap at the $\Delta m^2_{\mathrm{atm}}$ scale for the normal neutrino mass hierarchy [35]. I performed a new calculation that matched the initial conditions of the primary, ν_{e} only, simulation of the neutronization burst, but this time with a value of $\theta_{13} = 1.0 \times 10^{-3}$, two orders of magnitude smaller than the θ_{13} value in the original calculation. This new value of θ_{13} drives the neutrino background-enhanced flavor evolution at the $\Delta m^2_{\mathrm{atm}}$ scale entirely non-adiabatic, and Fig. 4.8 shows that this produces a resultant neutrino energy spectrum that is essentially indistinguishable from the spectrum produced in our calculations for the inverted neutrino mass hierarchy. This may present complications in the future determination of the neutrino mass hierarchy and θ_{13} using the neutronization pulse of an O-Ne-Mg core-collapse supernova. Planned earth-based experiments should be able to set an upper limit on the value of $\sin^2 2\theta_{13} \sim 1.0 \times 10^{-2}$ [82]. The neutronization neutrino burst signal from an O-Ne-Mg core-collapse supernova may have limited ability to discern a value of θ_{13} much below this threshold. On

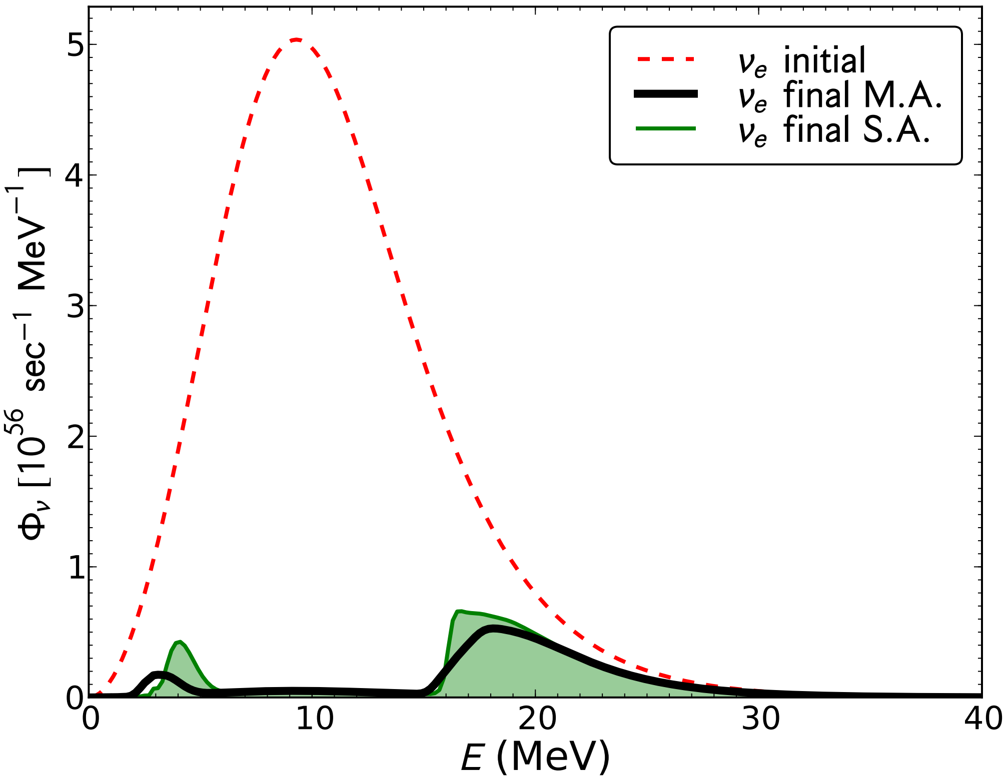

Figure 4.6: Emission angle-averaged electron neutrino flux Φ_ν (key top right, inset) for the normal neutrino mass hierarchy is shown as a function of neutrino energy E in MeV. The dashed curve gives the initial ν_{e} emission angle-averaged neutrino flux. The shaded region gives the predicted flux in a single-angle calculation, and the thick line shows the flux predicted by the multi-angle calculation. These calculations of electron neutrino flux are done using $\Delta m^2_\odot = 7.6 \times 10^{-5}\,\mathrm{eV}^2$ and $\Delta m^2_{\mathrm{atm}} = -2.4 \times 10^{-3}\,\mathrm{eV}^2$ and $\theta_{13} = 0.1$.

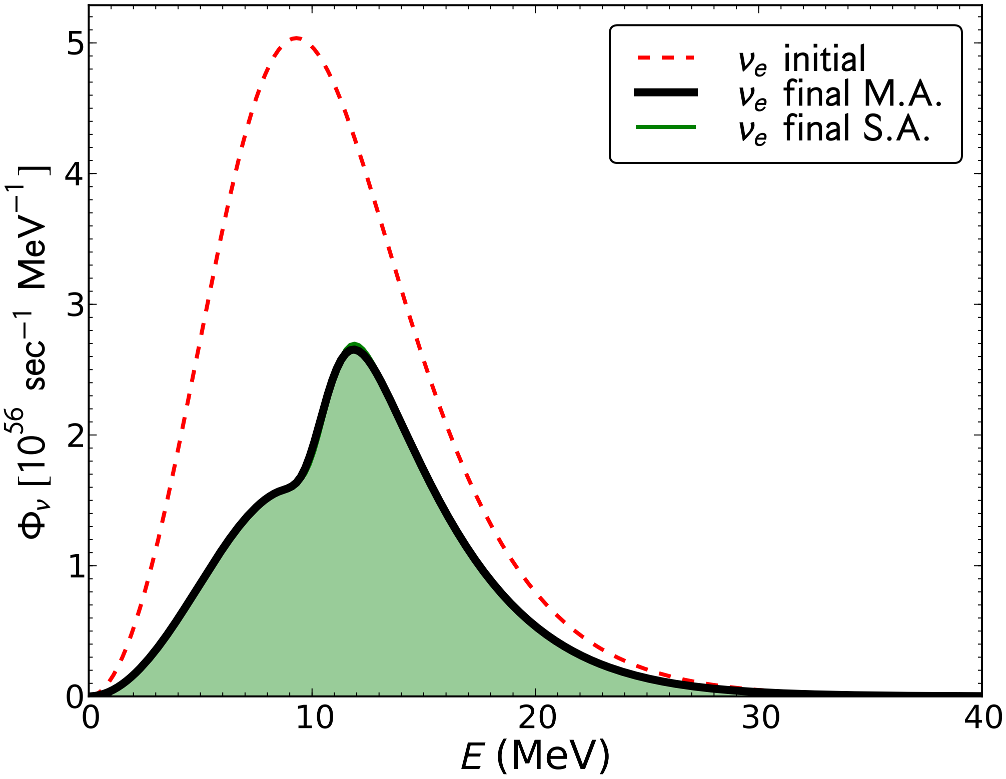

Figure 4.7: Emission angle-averaged electron neutrino flux Φ_ν (key top right, inset) for the inverted neutrino mass hierarchy is shown as a function of neutrino energy E in MeV. The dashed curve gives the initial ν_e emission angle-averaged neutrino flux. The shaded region gives the predicted flux in a single-angle calculation, and the thick line shows the flux predicted by the multi-angle calculation. These calculations of electron neutrino flux are done using $\Delta m^2_\odot = 7.6 \times 10^{-5}\,\mathrm{eV}^2$ and $\Delta m^2_{\mathrm{atm}} = -2.4 \times 10^{-3}\,\mathrm{eV}^2$ and $\theta_{13} = 0.1$.

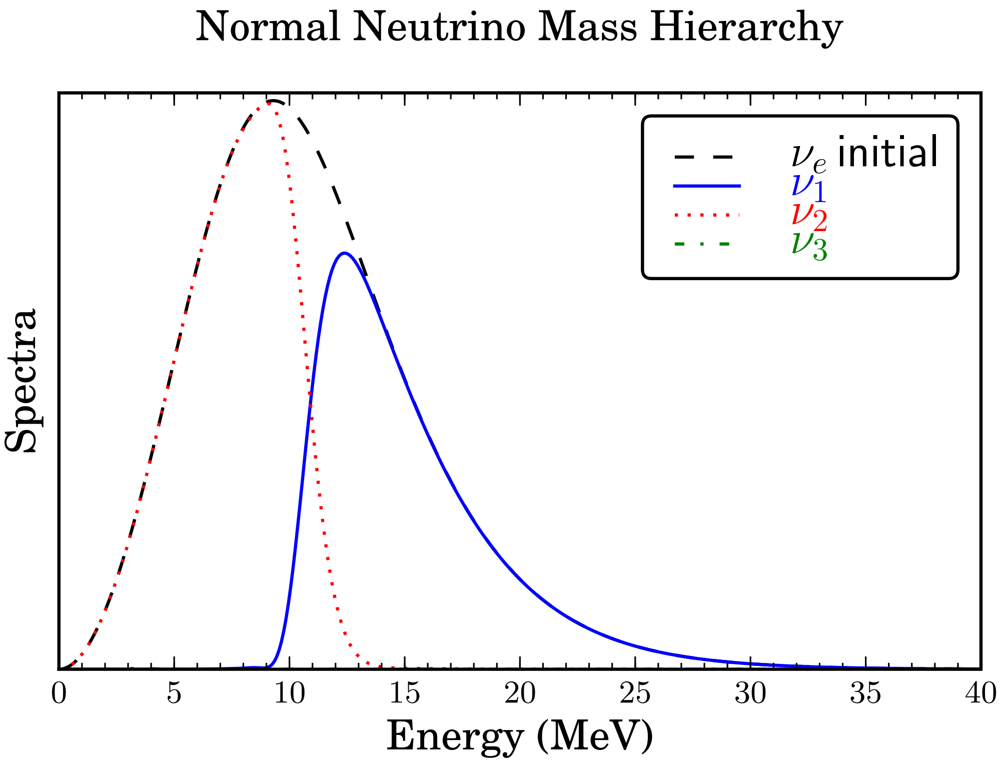

Figure 4.8: Emission angle-averaged neutrino energy distribution functions versus neutrino energy plotted in the neutrino mass basis for the 3×3 multi-angle calculation of neutrino flavor evolution. This calculation employs a significantly reduced value of $\theta_{13} = 1.0 \times 10^{-3}$. This mixing angle is associated with flavor transformation at the $\Delta m^2_{\mathrm{atm}}$ scale. Results shown at a radius of $r = 5000$km.

the other hand, the late-time supernova neutrino signal, which should be more or less generic for all core-collapse supernovae, has no such limitations. Detection of the sense of the swap in this case should provide an unambiguous determination of the neutrino mass hierarchy. Measurements like these could be complementary to laboratory based neutrino mass probes. For example, experiments such as the MAJORANA project may be able to determine the neutrino mass hierarchy directly [83].

4.3 Density Fluctuation Effects

To study why theoretical predictions of the neutrino mass state hopping rate differ from what is observed in our simulations I chose to vary only a single parameter in our model of the O-Ne-Mg supernova, the matter density profile. This affords us an opportunity to conduct an interesting side investigation. I explore the possibility that the neutrino signal from this model could be used to detect features in the matter density profile of the supernova, assuming a knowledge of neutrino mixing parameters.

Terrestrial experiments, like the proposed long baseline neutrino experiments, hold great promise for revealing key neutrino flavor mixing parameters, such as the value of θ_{13} and the neutrino mass hierarchy. These as yet unmeasured quantities influence how neutrinos change their flavors in the core collapse supernova environment.

If experiments can reveal neutrino mixing parameters, it stands to reason that the signal from a supernova could be used as a probe of supernova physics. There is a rich physical interplay between the hydrodynamic motion and nuclear abundances in a supernova and the neutrino flux streaming out from the proto-neutron star at it's heart. Armed with a refined understanding of neutrino flavor transformation physics, it is reasonable to ask whether the supernova neutrino signal could be used as a probe of the matter density profile in a supernova at times and depths that are impossible to measure with optical observations.

For the purposes of this study I have chosen the following neutrino mixing parameters: neutrino mass squared differences $\Delta m_{\odot}^2 = 7.6 \times 10^{-5}\,\mathrm{eV}^2$, $\Delta m_{\mathrm{atm}}^2 = 2.4 \times 10^{-3}\,\mathrm{eV}^2$; vacuum mixing angles $\theta_{12} = 0.59$, $\theta_{23} = \pi/4$, $\theta_{13} = 0.1$; and CP-violating phase $\delta = 0$. Here I will concentrate on the normal neutrino mass hierarchy. Along with this I model the neutronization neutrino burst to be of pure electron flavor and have a Fermi-Dirac spectrum with average energy $\langle E_\nu \rangle = 11\,\mathrm{MeV}$, a degeneracy parameter $\eta = 3$, and luminosity $L = 1.0 \times 10^{53}\,\mathrm{erg\,s^{-1}}$. Previous simulations [44] and semi-analytic work [40, 78] agree broadly on the theoretical framework that should describe the flavor evolution of neutrinos in this case.

4.3.1 Neutrino Flavor Transformation With and Without Matter Fluctuations

For our particular model, neutrinos emerging from the neutrinosphere initially are in pure electron flavor states. As these neutrinos stream outward through the envelope, a collective effect known as the "Neutrino Enhanced MSW" effect (not to be confused with the MSW, Mikheyev-Smirnov-Wolfenstein effect) can produce mass state hopping of neutrinos out of the heaviest mass eigenstate (for both neutrino mass hierarchies) when matter densities are large. Nominally, the hopping rate is set by a comparison of the scale height of the matter density and a characteristic neutrino oscillation length in the resonance region. When matter densities fall further, a second collective effect called the "Regular Precession Mode" begins. All neutrinos in this mode begin to rotate around an effective field in flavor space at the same frequency, regardless of their energy. Because of the ν_e only emission of the neutronization neutrino burst, this process conserves the total number of neutrinos occupying each mass eigenstate and produces the distinctive "Flavor Swaps" or "Spectral Swaps" seen in the final neutrino spectra.

This last point is extremely important. By conserving the number of neutrinos in each mass state, the flavor swaps freeze the flavor evolution history of the neutrinos into the final spectrum with a signature that stands out dramatically to an observer here on Earth. This suggests that such an observer might be able to simply measure the swap energies in a detected supernova neutrino signal and work backward to construct an in-situ measurement of the matter density profile at high densities.

Because the neutronization neutrino burst of an O-Ne-Mg supernova has been well studied and is a relatively simple case of flavor swap formation, it serves as a good test case to study our ability to extract information about the supernova envelope from a detected neutrino burst signal. For the inverted neutrino mass hierarchy, the sequence of events of neutrino flavor transformation produce only a single swap because only one mass state level crossing is present [40, 78, 44]. For the normal neutrino mass hierarchy, two swaps are produced because two separate level crossing populate all three mass eigenstates with neutrinos (for small θ_{13} this can be reduced to a single swap via the complete depopulation of mass state 3) [40, 78, 44].

The density profile used for this study comes from a set of simulations by Nomoto [2, 3]. This profile is typical of what a mid-collapse O-Ne-Mg supernova might produce at the epoch of the neutronization neutrino burst, $\sim 10\,\mathrm{ms}$ post bounce. A feature that this profile possesses is a small bump in the matter density which is created by the star's helium burning shell in a range of radius bounded by $r \simeq 1080\,\mathrm{km} - 1100\,\mathrm{km}$. This feature is known to cause neutrinos at low energies to pass through multiple MSW resonances at the $\Delta m^2_{\mathrm{atm}}$ mass scale, and has been discussed in [40, 78, 44].

To test our ability to detect a simple feature such as this, I conducted a pair of simulations. The first with the original density profile, called "Bump", and the second with a synthetic density profile where the He burning shell feature has been removed, called "No Bump". Figure 4.9 shows the electron number densities with these two profiles plotted side by side. For the neutrino-electron forward scattering potential H_{e} (hereafter the "matter" potential) the associated scale height at resonance is,

$$\mathcal{H} = \left| \frac{1}{H_{\mathrm{e}}} \frac{dH_{\mathrm{e}}}{dr} \right|^{-1}_{\mathrm{res}} . \tag{4.6}$$

Figure 4.10 shows the matter potential scale height for both profiles, evaluated at the MSW resonance location for each neutrino energy bin.

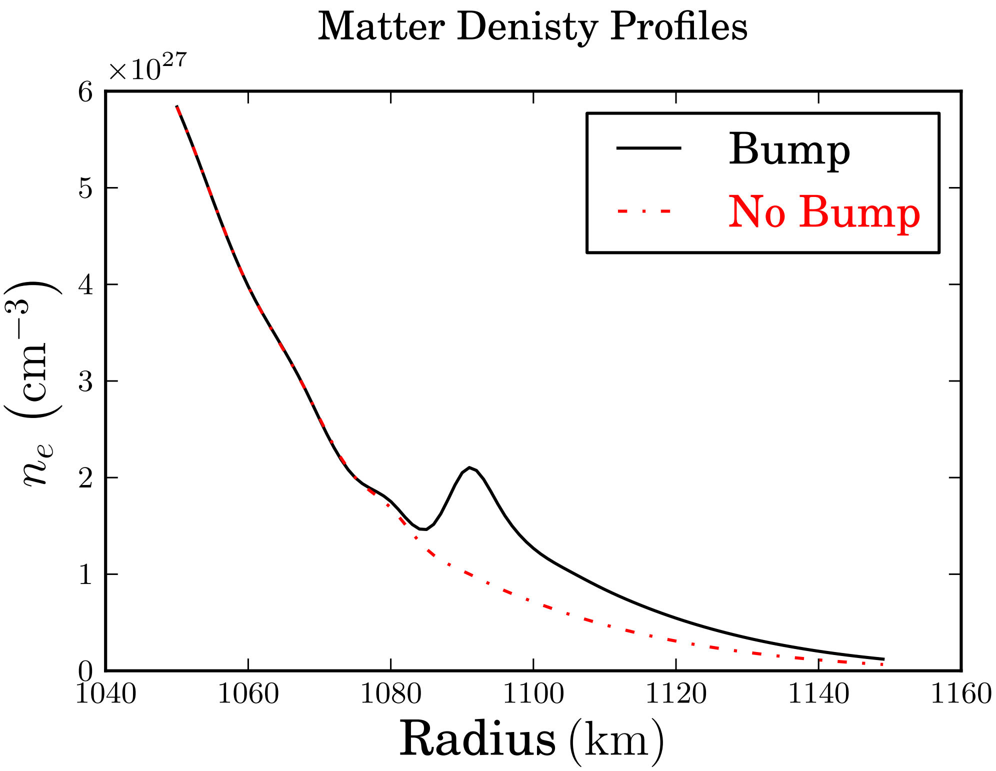

Figure 4.9: The electron number density for two matter profiles plotted as functions of radius in the resonance region for the $\Delta m^2_{\rm atm}$ mass state splitting. The solid line indicates the original matter density profile of Refs. [2, 3], called Bump. The dashed-dotted line indicates the artificial density profile with the bump artificially removed, called No Bump.

Figures 4.11 and 4.12 show the results of our calculations for the flavor transformation of electron neutrinos emitted during the neutronization neutrino burst. Figure 4.11 shows the results of the original, Bump, density profile. Figure 4.12 shows the results of a simulation using the No Bump density profile.

The aim of the second simulation, with the No Bump density profile, was to study whether one could detect a signature from features of the matter density profile using the neutrino flavor transformation signal. Post processing of this data led to a surprise. The total number of neutrinos that remain in the heavy mass eigenstate decreases when the bump in the density profile is removed. Explicitly, the heavy mass eigenstate (mass state 3) survival probability, $P_{\rm H}$, for the two

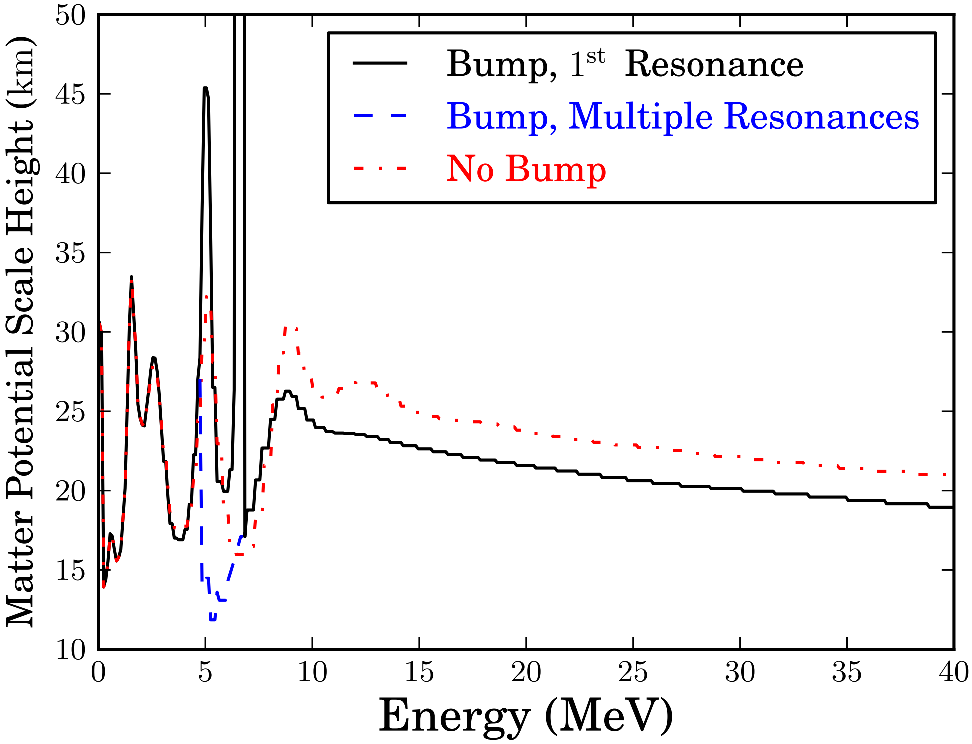

Figure 4.10: The scale height of the neutrino-electron forward scattering potential evaluated at the MSW resonance location for each neutrino energy. The solid line indicates the first MSW resonance scale height of neutrinos moving through the original matter density profile of Refs. [2, 3], while the dashed line indicates the scale heights of the multiple resonances. The dash-dotted line indicates the MSW resonance scale heights of neutrinos moving through the No Bump density profile.

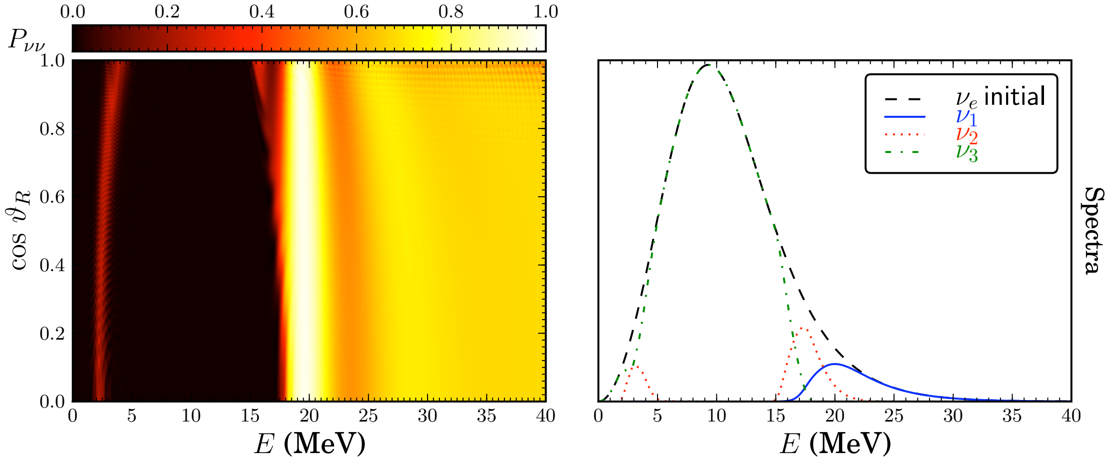

Figure 4.11: Bump. Left panel: electron neutrino survival probability $P_{\nu_e\nu_e}$ (color/shading key at top left) for the normal mass hierarchy is shown as a function of cosine of emission angle, $\cos\vartheta_{\mathrm{R}}$, and neutrino energy, E in MeV, plotted at a radius of $r = 5000\,\mathrm{km}$. Right: mass basis (key top right, inset) emission angle-averaged neutrino energy distribution functions versus neutrino energy, E. The dashed curve gives the initial ν_{e} emission angle-averaged energy spectrum. A kink in the density profile used, taken from Refs. [2, 3], leads to multiple MSW resonances for low energy neutrinos.

cases are $P_{\mathrm{H}}^{\mathrm{Bump}} = 0.852$ and $P_{\mathrm{H}}^{\mathrm{No\ Bump}} = 0.759$. This is a counterintuitive result. I expected that the removal of the bump from the original density profile would have produced flavor evolution that was more adiabatic, leading to a greater survival probability for the No Bump profile.

The effect that the removal of the helium burning shell has on the ν_{e} survival probability is shown in Figure 4.13. Note in this figure that there is an enhanced survival probability for ν_{e}'s at low energy for the Bump profile, and that the flavor swap energy is lowered for neutrinos in the No Bump profile.

Collective flavor evolution prior to the onset of the regular precession mode was thought to be described by the Synchronous MSW effect, as opposed to the Neutrino Enhanced MSW effect [40, 78, 44]. While there is a technical difference between these two modes of neutrino flavor transformation, the neutrino flavor transformation survival probabilities (and consequently the Swap energies) are quite similar for both cases, which led to the initial confusion. In both cases the resultant value of P_{H} is determined by the evolution of a single representative

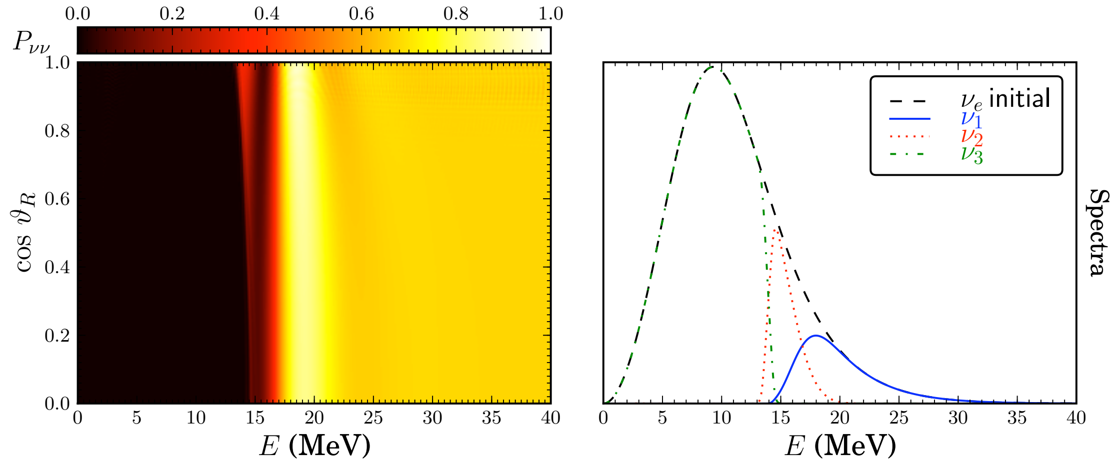

Figure 4.12: No Bump. Left panel: electron neutrino survival probability $P_{\nu_e\nu_e}$ (color/shading key at top left) for the normal mass hierarchy is shown as a function of cosine of emission angle, $\cos\vartheta_{\mathrm{R}}$, and neutrino energy, E in MeV, plotted at a radius of $r = 5000\,\mathrm{km}$. Right: mass basis (key top right, inset) emission angle-averaged neutrino energy distribution functions versus neutrino energy, E. The dashed curve gives the initial ν_{e} emission angle-averaged energy spectrum. The kink in the density profile taken from Refs. [2, 3], has been artificially removed from the density profile used in this simulation.

neutrino flavor state, which is the flavor state of the collective ensemble of neutrinos. Ideally, neutrinos remain so closely aligned with this collective flavor state that they do not "feel" the neutrino self coupling potential and, as a result, they behave as a single neutrino experiencing the matter-driven MSW effect.

We have mentioned previously that this paper considers only flavor transformation using the normal neutrino mass hierarchy. This choice was motivated by the Bump density feature I consider in this paper, which is significant for flavor transformation at the $\Delta m^2_{\mathrm{atm}}$ neutrino mass splitting for neutrinos with typical neutronization burst energies, $\sim 10\,\mathrm{MeV}$. Previously, it has been found that in the neutronization burst of an O-Ne-Mg core-collapse supernova, the atmospheric mass squared splitting experiences no neutrino flavor transformation in the inverted neutrino mass hierarchy [44]. Because of this, the presence or absence of the Bump density feature has no effect on the flavor transformation for neutrinos in the inverted mass hierarchy, leaving the final emission spectra identical to those already presented in [44]

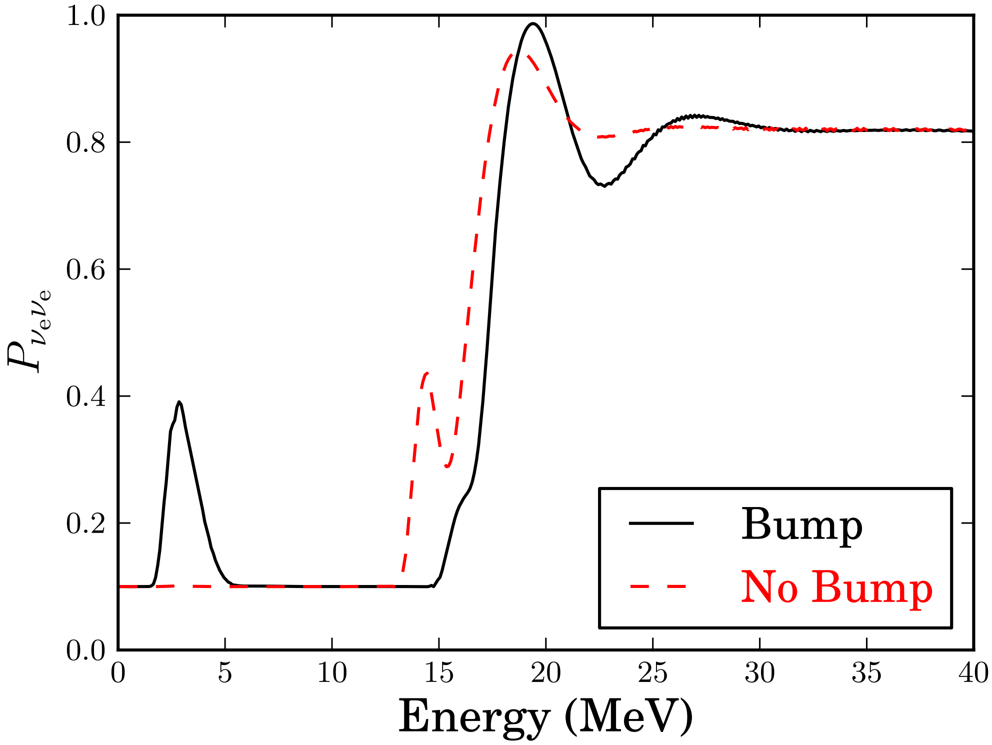

Figure 4.13: The electron neutrino survival probability as a function of neutrino energy shown at the final radius $r = 5000\,\mathrm{km}$. The solid line indicates the survival probability for neutrinos after moving through the Bump profile, while the dashed line indicates the survival probability for neutrinos after moving through the No Bump profile.

4.3.2 Theory

For our simulations I assume a pure ν_e burst emitted from the neutrino sphere ar $R_\nu = 60\,\mathrm{km}$ with a total luminosity of $L_\nu = 10^{53}\,\mathrm{erg\,s^{-1}}$ and a normalized spectrum

$$f_\nu\left(E\right) = \frac{1}{F_2\left(\eta_\nu\right) T_\nu^3} \frac{E^2}{\exp\left(E/T_\nu - \eta_\nu\right) + 1}, \tag{4.7}$$

where $\eta_\nu = 3$ and $T_\nu = 2.75\,\mathrm{MeV}$. This corresponds to an average ν_e energy $\langle E_\nu \rangle = F_3\left(\eta_\nu\right) T_\nu / F_2\left(\eta_\nu\right) = 11\,\mathrm{MeV}$. Here

$$F_n\left(\eta_\nu\right) = \int_0^\infty \frac{x^n}{\exp\left(x - \eta_\nu\right) + 1} dx\ . \tag{4.8}$$

In the single-angle approximation, the effective total neutrino number density at $r > R_\nu$ is

$$n_\nu(r) = \frac{L_\nu}{4\pi R_\nu^2 \langle E_\nu \rangle} \left[1 - \sqrt{1 - (R_\nu/r)^2} \right]^2 \approx \frac{L_\nu R_\nu^2}{16\pi \langle E_\nu \rangle r^4} \, , \tag{4.9}$$

where the approximate equality holds for $r \gg R_\nu$, and where I set $\hbar = c = 1$.

Because the salient features of our results are confined to the $\delta m^2_{\mathrm{atm}}$ mass squared mixing scale, I will confine the following discussion to a two neutrino flavor mixing scheme. Following the convention of [32], one takes each neutrino flavor state with energy E_ν and represent it as a three dimensional neutrino flavor isospin (NFIS),

$$\mathbf{s}_\omega = \begin{cases} \hat{\mathbf{e}}^{\mathrm{f}}_{\mathrm{z}}/2, & \text{for } \nu_{\mathrm{e}}, \\ -\hat{\mathbf{e}}^{\mathrm{f}}_{\mathrm{z}}/2, & \text{for } \nu_{\mathrm{x}}, \end{cases} \tag{4.10}$$

where $\hat{\mathbf{e}}^{\mathrm{f}}_{\mathrm{z}}$ is the unit vector in the z-direction for the neutrino flavor basis and ω is the vacuum oscillation frequency $\omega = \delta m^2_{\mathrm{atm}}/2E_\nu$. I focus on the normal mass hierarchy and I take the effective vacuum mixing angle $\theta_{\mathrm{v}} \approx \theta_{13} = 0.1$. The evolution of a NFIS $\mathbf{s}_\omega$ is governed by

$$\frac{d}{dr}\mathbf{s}_\omega = \mathbf{s}_\omega \times \left[\omega \mathbf{H}_{\mathrm{v}} + \mathbf{H}_{\mathrm{e}} - \mu(r) \int_0^\infty \mathbf{s}_{\omega'} f_\nu(E_{\omega'}) \, dE_{\omega'} \right] \, , \tag{4.11}$$

where $\mathbf{H}_{\mathrm{v}} = \cos 2\theta_{\mathrm{v}} \hat{\mathbf{e}}^{\mathrm{f}}_{\mathrm{z}} - \sin 2\theta_{\mathrm{v}} \hat{\mathbf{e}}^{\mathrm{f}}_{\mathrm{x}}$, $\mathbf{H}_{\mathrm{e}} = -\sqrt{2} G_{\mathrm{F}} n_{\mathrm{e}}(r) \hat{\mathbf{e}}^{\mathrm{f}}_{\mathrm{z}}$, $\mu(r) = 2\sqrt{2} G_{\mathrm{F}} n_\nu(r)$, and $E_{\omega'} = \delta m^2_{\mathrm{atm}}/2\omega'$.

In what follows, I leave out radiative vertex corrections to $\mathbf{H}_{\mathrm{e}}$. These corrections are discussed in Refs. [84, 85, 24, 86]. I have done numerical calculations that show these corrections do not change the qualitative nature of the effects discussed below.

For convenience, I define

$$g(\omega) \equiv \frac{\delta m^2_{\mathrm{atm}}}{2\omega} f_\nu(E_\omega) \tag{4.12}$$

and

$$\mathbf{S} \equiv \int_0^\infty \mathbf{s}_\omega f_\nu(E_\omega) \, dE_\omega = \int_0^\infty \mathbf{s}_\omega g(\omega) \, d\omega \, . \tag{4.13}$$

It follows from Eqns. (4.11)-(4.13) that

$$\frac{d}{dr}\mathbf{S} = \int_0^\infty \omega g(\omega) \mathbf{s}_\omega d\omega \times \mathbf{H}_{\mathrm{v}} + \mathbf{S} \times \mathbf{H}_{\mathrm{e}} \, . \tag{4.14}$$

As $g(\omega)$ is concentrated in a finite range of ω, to zeroth order one approximates $g(\omega) \approx \delta(\omega - \langle\omega\rangle)$, where $\langle\omega\rangle = \int_0^\infty \omega g(\omega)\, d\omega$. This is a fair approximation for the particular case we are treating, namely, low energy ν_e's in the neutronization burst ($\langle E_\nu \rangle = 11\,\mathrm{MeV}$). With this approximation, the zeroth-order mean field $\mathbf{S}^{(0)}$ is defined through

$$\frac{d}{dr}\mathbf{S}^{(0)} = \mathbf{S}^{(0)} \times \left[\langle\omega\rangle \mathbf{H}_\mathrm{v} + \mathbf{H}_\mathrm{e}\right] \equiv \mathbf{S}^{(0)} \times \mathbf{H}_\mathrm{MSW} \ . \tag{4.15}$$

The evolution of $\mathbf{S}^{(0)}$ is the behavior of the system in the high luminosity, "Synchronized", limit. (In the Synchronous MSW effect, all $\mathbf{s}_\omega$ are aligned with $\mathbf{S}$, and orbit around it. Note, this idealized situation does not occur in the presence of matter [33].) For the neutronization neutrino burst luminosity and matter density profile I use, our calculations take place below this luminosity regime. I do not observe individual $\mathbf{s}_\omega$ orbiting $\mathbf{S}$ [87], but I do observe that individual $\mathbf{s}_\omega$ remain closely aligned to $\mathbf{S}$ and $\mathbf{S}^{(0)}$.

The evolution of $\mathbf{S}^{(0)}$ is the same as that of an idealized ν_e with $E_\nu = \delta m^2_\mathrm{atm}/2\langle\omega\rangle = 8.53\,\mathrm{MeV}$ undergoing the usual MSW effect. This is the collective NFIS that all the the neutrinos will follow during the Neutrino Enhanced MSW effect. Now we can approximately solve for the evolution of $\mathbf{s}_\omega$ from

$$\frac{d}{dr}\mathbf{s}_\omega \approx \mathbf{s}_\omega \times \left[\omega \mathbf{H}_\mathrm{v} + \mathbf{H}_\mathrm{e} - \mu(r)\, \mathbf{S}^{(0)}\right] \ . \tag{4.16}$$

We can use the solution of Equation 4.15 to obtain the first-order mean field $\mathbf{S}^{(1)}$ from the definition of $\mathbf{S}$ in the first expression in Equation 4.13, and then recalculate the evolution of $\mathbf{s}_\omega$ from the above Equation 4.15 but with $\mathbf{S}^{(1)}$ replacing $\mathbf{S}^{(0)}$. This procedure can be repeated until the results converge.

Of course, the procedure outlined above is not recommended as a numerical method, but instead points to an analytic approach to understand collective oscillations. Based on the MSW effect, $\mathbf{S}^{(0)}$ goes through resonance at $n_\mathrm{e} \approx 1.09 \times 10^{27}\,\mathrm{cm}^{-3}$ corresponding to $r \approx 1100\,\mathrm{km}$ in both simulations. For simplicity, let us consider a smooth distribution for $n_\mathrm{e}(r)$. Before the resonance,

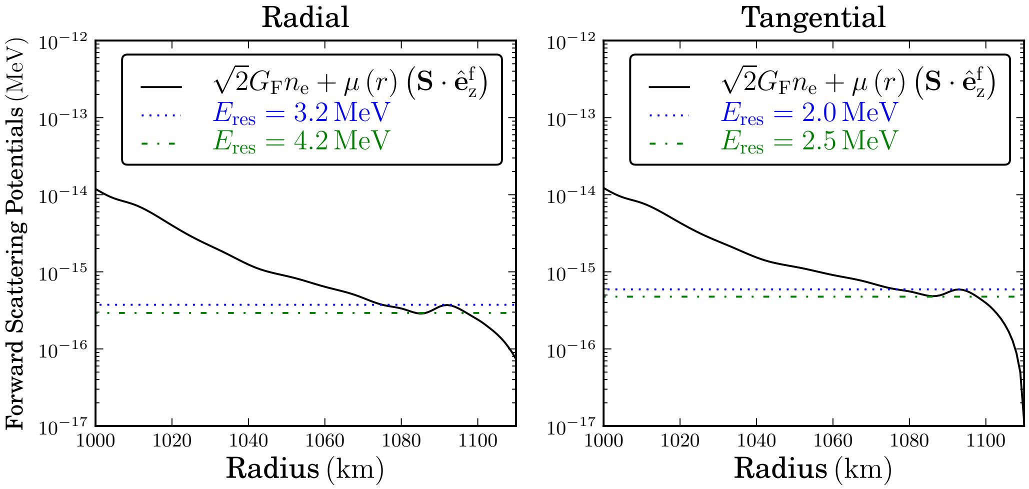

Figure 4.14: Left panel: the combined matter and neutrino self-coupling forward scattering potentials experienced by radially emitted neutrinos as a function of radius. Right: the combined matter and neutrino self-coupling forward scattering potentials experienced by tangentially emitted neutrinos as a function of radius. The dotted and dashed-dotted lines indicate the upper and lower neutrino energies, respectively, to experience multiple neutrino-background enhanced MSW resonances in the desynchronized limit.

the evolution of $\mathbf{S}^{(0)}$ is somewhat adiabatic and we can take

$$\begin{aligned}\mathbf{S}^{(0)} &\approx -\frac{\mathbf{H}_{\mathrm{MSW}}}{2|\mathbf{H}_{\mathrm{MSW}}|} &(4.17)\\ &\approx -\frac{1}{2}\left(\cos 2\theta_{\mathrm{m}}\hat{\mathbf{e}}^{\mathrm{f}}_{\mathrm{z}} - \sin 2\theta_{\mathrm{m}}\hat{\mathbf{e}}^{\mathrm{f}}_{\mathrm{x}}\right) \ , &(4.18)\end{aligned}$$

where

$$\cos 2\theta_{\mathrm{m}} = \frac{\langle\omega\rangle\cos 2\theta_{\mathrm{v}} - \sqrt{2}G_{\mathrm{F}}n_{\mathrm{e}}}{\sqrt{\left(\langle\omega\rangle\cos 2\theta_{\mathrm{v}} - \sqrt{2}G_{\mathrm{F}}n_{\mathrm{e}}\right)^2 + \left(\langle\omega\rangle\sin 2\theta_{\mathrm{v}}\right)^2}} \quad , \tag{4.19}$$

$$\sin 2\theta_{\mathrm{m}} = \frac{\langle\omega\rangle\sin 2\theta_{\mathrm{v}}}{\sqrt{\left(\langle\omega\rangle\cos 2\theta_{\mathrm{v}} - \sqrt{2}G_{\mathrm{F}}n_{\mathrm{e}}\right)^2 + \left(\langle\omega\rangle\sin 2\theta_{\mathrm{v}}\right)^2}} \quad . \tag{4.20}$$

The evolution of $\mathbf{s}_\omega$ at densities higher than the resonance density for $\mathbf{S}^{(0)}$ is then governed by

$$\frac{d}{dr}\mathbf{s}_\omega \approx \mathbf{s}_\omega \times \left[\left(\omega\cos 2\theta_{\mathrm{v}} - \sqrt{2}G_{\mathrm{F}}n_{\mathrm{e}} + \frac{\mu}{2}\cos 2\theta_{\mathrm{m}}\right)\hat{\mathbf{e}}^{\mathrm{f}}_{\mathrm{z}} - \left(\omega\sin 2\theta_{\mathrm{v}} + \frac{\mu}{2}\sin 2\theta_{\mathrm{m}}\right)\hat{\mathbf{e}}^{\mathrm{f}}_{\mathrm{x}}\right] \tag{4.21}$$

$$\equiv \mathbf{s}_\omega \times \mathbf{H}_\omega \ . \tag{4.22}$$

This equation also defines $\mathbf{H}_\omega$. Note that the NFIS evolution described by this equation is similar to the usual MSW effect but with modified diagonal and off-diagonal terms. Note especially that the off-diagonal term $(\mu/2)\sin 2\theta_{\mathrm{m}} = \mu/2$ is large at the resonance location for $\mathbf{S}^{(0)}$. If $\mathbf{s}_\omega$ evolves adiabatically, then

$$\begin{aligned}\mathbf{s}_\omega &\approx -\frac{\mathbf{H}_\omega}{2|\mathbf{H}_\omega|} &(4.23)\\ &\approx -\frac{1}{2}\left(\cos 2\theta_\omega\hat{\mathbf{e}}^{\mathrm{f}}_{\mathrm{z}} - \sin 2\theta_\omega\hat{\mathbf{e}}^{\mathrm{f}}_{\mathrm{x}}\right) \ , &(4.24)\end{aligned}$$

where

$$\cos 2\theta_\omega = \frac{\langle\omega\rangle\cos 2\theta_{\mathrm{v}} - \sqrt{2}G_{\mathrm{F}}n_{\mathrm{e}} + (\mu/2)\cos 2\theta_{\mathrm{m}}}{\sqrt{\left(\langle\omega\rangle\cos 2\theta_{\mathrm{v}} - \sqrt{2}G_{\mathrm{F}}n_{\mathrm{e}} + (\mu/2)\cos 2\theta_{\mathrm{m}}\right)^2 + \left(\langle\omega\rangle\sin 2\theta_{\mathrm{v}} + (\mu/2)\sin 2\theta_{\mathrm{m}}\right)^2}} \ , \tag{4.25}$$

$$\sin 2\theta_\omega = \frac{\langle\omega\rangle \sin 2\theta_{\rm v} + (\mu/2)\sin 2\theta_{\rm m}}{\sqrt{\left(\langle\omega\rangle \cos 2\theta_{\rm v} - \sqrt{2}G_{\rm F}n_{\rm e} + (\mu/2)\cos 2\theta_{\rm m}\right)^2 + \left(\langle\omega\rangle \sin 2\theta_{\rm v} + (\mu/2)\sin 2\theta_{\rm m}\right)^2}} \,. \tag{4.26}$$

If $\mathbf{s}_\omega$ goes through resonance non-adiabatically at densities above the resonance density for $\mathbf{S}^{(0)}$, then subsequently $\mathbf{s}_\omega$ will no longer stay anti-aligned with $\mathbf{H}_\omega$. This change in alignment corresponds to neutrinos jumping between mass states. Confirmation of this simple picture is borne out by our numerical simulations as can be seen in Figures 4.11 and 4.12, where the Bump profile exhibits a population of low energy mass state 2 (ν_2) neutrinos. In the Bump density profile, Figure 4.11, the helium burning shell produces multiple MSW-like resonances for low energy neutrinos. These multiple resonances,illustrated in Figure 4.14, are non-adiabatic, engendering further loss of alignment. This leads to a population of low energy neutrinos occupying mass state 2, which do not recover their alignment with $\mathbf{H}_\omega$.

By way of contrast, in Figure 4.12 there is no population of low energy neutrinos in mass state 2 because the absence of the helium burning shell in the No Bump profile makes the evolution of these neutrinos adiabatic, hence they remain aligned with $\mathbf{H}_\omega$. In both cases, NIFS's $\mathbf{s}_\omega$ over a wide range of ω experience significant evolution at densities higher than the resonance density of $\mathbf{S}^{(0)}$.

If $\mathbf{S}^{(0)}$ goes through resonance adiabatically, the above description of NFIS evolution can be extended to lower densities. Note that $\cos 2\theta_{\rm m}$ changes from ≈ -1 at high density to 0 at resonance and to $\approx \cos 2\theta_{\rm v}$ at low density, consistent with a simple MSW picture. The term$\sqrt{2}G_{\rm F}n_{\rm e} - (\mu/2)\cos 2\theta_{\rm m}$ becomes 0 at some radius and all $\mathbf{s}_\omega$ go through resonance before this radius.

However, if $\mathbf{S}^{(0)}$ goes through resonance non-adiabatically, the situation becomes more complicated. For illustration consider the regime of low $n_{\rm e}$, lower than the $\mathbf{S}^{(0)}$ resonance density. The non-adiabatic evolution of $\mathbf{S}^{(0)}$ means that it no longer stays anti-aligned with $\mathbf{H}_{\rm MSW} \approx \langle\omega\rangle\mathbf{H}_{\rm v}$ in this regime. Instead, one has

$$\mathbf{S}^{(0)} \cdot \hat{\mathbf{H}}_{\rm v} = \frac{1}{2}\cos\alpha = P_{\rm hop} - \frac{1}{2} \,, \tag{4.27}$$

where α is the angle between $\mathbf{S}^{(0)}$ and the external field
$\mathbf{H}_{\rm v}$, and $P_{\rm hop}$ is the probability for $\mathbf{S}^{(0)}$ to hop from being anti-aligned before

resonance to being aligned with $\mathbf{H}_{\mathrm{MSW}}$ after resonance. One can take

$$\mathbf{S}^{(0)} \approx \left(P_{\mathrm{hop}} - \frac{1}{2}\right)\hat{\mathbf{H}}_{\mathrm{v}} + \mathbf{S}_{\perp}^{(0)} \ , \tag{4.28}$$

where $\mathbf{S}_{\perp}^{(0)}$ is the component perpendicular to $\mathbf{H}_{\mathrm{v}}$ with a magnitude

$$\mathbf{S}_{\perp}^{(0)} \approx \sqrt{(1/2)^2 - [P_{\mathrm{hop}} - (1/2)]^2} \ . \tag{4.29}$$

Note that $\mathbf{S}_{\perp}^{(0)}$ precesses around $\mathbf{H}_{\mathrm{v}}$ with an angular velocity $-\langle\omega\rangle\mathbf{H}_{\mathrm{v}}$.

In a frame co-precessing with $\mathbf{S}^{(0)}$, the evolution of $\mathbf{s}_{\omega}$ is governed by

$$\begin{aligned}
\frac{d}{dr}\mathbf{s}_{\omega} &\approx \mathbf{s}_{\omega} \times \left[\left(\omega - \langle\omega\rangle\right)\mathbf{H}_{\mathrm{v}} - \mu\left(r\right)\mathbf{S}^{(0)}\right] && (4.30)\\
&\approx \mathbf{s}_{\omega} \times \left\{\left[\omega - \langle\omega\rangle - \mu\left(r\right)\left(P_{\mathrm{hop}} - \frac{1}{2}\right)\right]\mathbf{H}_{\mathrm{v}} - \mu\left(r\right)\mathbf{S}_{\perp}^{(0)}\right\} && (4.31)\\
&\equiv \mathbf{s}_{\omega} \times \mathbf{H}_{\omega}^{\mathrm{co-pre}} \ . && (4.32)
\end{aligned}$$

The evolution of $\mathbf{s}_{\omega}$ is expected to be adiabatic and, as a result, the angle between $\mathbf{s}_{\omega}$ and $\mathbf{H}_{\omega}^{\mathrm{co-pre}}$ stays fixed. This angle depends on the relative directions of $\mathbf{s}_{\omega}$ and $\mathbf{H}_{\omega}^{\mathrm{co-pre}}$ right after the resonance of $\mathbf{S}^{(0)}$. The latter direction depends on the exact direction of $\mathbf{S}_{\perp}^{(0)}$ coming out of the resonance. At large radii, $\mathbf{H}_{\omega}^{\mathrm{co-pre}}$ simply becomes $\left(\omega - \langle\omega\rangle\right)\mathbf{H}_{\mathrm{v}}$. Those $\mathbf{s}_{\omega}$ with $\omega < \langle\omega\rangle$ that are approximately aligned with $\mathbf{H}_{\omega}^{\mathrm{co-pre}}$ right after the resonance of $\mathbf{S}^{(0)}$ are nearly fully converted into ν_{x}.

Neutrinos participating in the Neutrino Enhanced MSW effect have NIFS's which are closely aligned with the collective field $\mathbf{S}$, so their flavor evolution will be a close match to that of $\mathbf{S}^{(0)}$ [33]. Specifically, they will co-precess with the effective field, even when the flavor evolution of $\mathbf{S}^{(0)}$ and $\mathbf{S}$ are non-adiabatic. Examples of this co-precession can be viewed in movies which are on our website [87].

In this co-precession picture the probability to remain in the heavy mass eigenstate, P_{H}, should depend on the three quantities relevant to the MSW evolution of $\mathbf{S}^{(0)}$: vacuum mixing angle θ_{v}; collective oscillation frequency $\langle\omega\rangle$; and the matter potential scale height R_{H} at the location where $\mathbf{S}^{(0)}$ is at resonance, $\langle\omega_H\rangle\cos 2\theta_{\mathrm{v}} = 2\sqrt{2}G_{\mathrm{F}}n_{\mathrm{e}}\left(r\right)$. The first and second quantities are identical for both of these simulations. Only R_{H} changes when the burning shell feature is removed, with $R_{\mathrm{H}}^{\mathrm{Bump}} = 25.3\,\mathrm{km}$ and $R_{\mathrm{H}}^{\mathrm{No\ Bump}} = 28.5\,\mathrm{km}$.

Following the evolution of $\mathbf{S}^{(0)}$ through the envelope of matter around the proto-neutron star, the probability of a neutrino with $\omega = \langle\omega\rangle$ to hop out of the heavy mass eigenstate will be given by the double exponential Landau-Zener hopping probability, $P_{\text{hop}} = (1 - P_{\text{H}})$, with:

$$P_{\text{hop}} = \frac{\exp\left(2\pi R_{\text{H}} \langle\omega\rangle \cos^2\theta_{\text{v}}\right) - 1}{\exp\left(2\pi R_{\text{H}} \langle\omega\rangle\right) - 1}. \tag{4.33}$$

Given that the critical scale height of the matter profile is slightly smaller for the Bump profile, the above equation implies that there should be a larger probability to hop out of mass state 3 in the presence of the helium burning shell. This is why the total number of neutrinos remaining in mass state 3 naively is expected to increase for the No Bump simulation. Equation 4.33 yields a prediction that for the Bump density profile $P_{\text{H}}^{\text{Predicted}} = 0.68$, and for the No Bump density profile $P_{\text{H}}^{\text{Predicted}} = 0.71$.

Using the final emission spectra from Figures 4.11 and 4.12 to calculate P_{H} for both simulations, as one would in analyzing an actual supernova neutrino signal, produces somewhat different results. For the No Bump calculation, $P_{\text{H}}^{\text{Observed}} = 0.76$. This indicates a slightly more adiabatic than I had calculated above, and would lead an observer to deduce a larger matter scale height in the collapsing core of the supernova than was actually present. More strikingly, the Bump profile exhibits $P_{\text{H}}^{\text{Observed}} = 0.85$, implying fully 17% more neutrinos remain in mass state 3 than predicted. This would lead an observer interested in the envelope to grossly miss-calculate the electron density scale height, arriving at a number nearly twice the actual value. I will endeavor to understand why it is that our model of neutrino flavor transformation seems to have led us astray when attempting to work backward from our observed signal to the matter density profile of the collapsing star.

4.3.3 Analysis

Though the simple neutrino transformation model presented above is successful in many respects, I do not attempt to provide an exhaustive proof of the model, only to point out that it offers a straightforward explanation of the puzzling aspects of our result. Furthermore, our numerical calculations show that one must be careful in applying the theory of the Neutrino Enhanced MSW effect to infer information about the envelope of the proto-neutron star.

First, even in early (e.g. Ref. [56]) treatments of neutrino flavor evolution it was evident that flavor diagonal neutrino-neutrino forward scattering potential, $B\left(r\right)$, would alter the position of the MSW resonance position for a given neutrino energy E_ν and mass splitting Δm^2 because the resonance condition is

$$\frac{\Delta m^2}{2E}\cos 2\theta_{\mathrm{v}} = A\left(r\right) + B\left(r\right) \ , \tag{4.34}$$

where $A\left(r\right) = \sqrt{2}G_{\mathrm{F}}n_{\mathrm{e}}\left(r\right)$ is the matter potential at radius r. Neutrino propagation through the MSW resonance at the shifted position in general will result in an altered survival probability because the scale height of the combined potential will be different. However, this simplistic analysis is completely inadequate because it is the neutrino-neutrino flavor off-diagonal potential which in part determines adiabaticity [56, 31]. This potential, in turn, is sensitive to the relative $x-y$ plane phase angles of the individual neutrino NFIS's, necessitating a self-consistent collective oscillation treatment.

Shown in Figures 4.15 and 4.16 is the evolution of the Neutrino Enhanced MSW effect collective NFIS $\mathbf{S}$ and evolution of the zeroth order approximation $\mathbf{S}^{(0)}$. Each of these are given for the Bump and No Bump profiles. These figures show the opening angle between the collective NFIS and $\mathbf{H}_{\mathrm{MSW}}$. To lowest order, the collective NFIS $\mathbf{S}$ from Equation 4.13 follows the alignment of $\mathbf{S}^{(0)}$, starting anti-aligned with $\mathbf{H}_{\mathrm{MSW}}$ and undergoing a mild change of alignment as the system passes through resonance, with the hopping probability given by $P_{\mathrm{hop}} = 1/2\left(1+\cos\alpha\right)$. However, there is a small difference between the final alignment of $\mathbf{S}^{(0)}$ and $\mathbf{S}$ for all of the calculations. The full numerical calculations reveal that mass state hopping is more adiabatic than our zeroth order approximation would lead us to believe, differing by $\approx 5-10\,\%$ from the hopping probability associated with the evolution of $\mathbf{S}^{(0)}$.

The reason that the full calculations exhibit less mass state hopping can be found in the imperfect alignment of individual $\mathbf{s}_\omega$ with $\mathbf{S}$. The Neutrino Enhanced MSW model predicts that individual $\mathbf{s}_\omega$ tend to stay aligned with $\mathbf{S}$ as the collec-

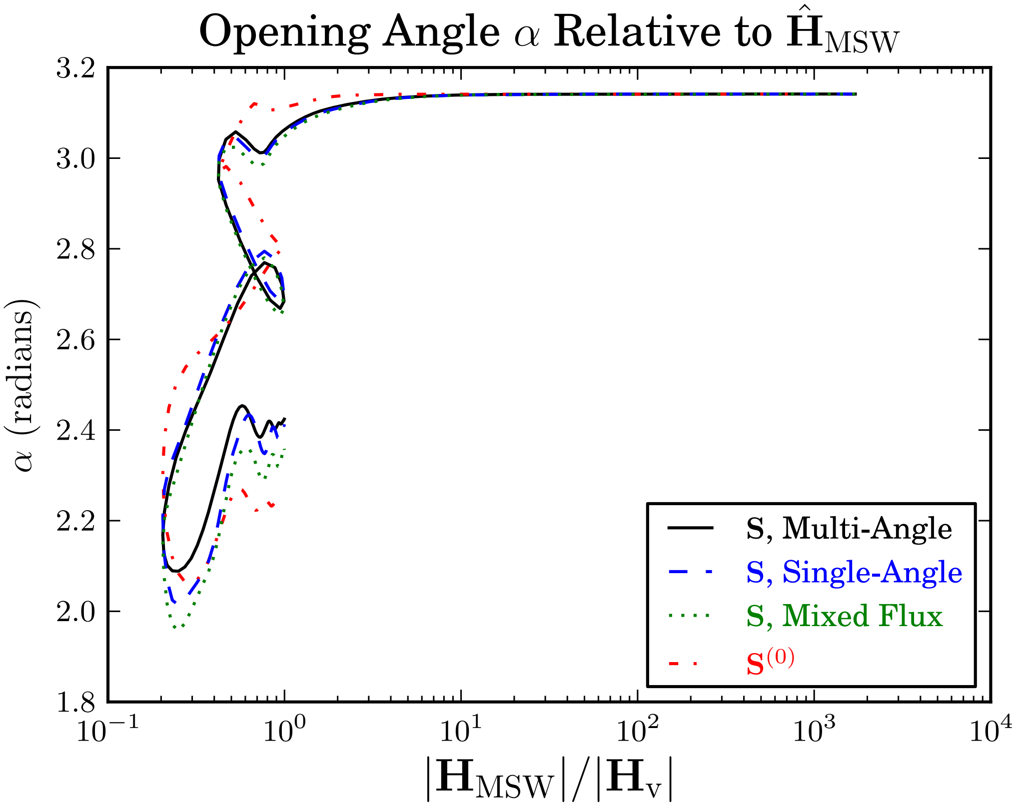

Figure 4.15: Bump: The opening angle α between the collective NFIS and $\mathbf{H}_{\rm MSW}$ for the Bump profile, plotted as a function of $|\mathbf{H}_{\rm MSW}| / |\mathbf{H}_{\rm v}|$ as the system moves through resonance. The idealized NFIS (dotted-dashed line) shows the evolution of $\mathbf{S}^{(0)}$ in the absence of any neutrino self-coupling. The solid line and dashed line show the evolution of $\mathbf{S}$ as calculated in multi-angle and single-angle simulations respectively, including the neutrino self-coupling potentials. The dotted line shows the evolution of $\mathbf{S}$ as calculated for a neutronization burst with $L_\nu \approx 0.1\, L_{\nu_{\rm e}}$ for all neutrino species other than $\nu_{\rm e}$. Note that the qualitative behavior of $\mathbf{S}$ for the mutli-angle, single-angle, and mixed flux treatments are quite similar.

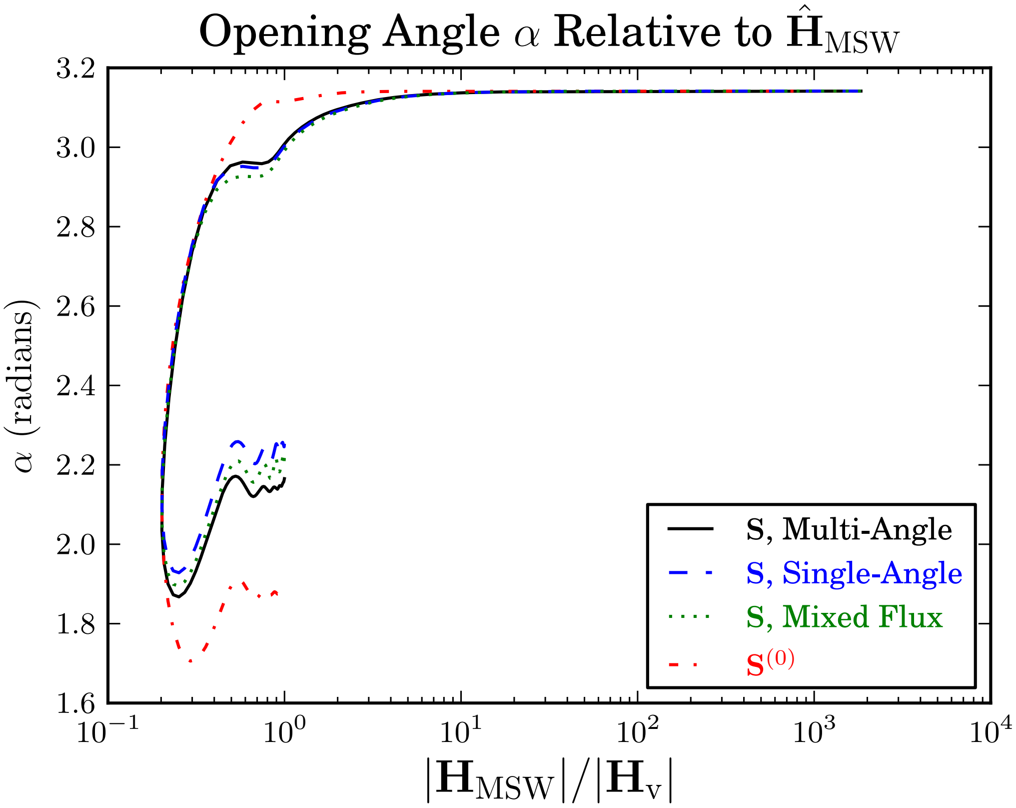

Figure 4.16: No Bump: The opening angle α between the collective NFIS and $\mathbf{H}_{\mathrm{MSW}}$ for the No Bump profile, plotted as a function of $|\mathbf{H}_{\mathrm{MSW}}|\,/\,|\mathbf{H}_{\mathrm{v}}|$ as the system moves through resonance. The idealized NFIS (dotted-dashed line) shows the evolution of $\mathbf{S}^{(0)}$ in the absence of any neutrino self-coupling. The solid line and dashed line show the evolution of $\mathbf{S}^{(0)}$ as calculated in multi-angle and single-angle simulations respectively, including the neutrino self-coupling potentials. The dotted line shows the evolution of $\mathbf{S}$ as calculated for a neutronization burst with $L_\nu \approx 0.1\,L_{\nu_{\mathrm{e}}}$ for all neutrino species other than ν_{e}. Note that the qualitative behavior of $\mathbf{S}$ for the mutli-angle, single-angle, and mixed flux treatments are quite similar.

tive mode passes through resonance and subsequently begin to orbit around $\mathbf{H}_\mathrm{v}$ as the system transitions to the regular precession mode. In Figure 4.17 I show the average opening angle between individual $\mathbf{s}_\omega$ and $\mathbf{S}$, taken to be $\cos\theta = \left(\hat{\mathbf{s}}_\omega \cdot \hat{\mathbf{S}}\right)$, for the Bump and No Bump profiles. On average individual $\mathbf{s}_\omega$ and $\mathbf{S}$ remain aligned to within a few percent throughout the resonance region in both the Bump and No Bump simulations, which shows that this is indeed the correct physical picture. However, as I have mentioned previously, the individual $\mathbf{s}_\omega$ pass through resonance at slightly higher densities than $\mathbf{S}^{(0)}$. The individual $\mathbf{s}_\omega$ are slightly misaligned and this means that when the individual neutrino states are at resonance, i.e. $\cos 2\theta_\omega = 0$, the collective mean field $\mathbf{S}$ is not yet at resonance itself, i.e. $\cos 2\theta_\mathrm{m} \neq 0$.

From Equation 4.25 we see that for an individual neutrino state at resonance the adiabaticity of the mass state hopping will not be determined entirely by the matter potential if $\cos 2\theta_\mathrm{m} \neq 0$, which is precisely the result I recover from Equation 4.34 when $A > B$ with $B \neq 0$. (By contrast, the flavor evolution through resonance for $\mathbf{S}^{(0)}$ is determined entirely by the matter potential.) Individual $\mathbf{s}_\omega$ experience some fraction of the neutrino self-coupling potential μ. This comes from the fact that our approximation $g(\omega) \approx \delta(\omega - \langle\omega\rangle)$ is a rather gross approximation. In reality, the function $g(\omega)$ has a finite width. However, one finds that this approximation produces results that match well with our calculations and individual $\mathbf{s}_\omega$ track the evolution of $\mathbf{S}^{(0)}$ more closely than one might expect given the width of our initial ν_e distribution.

A serious source of potential error in interpreting the swap signal for the neutronization neutrino burst comes from rapid fluctuations in the matter potential. I have shown the evolution of the system follows $\mathbf{S}^{(0)}$ closely. In turn, $\mathbf{S}^{(0)}$ experiences only the ordinary MSW effect in it's flavor evolution. This is illustrated clearly by the similarities in the observed mass state 3 survival probabilities and the trajectories of $\mathbf{S}$ and $\mathbf{S}^{(0)}$ in Figures 4.15 and 4.16. For the No Bump profile $P_\mathrm{H}^\mathrm{Observed} = 0.76$, and $P_\mathrm{H}^{\mathbf{S}^{(0)}} = 0.68$. For the Bump profile $P_\mathrm{H}^\mathrm{Observed} = 0.85$, and $P_\mathrm{H}^{\mathbf{S}^{(0)}} = 0.80$. However, as I have mentioned in the previous section, this result for the Bump profile is in stark disagreement with the prediction of the double

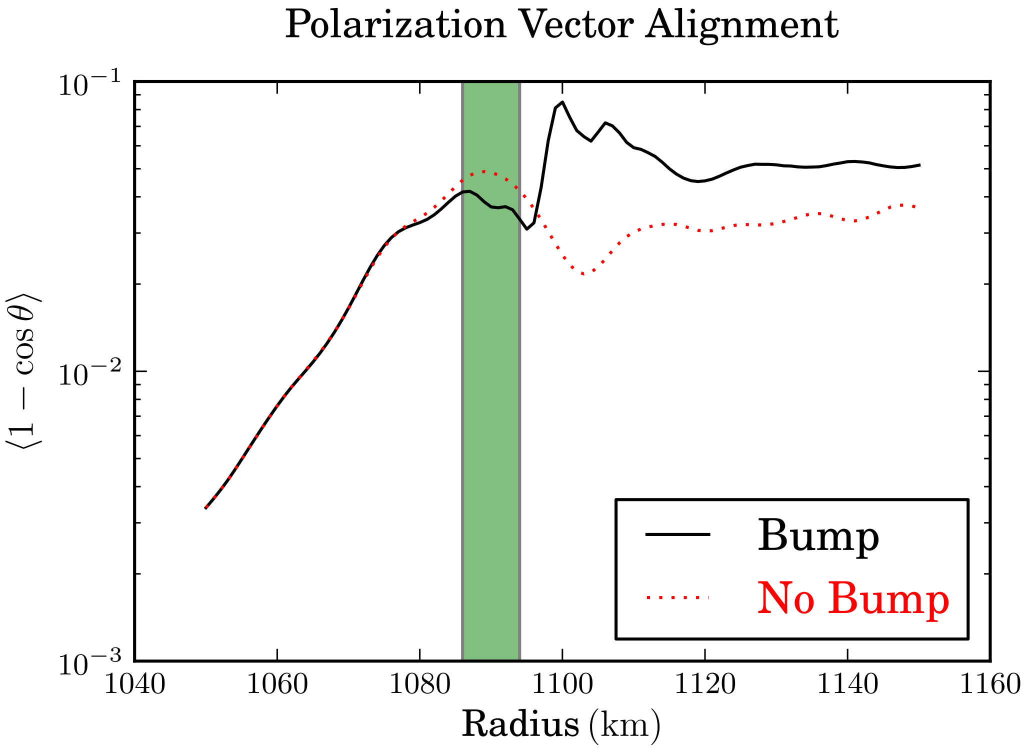

Figure 4.17: The average alignment of individual neutrino polarization vectors, $\mathbf{s}_\omega$, with the collective polarization vector, $\mathbf{S}$. The solid black line shows the “Bump” profile from Refs. [2, 3] and the dotted red line shows the modified “No Bump” profile. The shaded region indicates the physical position of the Helium burning shell density feature present in the Bump profile.

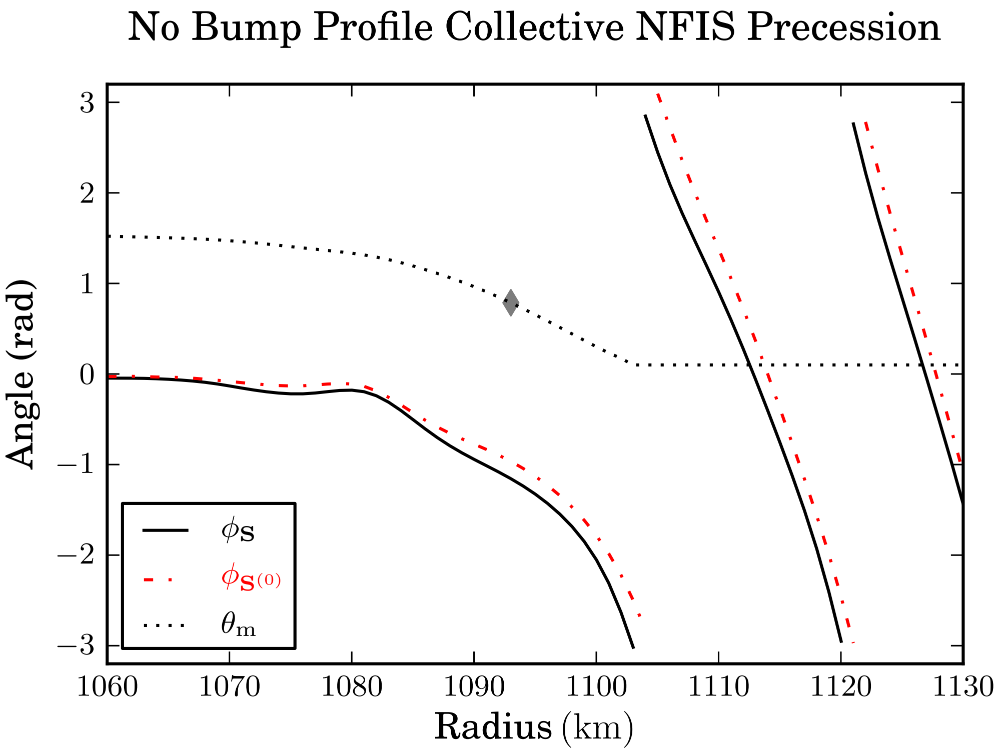

Figure 4.18: No Bump: The precession of the collective polarization vector, $\mathbf{S}$, and the zeroth order effective field $\mathbf{S}^{(0)}$, about the $\hat{\mathbf{e}}_{\mathrm{z}}^{\mathrm{f}}$ axis as neutrinos move through resonance in the No Bump profile. The solid line shows the azimuthal angle, $\phi_{\mathbf{S}}$, for the collective polarization vector $\mathbf{S}$. The dashed-dotted line shows the azimuthal angle, $\phi_{\mathbf{S}^{(0)}}$, for the zeroth order effective field $\mathbf{S}^{(0)}$. The dotted line shows the value of θ_{m} for $\mathbf{S}$ and $\mathbf{S}^{(0)}$ for reference, with a diamond symbol located at $\theta_{\mathrm{m}} = \pi/4$ where the system is at resonance.

exponential Landau-Zener hopping probability of Equation 4.33.

As has been know for some time, turbulent matter density fluctuations can produce flavor “depolarization” for MSW neutrino flavor transformation [88, 89, 90, 91, 36, 53, 54, 92, 55]. Broadly, these turbulent fluctuations can produce mass state hopping that does not agree with what one would deduce from Equation 4.33 using the gross scale height of the matter potential.

By considering the derivative of Eqn. 4.15 it can be seen that there is a restoring force that causes $\mathbf{S}^{(0)}$ to orbit $\mathbf{H}_{\mathrm{MSW}}$ as the system evolves. Another term in the derivative of Eqn. 4.15 drives precession of $\mathbf{S}^{(0)}$ about the $\hat{\mathbf{e}}_{\mathrm{z}}^{\mathrm{f}}$ axis any

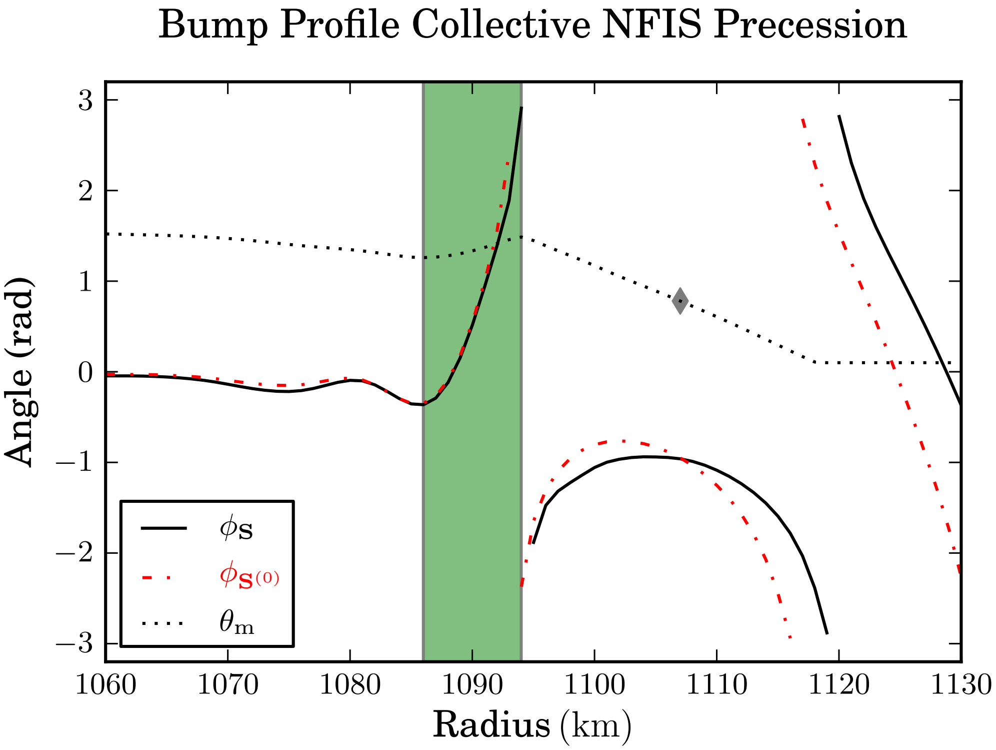

Figure 4.19: Bump: The precession of the collective polarization vector, $\mathbf{S}$, and the zeroth order effective field $\mathbf{S}^{(0)}$, about the $\hat{\mathbf{e}}_{\rm z}^{\rm f}$ axis as neutrinos move through resonance in the Bump profile. The solid line shows the azimuthal angle, $\phi_{\mathbf{S}}$, for the collective polarization vector $\mathbf{S}$. The dashed-dotted line shows the azimuthal angle, $\phi_{\mathbf{S}^{(0)}}$, for the zeroth order effective field $\mathbf{S}^{(0)}$. The dotted line shows the value of $\theta_{\rm m}$ for $\mathbf{S}$ and $\mathbf{S}^{(0)}$ for reference, with a diamond symbol located at $\theta_{\rm m} = \pi/4$ where the system is at resonance. The shaded region indicates the physical position of the Helium burning shell density feature present in the Bump profile.

time the matter potential is changing non-adiabatically.

In the traditional MSW framework, this precession is dependent on the energy of each neutrino, as the neutrino energy sets the relative size of the terms in Eqn. 4.15's derivative. As a result, if the matter density profile is turbulent, the alignments of individual neutrino NFIS's can be scattered throughout the flavor space, hence the term "depolarization".

The matter driven precession figures into the hopping probability given by Eqn. 4.33 because the double exponential hopping probability is derived from the Landau-Zener two level hopping problem using the boundary condition that the precession of $\mathbf{S}^{(0)}$ originating from this term can be taken to be zero before the system approaches resonance [93, 94]. If there is significant matter driven precession for $\mathbf{S}$ and $\mathbf{S}^{(0)}$ prior to resonance, Eqn. 4.33 will not be the appropriate analytic solution for the Landau-Zener hopping probability.

These issues can be explored by examining the projection of the collective field $\mathbf{S}$ (or $\mathbf{S}^{(0)}$) in the $\hat{\mathbf{e}}^{\mathrm{f}}_{\mathrm{x}} - \hat{\mathbf{e}}^{\mathrm{f}}_{\mathrm{y}}$ plane. Define the angle made by this projection and $\hat{\mathbf{e}}^{\mathrm{f}}_{\mathrm{x}}$ to be ϕ. Figure 4.18 shows the value of ϕ in the No Bump profile for $\mathbf{S}$ and $\mathbf{S}^{(0)}$ through the resonance region. Prior to resonance, when $\theta_{\mathrm{m}} \backsimeq \pi/2$, there is no appreciable precession of either $\mathbf{S}$ or $\mathbf{S}^{(0)}$. This is not particularly surprising, as the observed hopping probability of $\mathbf{S}^{(0)}$ matches exactly with Eqn. 4.33, with $\mathbf{S}$ exhibiting slightly less hopping as I have discussed above.

Figure 4.19, where I show the evolution of ϕ for $\mathbf{S}$ and $\mathbf{S}^{(0)}$ in the Bump profile, exhibits very different phenomenology. The system starts out identically to the configuration of the neutrinos in the No Bump profile, with no matter driven precession before the bump is reached. However, the sudden increase in the local matter density at $r \sim 1086\,\mathrm{km}$ brought on by the helium burning shell drives rapid precession of $\mathbf{S}$ and $\mathbf{S}^{(0)}$ in a counter clock-wise direction. At the same time, the value of θ_{m} is brought back up to the pre-resonance value of $\theta_{\mathrm{m}} \backsimeq \pi/2$. This resets the clock, so to speak, on $\mathbf{H}_{\mathrm{MSW}}$ and the boundary conditions for $\mathbf{S}$ and $\mathbf{S}^{(0)}$. The collective NFIS is clearly precessing rapidly at the boundary of the MSW resonance region, meaning that our use of the double exponential hopping formula is not appropriate.

This phenomenon is a simplistic example of the turbulence driven flavor depolarization discussed in Ref. [90, 36, 92, 55], where we are following the evolution of a single NFIS, $\mathbf{S}^{(0)}$, as it is scattered to a random position in flavor space. What is surprising about this calculation is that I have observed that the collective Neutrino Enhanced MSW effect persists and maintains coherence in multi-angle calculations, in spite of rough handling by the matter potential. The collective NFIS, $\mathbf{S}$ (and consequently the individual neutrino $\mathbf{s}_\omega$'s), tracks the evolution of $\mathbf{S}^{(0)}$ and achieves a final alignment in flavor space that is not relatable to the simplistic prediction of Eqn. 4.33. Our calculations suggest that the Neutrino Enhanced MSW effect is susceptible to the same turbulence driven precession as the ordinary MSW effect.

This is unfortunate from the perspective of attempts to use the swap signal to probe the matter density profile. In the particular case of the neutronization neutrino burst, the resultant swap energy may or may not be relatable to the matter density profile, depending on the "smoothness" of the actual matter density profile of the collapsing star. In the case of the Bump profile, our observed survival probability of $P_{\mathrm{H}}^{\mathrm{Bump}} = 0.852$ would lead an observer to infer a matter density scale height of $R_{\mathrm{H}}^{\mathrm{Bump,\ inferred}} = 45.9\,\mathrm{km}$, compared to the actual scale height of $R_{\mathrm{H}}^{\mathrm{Bump}} = 25.3\,\mathrm{km}$, an 85% error. In principle, this fluctuation driven precession might alter the survival probability P_{H} and, consequently, push the swap energy up or down depending on the particular realization of the density fluctuations [90, 36, 92, 55].

In the example I study here, the low energy neutrinos experiencing multiple MSW resonances would be almost invisible to neutrino detectors designed to collect supernova neutrinos, since these detectors might have low energy thresholds of $\sim 5-10\,\mathrm{MeV}$. However these neutrinos provide our only clue about matter density fluctuations. While I have been able to use our detailed knowledge of the neutrino flavor states as they evolved through the resonance region to correctly deduce what has transpired, an observer on the Earth would not have access to such privileged information.

4.4 Luminosity Variation Effects

The results from multi-angle simulations shown in Figures 4.20 and 4.21 demonstrate that the n_e profile with the bump gives rise to a very clear flavor transformation signature. Depending on the luminosity, a population of ν_e below 8 MeV have large probabilities to transform between neutrino mass states (have large hopping probabilities). For example, the medium range luminosity case, $L_\nu = 8.0 \times 10^{52}\,\mathrm{erg\,s^{-1}}$, exhibits a peak hopping probability for the bump-affected neutrinos of $\sim 80\%$ at $E_\nu = 4.5\,\mathrm{MeV}$, shown in Figure 4.21. In the extreme case of $L_\nu = 10^{54}\,\mathrm{erg\,s^{-1}}$, the hopping probability is $\sim 15\%$ for $E_\nu = 0.5\,\mathrm{MeV}$, although this is hard to see in Figure 4.20 (but see Figure 4.21).

4.4.1 Analysis of Flavor Evolution of the ν_e's

As discussed in Refs. [40, 78, 44, 45] the flavor evolution of the ν_e flux in this case is governed by $\delta m^2_{\mathrm{atm}}$ and θ_{13}. Although the numerical calculations I have conducted employ full 3×3 flavor mixing, in the following analysis, we focus on the 2-flavor mixing for these ν_e with $\delta m^2 = \delta m^2_{\mathrm{atm}}$ and $\theta_{\mathrm{v}} = \theta_{13}$. Further, I adopt the single-angle approximation, as this has been shown to be surprisingly effective in providing qualitative understanding of the results from multiangle simulations.

Using the notation introduced in Ref. [32], we can represent a ν_e of energy E by a neutrino flavor isospin (NFIS) $\mathbf{s}_\omega$ with $\omega = \delta m^2/2E$. The evolution of $\mathbf{s}_\omega$ is governed by

$$\frac{d}{dr}\mathbf{s}_\omega = \mathbf{s}_\omega \times \left[\omega \mathbf{H}_{\mathrm{v}} + \mathbf{H}_e - \mu(r)\int_0^\infty \mathbf{s}_{\omega'} f_\nu(E_{\omega'})dE_{\omega'}\right], \tag{4.35}$$

where $\mathbf{H}_{\mathrm{v}} = \cos 2\theta_{\mathrm{v}}\hat{\mathbf{e}}^{\mathrm{f}}_z - \sin 2\theta_{\mathrm{v}}\hat{\mathbf{e}}^{\mathrm{f}}_x$, $\mathbf{H}_e = -\sqrt{2}G_F n_e(r)\hat{\mathbf{e}}^{\mathrm{f}}_z$, $\mu(r) = 2\sqrt{2}G_F n_\nu(r)$, and $E_{\omega'} = \delta m^2/2\omega'$. Here $\hat{\mathbf{e}}^{\mathrm{f}}_x$ and $\hat{\mathbf{e}}^{\mathrm{f}}_z$ are the unit vectors in the x and z directions, respectively, of the neutrino flavor space. For convenience, I define

$$g(\omega) \equiv \frac{\delta m^2}{2\omega^2} f_\nu(E_\omega) \tag{4.36}$$

and

$$\mathbf{S} \equiv \int_0^\infty \mathbf{s}_\omega f_\nu(E_\omega)dE_\omega = \int_0^\infty \mathbf{s}_\omega g(\omega)d\omega. \tag{4.37}$$

It follows that

$$\frac{d}{dr}\mathbf{S} = \int_0^\infty \omega g(\omega)\mathbf{s}_\omega d\omega \times \mathbf{H}_\mathrm{v} + \mathbf{S} \times \mathbf{H}_e. \tag{4.38}$$

As $g(\omega)$ is concentrated in a finite range of ω, to zeroth order we approximate $g(\omega) \approx \delta(\omega - \langle\omega\rangle)$, where $\langle\omega\rangle = \int_0^\infty \omega g(\omega) d\omega$ is calculated from the actual $g(\omega)$ in Eq. (5). Then the zeroth-order mean field $\mathbf{S}^{(0)}$ can be obtained from

$$\frac{d}{dr}\mathbf{S}^{(0)} = \mathbf{S}^{(0)} \times [\langle\omega\rangle\mathbf{H}_\mathrm{v} + \mathbf{H}_e] \equiv \mathbf{S}^{(0)} \times \mathbf{H}_\mathrm{MSW}. \tag{4.39}$$

The evolution of $\mathbf{S}^{(0)}$ is the same as that of a ν_e with $E_\mathrm{MSW} = \delta m^2/2\langle\omega\rangle = 8.53$ MeV undergoing the usual MSW effect. With this, we can approximately solve the evolution of $\mathbf{s}_\omega$ by employing

$$\frac{d}{dr}\mathbf{s}_\omega \approx \mathbf{s}_\omega \times \left[\omega\mathbf{H}_\mathrm{v} + \mathbf{H}_e - \mu(r)\mathbf{S}^{(0)}\right]. \tag{4.40}$$

As the heavy mass eigenstate essentially coincides with ν_e at high densities, but the light mass eigenstate is predominantly ν_e at low densities, the survival probability of an initial ν_e is approximately $1 - P_\mathrm{H}$, where P_H is the probability for remaining in the heavy mass eigenstate.

4.4.2 Dependence on L_ν

We can go further by using the zeroth-order mean field $\mathbf{S}^{(0)}$ to understand how the flavor evolution of the low-energy ν_e depends on L_ν. As discussed below, Equations 4.39 and 4.40 imply that neutrinos with $\omega \gg \langle\omega\rangle$ will experience an MSW resonance before the resonance of $\mathbf{S}^{(0)}$. These higher frequency neutrinos may pass through multiple resonances created by the matter potential bump.

Based on the MSW effect, $\mathbf{S}^{(0)}$ corresponding to $E_\mathrm{MSW} = 8.53$ MeV goes through the resonance after the low-energy ν_e. Assuming adiabatic evolution of $\mathbf{S}^{(0)}$ before the resonance, we can take

$$\mathbf{S}^{(0)} \approx -\frac{\mathbf{H}_\mathrm{MSW}}{2|\mathbf{H}_\mathrm{MSW}|} \approx -\frac{1}{2}(\cos 2\theta_m \hat{\mathbf{e}}_z^f - \sin 2\theta_m \hat{\mathbf{e}}_x^f), \tag{4.41}$$

where

$$\cos 2\theta_m = \frac{\langle\omega\rangle\cos 2\theta_{\rm v} - \sqrt{2}G_F n_e}{\sqrt{(\langle\omega\rangle\cos 2\theta_{\rm v} - \sqrt{2}G_F n_e)^2 + (\langle\omega\rangle \sin 2\theta_{\rm v})^2}}, \tag{4.42}$$

$$\sin 2\theta_m = \frac{\langle\omega\rangle\sin 2\theta_{\rm v}}{\sqrt{(\langle\omega\rangle\cos 2\theta_{\rm v} - \sqrt{2}G_F n_e)^2 + (\langle\omega\rangle \sin 2\theta_{\rm v})^2}}. \tag{4.43}$$

The evolution of $\mathbf{s}_\omega$ before the resonance of $\mathbf{S}^{(0)}$ is then governed by

$$\frac{d}{dr}\mathbf{s}_\omega \approx \mathbf{s}_\omega \times \left[(\omega\cos 2\theta_{\rm v} - \sqrt{2}G_F n_e + \frac{\mu}{2}\cos 2\theta_m)\hat{\mathbf{e}}_z^f - (\omega \sin 2\theta_{\rm v} + \frac{\mu}{2}\sin 2\theta_m)\hat{\mathbf{e}}_x^f\right] \tag{4.44}$$

$$\equiv \mathbf{s}_\omega \times \mathbf{H}_\omega\ . \tag{4.45}$$

The above equation shows that $\mathbf{s}_\omega$ goes through the resonance when

$$\omega\cos 2\theta_{\rm v} = \sqrt{2}G_F n_e - \frac{\mu}{2}\cos 2\theta_m \equiv |{\rm H}_e| + B. \tag{4.46}$$

Note that $\cos 2\theta_m < 0$ before the resonance of $\mathbf{S}^{(0)}$ [see Eq. (11)] and therefore $B > 0$. Consequently, the energy of those ν_e ($E_\omega = \delta m^2/2\omega$) that go through the resonance at the bump in the n_e profile decreases as L_ν, and hence B, increases. This trend can be seen in every frame in Figures 4.20 and 4.21. As the neutrino luminosity is increased, the peak energy of the population of low energy neutrinos that hop out of the heavy neutrino mass eigenstate as a result of the bump decreases.

We can also qualitatively understand why increasing L_ν produces a decreasing survival probability of the bump-affected ν_e. The Landau-Zener probability for hopping from the heavy to the light mass eigenstate after the resonance is

$$P_{\rm hop} = \exp\left[-\frac{\pi}{4}\frac{\delta m^2 \sin^2 2\theta_{\rm v}}{E\cos 2\theta_{\rm v}}\mathcal{H}_{\rm res}\right], \tag{4.47}$$

where

$$\mathcal{H}_{\rm res} \equiv \left|\frac{d\ln(|{\rm H}_e| + B)}{dr}\right|^{-1}_{\rm res} \tag{4.48}$$

is the scale height of the total flavor-evolution potential at the resonance position. Crudely we have $1 - P_{\rm H} \sim P_{\rm hop}$. As increasing L_ν shifts the resonance energy window to lower E_ν at the bump in the n_e profile, $P_{\rm hop}$ decreases because flavor evolution through the resonance tends to be more adiabatic for lower-energy neutrinos [see Eq. (16)]. In addition, as B decreases much more slowly than $|\mathrm{H}_e|$ with radius, $\mathcal{H}_{\mathrm{res}}$ becomes larger when the contribution from B increases with L_ν. This also reduces P_{hop} [see Eq. (16)].

Furthermore, equations 4.39 and 4.40 also imply that a sufficiently large neutrino-neutrino scattering potential will cause neutrinos with oscillation frequencies roughly equal to or less than $\langle\omega\rangle$ to follow the evolution of $\mathbf{S}^{(0)}$ as this vector moves through resonance. To illustrate this, I choose to define the angle α as the angle between $\mathbf{H}_{\mathrm{MSW}}$ and either $\mathbf{S}^{(0)}$ or $\mathbf{S}$. The heavy mass eigenstate survival probability P_{H} of the collective ensemble of neutrinos that follow the evolution of $\mathbf{S}^{(0)}$ is related to α by

$$P_{\mathrm{H}} = 1 - \frac{1}{2}\left(1 + \cos\alpha\right). \tag{4.49}$$

Figure 4.22 shows the evolution of α for the simulations with relatively high luminosities. From the figure it can be seen that the evolution of $\mathbf{S}$ for these luminosities is qualitatively similar to that of $\mathbf{S}^{(0)}$.

Interestingly, the final alignment angle, α, for the collective neutrino isospin vectors is slightly larger than it is for $\mathbf{S}^{(0)}$. This means that the collective NFIS's are more closely aligned with $-\hat{\mathbf{H}}_{\mathrm{v}}$ than $\mathbf{S}^{(0)}$ is. The highest luminosity simulation, with $L_\nu = 10^{54}\,\mathrm{erg\,s^{-1}}$, has the collective NFIS that is most closely aligned with $\mathbf{S}^{(0)}$, and the reason for this can be found in Eq. 4.40. In the limit of $\mu(r) \gg |\mathbf{H}_{\mathrm{e}}| \gg \omega$ the individual $\mathbf{s}_\omega$ will orbit exclusively around $\mathbf{S}^{(0)}$ and follow it through resonance. However, it can be seen from Eqs. 4.42 and 4.45 that only neutrinos with $\omega = \langle\omega\rangle$ go through resonance at the exact position where $\cos 2\theta_{\mathrm{m}} = 0$. Neutrinos following the evolution of $\mathbf{S}^{(0)}$ will still experience some fraction of the neutrino self-coupling potential, although at resonance $|\mathbf{H}_{\mathrm{e}}| \gg B$ for neutrinos that track $\mathbf{S}^{(0)}$. This results in a small increase in $\mathcal{H}_{\mathrm{res}}$, which slightly lowers the overall hopping probability and slightly increases α.

When the neutrino luminosity is moderately lower, the same basic phenomenology is observed. Figure 4.23 shows the evolution of α for the simulations with moderate luminosities, $0.6 - 1.0 \times 10^{53}\,\mathrm{erg\,s^{-1}}$. The collective NFIS $\mathbf{S}$ for these simulations still tracks roughly the evolution of $\mathbf{S}^{(0)}$, although deviations become more pronounced as the neutrino luminosity decreases. Counter-intuitively, the final alignment of the lower luminosity $\mathbf{S}$'s is closer to that of $\mathbf{S}^{(0)}$ than in the calculations with $L_\nu = 10^{53}\,\mathrm{erg\,s^{-1}}$. This effect originates in the contribution of the bump-affected neutrinos to the integrals in Eqs. 4.37 and 4.38. From Figure 4.20 one can see that the population of bump-affected neutrinos has grown appreciably in this luminosity range, comprising $7-10\,\%$ of all neutrinos. These bump affected neutrinos are not connected in a coherent fashion to the flavor evolution of $\mathbf{S}$, but they are predominantly aligned with the $+\hat{\mathbf{H}}_{\mathrm{v}}$ axis (they are predominantly ν_2). This means that they will tend to drag the alignment of $\mathbf{S}$ closer to the $+\hat{\mathbf{H}}_{\mathrm{v}}$ axis, which systematically moves the final value of α lower.

For luminosities below $L_\nu = 6.0\times10^{52}\,\mathrm{erg\,s^{-1}}$, the magnitude of the neutrino self-coupling potential drops below $\langle\omega\rangle = 1.4\times10^{-16}\,\mathrm{MeV}$ prior to reaching the resonance region of $\mathbf{S}^{(0)}$. This means that many neutrino states will undergo an MSW-like flavor transformation prior to reaching this region of the supernova envelope. As a result, these neutrinos, including those with $\omega = \langle\omega\rangle$, will not participate in the collective flavor oscillations I have described. In turn, this means that the approximation $g\left(\omega\right) \approx \delta\left(\omega - \langle\omega\rangle\right)$ is not justified in this case. Ultimately this approximation breaks down because the evolution of the the neutrino state with $\omega = \langle\omega\rangle$ is not coherently related to the evolution of other neutrino flavor states.

The progressive breakdown of this approximation with decreasing neutrino luminosity can be seen in Figure 4.24. The motion of the vector $\mathbf{S}$ for each calculation deviates widely from the motion of $\mathbf{S}^{(0)}$. Furthermore, the final alignment angle α for each $\mathbf{S}$ is no longer related to the actual hopping probability for neutrinos in those calculations. The hopping probability inferred from Figure 4.24 and Equation 4.49 differs dramatically from the actual hopping probability observed in the calculations shown in Figures 4.20 and 4.21 for low L_ν. The discrepancies are $\Delta P_{\mathrm{hop}} = 0.16,\ 0.35,\ 0.48$ for the calculations with $L_\nu = 4.0,\ \sqrt{10},\ 1.0\times10^{52}\,\mathrm{erg\,s^{-1}}$ respectively.

4.4.3 Spectral Swap Formation

If the luminosity is large enough, it can be seen that after the neutrinos in these calculations have passed the resonance region, the neutrino self-coupling potential becomes the dominant term in the neutrino forward scattering potential. Neutrinos which have $\omega < \mu\left(r\right)$ fall into a form of collective flavor oscillations known as the Regular Precession mode. The Regular Precession mode is typified by the collective ensemble of neutrinos rotating with a common frequency, ω_{pr} about the axis of the vacuum mass basis,

$$\frac{d}{dr}\mathbf{s}_{\omega} = \omega_{\mathrm{pr}}\left(\mathbf{s}_{\omega} \times \mathbf{H}_{\mathrm{v}}\right). \tag{4.50}$$

This collective oscillation has the feature that it conserves an effective lepton number (or "energy") of the ensemble of neutrinos. While this lepton number has a more complicated general expression, in the particular case of the neutronization neutrino burst where the initial flux of neutrinos is nearly pure ν_{e}, the conserved lepton number is simply $\propto n_{\nu}P_{\mathrm{H}}$ for neutrino mixing at the atmospheric mass scale.

In the initial stages of neutrino flavor transformation, this lepton number is not conserved. However, thereafter the Regular Precession mode fixes the total number of neutrinos in mass state 3. This gives the criterion for the precession frequency, ω_{pr}, for the system,

$$\int_{\omega_{\mathrm{pr}}}^{\infty} P_H\left(\omega\right) g\left(\omega\right) d\omega = \int_{0}^{\infty} g\left(\omega\right)\left\{P_H\left(\omega\right) - \left[P_2\left(\omega\right) + P_1\left(\omega\right)\right]\right\} d\omega, \tag{4.51}$$

where $P_1\left(\omega\right)$, $P_2\left(\omega\right)$ are the probabilities of a neutrino with oscillation frequency ω to be in the instantaneous mass eigenstate 1, or 2 respectively.

It is this precession frequency that sets the energy of the spectral swap (in this case between mass state 3 and mass state 2). As the magnitude of the self coupling drops, neutrinos with oscillation frequencies in the range $\mu\left(r\right) > \omega > \omega_{\mathrm{pr}}$ will participate in the the Regular Precession mode and will align with mass state 3, while neutrinos with $\omega < \omega_{\mathrm{pr}}$ will be aligned with mass state 2. The final results of this process can be seen in Figure 4.20. For all but the least luminous calculation a spectral swap forms, with $E_{\mathrm{swap}} = \delta m^2/2\omega_{\mathrm{pr}}$, close to $E_{\nu} \sim 15\,\mathrm{MeV}$. The precise location of E_{swap} depends on the details of flavor transformation due to the motion of $\mathbf{S}^{(0)}$ and the bump affected neutrinos. Broadly speaking, a smaller P_{H} found from Eq. 4.49 will lower the swap energy of the final neutrino energy spectra by reducing the value of the integral on the right side of Eq. 4.51. However, a larger population of bump affected neutrinos will move the swap energy to higher values (smaller ω_{pr}) by reducing $P_{\mathrm{H}}(\omega)\, g(\omega)$ for large ω.

It is important to note that the spectral swap between mass states 3 and 2 can sometimes form even when the coherent flavor evolution of neutrinos has broken down deeper in the envelope. As discussed in the previous section, for the calculations with $L_\nu < 6.0 \times 10^{52}\,\mathrm{erg\,s^{-1}}$ collective neutrino flavor transformation breaks down in the resonance region because $\mu(r) < \langle\omega\rangle$. However, from Figure 4.20 it can be seen that a mass state 3/2 swap still forms successfully for $L_\nu = 4.0 \times 10^{52}\,\mathrm{erg\,s^{-1}}$ and $L_\nu = \sqrt{10} \times 10^{52}\,\mathrm{erg\,s^{-1}}$. Swaps between mass state 3 and 2 form for these two models where the luminosity is low because the neutrino self-coupling is still large compared to ω for high energy neutrinos, specifically $\mu(r) > \omega_{\mathrm{pr}}$ after the resonance region. This allows the high energy neutrinos to briefly form a Regular Precession mode before $\mu(r)$ decreases further with radius and flavor transformation in the $\delta m^2_{\mathrm{atm}}$ mixing sector stops.

For the lowest neutrino luminosity, $L_\nu = 1.0 \times 10^{52}\,\mathrm{erg\,s^{-1}}$, there is no spectral swap observed in Figure 4.20 between mass states 3 and 2. In this case, $\mu(r) < \omega_{\mathrm{pr}}$ even before the system finishes MSW-like flavor transformation. No collective oscillation can proceed in the $\delta m^2_{\mathrm{atm}}$ mixing sector for this case.

While I have focused entirely on the $\delta m^2_{\mathrm{atm}}$ mixing sector in the sections above, it should be pointed out that the $\delta m^2_{\odot}$ mixing sector is completely indifferent to the range of luminosities that I have explored. The neutrino flavor mixing energy scale for the $\delta m^2_{\odot}$ mass state splitting is ~ 30 times smaller than that of the atmospheric mass state splitting. The model of neutrino flavor transformation outlined above is quite robust for the solar mixing sector, with $\mu(r) > \langle\omega\rangle_{\odot}$ and $\mu(r) > (\omega_{\mathrm{pr}})_{\odot}$ for all of the neutrino luminosities that I consider. The spectral swap between mass states 2 and 1 is created by the Regular Precession mode in this mixing sector. While $E_{\mathrm{swap}_{\odot}}$ varies greatly for the different calculations in Figure 4.20, this swap energy is only changed by variations in flavor transformation in the $\delta m^2_{\rm atm}$ sector. The ratio of ν_2/ν_1 neutrinos is identical for all of the calculations shown in Figure 4.20. A curious consequence of this is that the spectral swap energies move closer and closer together as the luminosity of the neutronization burst decreases, until ultimately the swap between mass state 3 and 2 disappears altogether. This behavior is evident in Figure 4.20.

4.4.4 Expected Signal

So far I have examined the behavior of neutrino flavor transformation in the O-Ne-Mg neutronization burst environment in discreet segments in time, where the neutrino luminosities and spectral energy distributions are fixed. The reality of the neutronization burst is one in which the neutrino emission from the protoneutron star is evolving constantly on time scales which are short compared to the overall length of the burst. The results shown in Figures 4.20 and 4.21 are *instantaneous* snapshots of the end results of neutrino flavor transformation during the neutonization burst, and therefore do not necessarily represent the entirety of the expected signal. The luminosities, average energies, and relative fluxes of different flavors of neutrinos emitted during the burst change over the course of the neutronization epoch. Based on this analysis, I conclude that it is possible that these changes could induce significant variation in the flavor swap structure of the neutrino emission over the length of the burst.

Further complicating the issue of what one might expect to see of the neutrino flavor states as they arrive at Earth is that any detected neutronization burst signal will be constructed by stacking together all of the neutrino events in a detector within some finite window of time. The final result is a time integrated signal where the measured flavor states of individual neutrino energy bins are weighted by their instantaneous fluxes. If the swap structure of the final neutrino flavor states varies widely during this time integration window, the clean flavor swaps show in Figures 4.20 and 4.21 may not be easily detectable in the final signal.

To investigate whether these considerations are important, I conducted a suite of multi-angle, 3-flavor, neutrino flavor transformation calculations using the neutronization burst neutrino emission from two separate studies of O-Ne-Mg core-collapse explosions [4, 5]. Starting from the initial rapid rise in ν_{e} luminosity as the bounce shock moves through the neutrinosphere surface, I solve for the neutrino flavor evolution at six discrete times spaced 5 ms apart after the start of the burst, giving an overall integration time of 30 ms. This section of time slices covers what is broadly defined as the neutronization burst. Although the total length of the neutronization burst is not identical between the two studies, I choose the point of view of an observer who must make a single, appropriate time cut in order to analyze the received signal. To construct the initial neutrino emission spectra for each 5 ms time slice, I take a time average of the luminosity and average neutrino energy for each $\nu/\bar{\nu}$ flavor in a given time slice and use those data to reconstruct overall energy spectra. The neutrino mixing parameters employed for this calculation are the same as those stated at the beginning of this paper when performing calculations for the normal neutrino mass hierarchy. I also treat flavor transformation for neutrinos in the inverted neutrino mass hierarchy, where $\Delta m^2_{\mathrm{atm}} = -2.4 \times 10^{-3}\,\mathrm{eV}^2$.

The normalized total flux of neutrinos found in the final signal is taken to be the time integrated sum of the neutrino flavor states and fluxes produced by each of our calculations. Results for these calculations presented in the vacuum mass basis can be seen in Figures 4.25 and 4.26 for the normal neutrino mass hierarchy, and Figures 4.27 and 4.28 for the inverted neutrino mass hierarchy. The neutrino flavor basis representation for these results is given in Figures 4.29 and 4.30 for the normal neutrino mass hierarchy, and Figures 4.31 and 4.32 for the inverted neutrino mass hierarchy.

For neutrinos in the normal mass hierarchy, one can clearly see in Figure 4.25 that for a neutronization burst of the type found in [4], the swap structures are noticeably disrupted by the time integration of the received neutrino signal. The remnants of the two expected flavor swaps can be seen at $\sim 15\,\mathrm{MeV}$ and $\sim 20\,\mathrm{MeV}$, but these have been smoothed out by variations over time. By contrast, Figure 4.26 shows that for a neutronization burst of the type found in [5], the flavor swap signal remains sufficiently constant throughout the duration of the burst, with a mass state ν_3/ν_2 swap at 14.5 MeV and a mass state ν_2/ν_1 swap at 19 MeV.

The difference in the results for these two models derives from differences in the luminosities and average energies of neutrino emission during the neutronization neutrino burst, which in turn arrises from uncertainties in current models of supernova explosion physics. The neutrino emission parameters given in Ref. [4] are for the lab frame while those in Ref. [5] are for a frame comoving with an infalling mass element. However, even after correcting for the difference between the reference frames, significant differences remain in the neutrino emission parameters for the two supernova models, especially in terms of the neutrino luminosity. I consider that such differences are most likely due to the different physics input used by these two models. In any case, I wish to explore how small but significant variations of neutrino emission affect the signal through collective oscillations. So I have adopted the neutrino emission parameters given in Refs. [4] and [5] as examples. The study in Ref. [4] employs a model which produces ν_{e}'s which have relatively lower average energies, making them more susceptible to luminosity and bump modification of the swap signal over time compared to ν_{e}'s produced in Ref. [5]. Furthermore, the overall fluence of electron lepton number during the neutronization burst epoch in Ref. [4] is less than Ref. [5], which provides a lower relative ν_{e} luminosity. This in turn makes the swap signal produced in the neutronization burst more variable with time for the neutronization burst in Ref. [4].

For neutrinos in the inverted mass heirarchy, Figures 4.27 and 4.28 show that the swap signal is consistent over time for both models I consider. For both studies, the expected neutrino signal has a clear mass state ν_2/ν_1 swap. The swap energies are slightly different, owing to the different average energies of ν_{e}'s in both studies. The swap signals in the inverted neutrino mass hierarchy are insensitive to the differences in neutrino emission between these studies because the inverted mass hierarchy forms only a single swap at the $\Delta m^2_{\odot}$ scale. Because the mass squared splitting for this scale is ~ 30 times smaller than the atmospheric scale, the ν_{e} luminosity for both of these studies is firmly in the "high luminosity" limit for swap formation via the mode of collective neutrino flavor transformation I have outlined here and, as a result, is not sensitive to the changes in neutrino luminosity and average energy over the course of the burst.

Chapter 4, in part, is a reprint of material has appeared in Physical Review D, 2010-2012. Cherry, J. F., Wu, M.-R., Carlson, J., Duan, H., Fuller, G. M., and Qian, Y.-Z., the American Physical Society, 2010-2012. The dissertation author was the primary investigator and author of these papers.

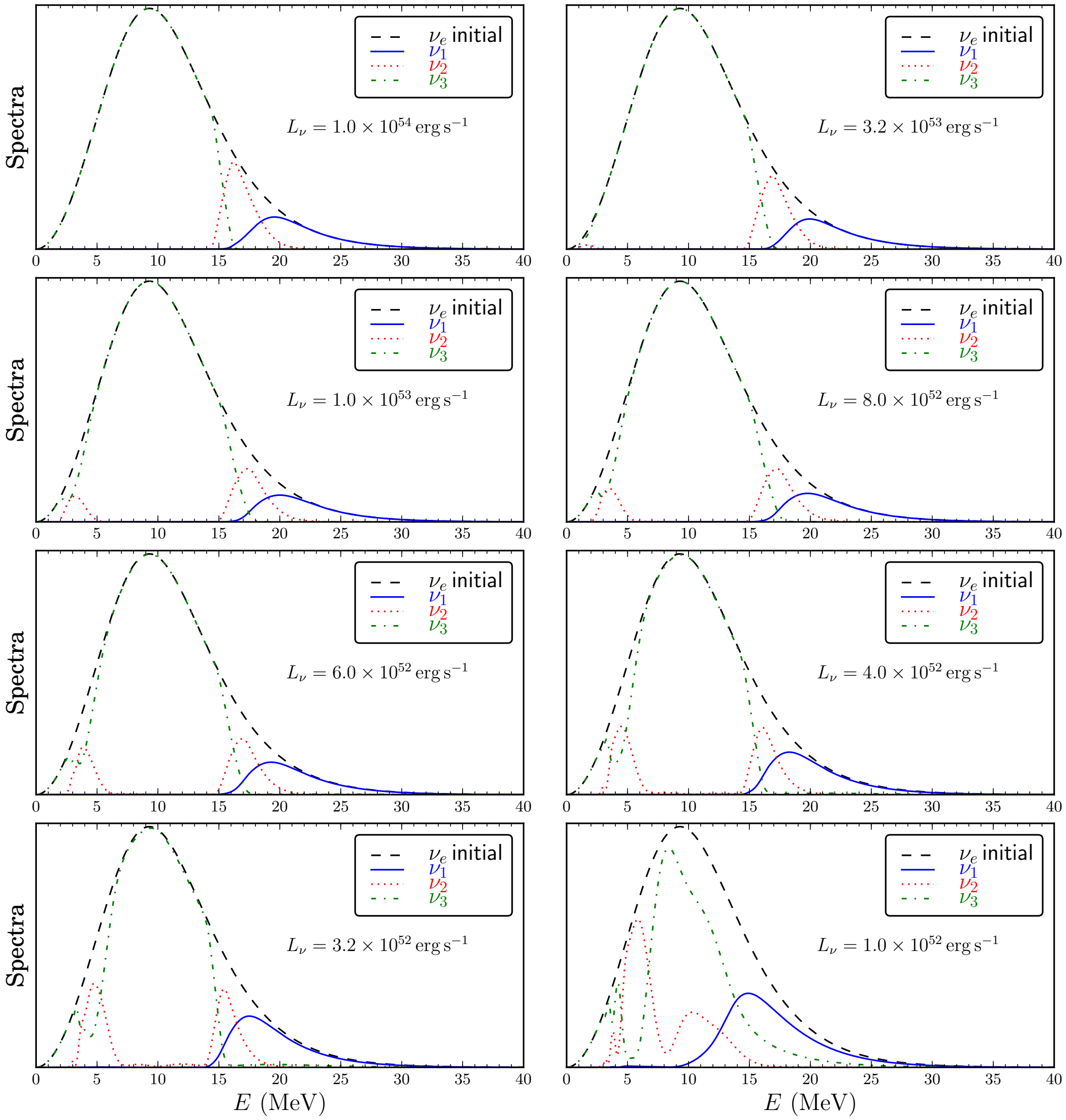

Figure 4.20: The final neutrino mass state emission energy spectra for calculations of the flavor transformation in the neutronization neutrino burst of an O-Ne-Mg core-collapse supernova. Each panel shows the results for a different possible burst luminosity, ranging from $L_\nu = 10^{54} - 10^{52}\,\mathrm{erg\,s^{-1}}$, with identical Fermi-Dirac energy distributions.

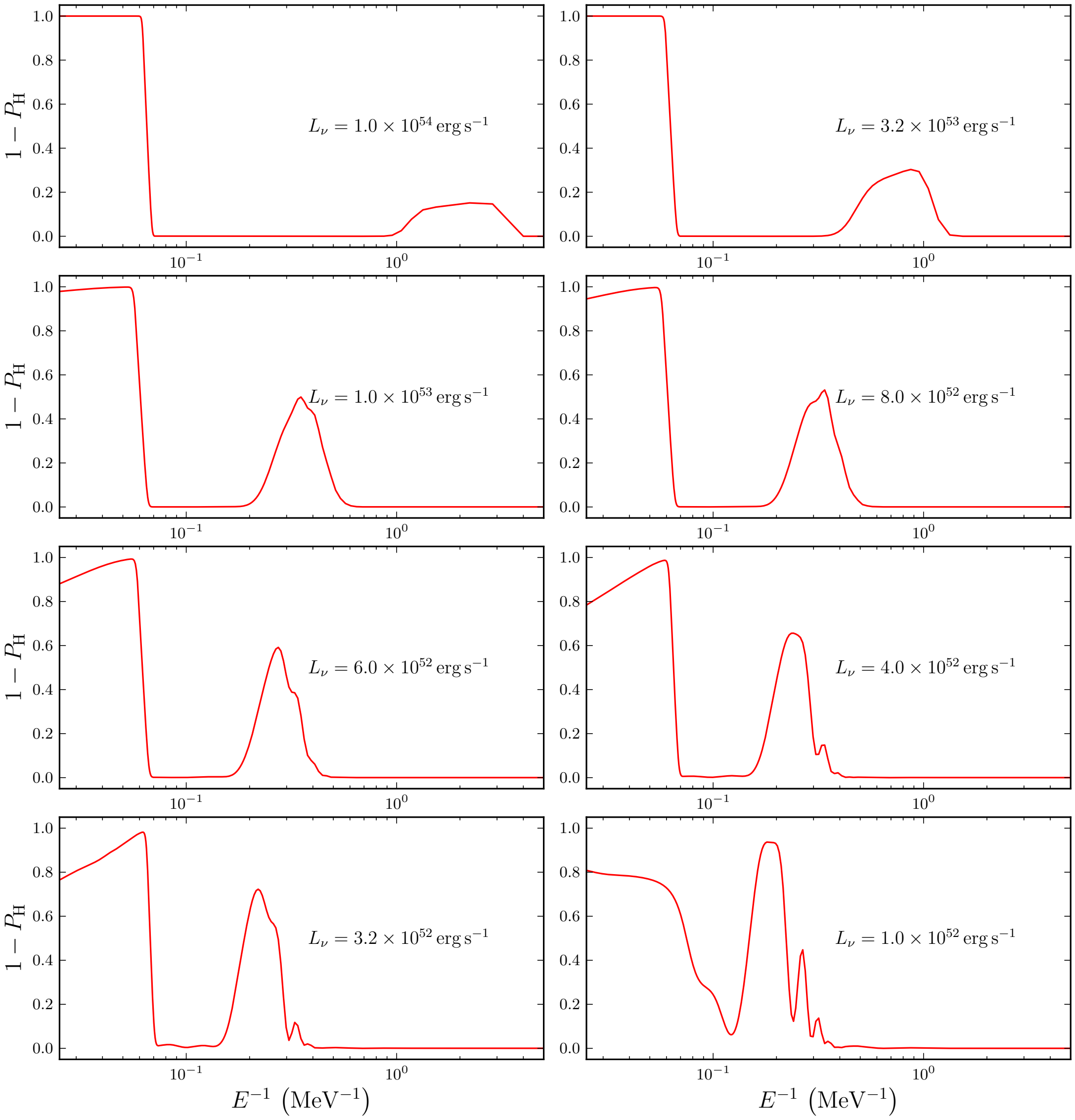

Figure 4.21: The probability for electron neutrinos in the neutronization neutrino burst of an O-Ne-Mg core-collapse supernova to hop out of the (initial) heavy mass eigenstate, $1 - P_{\rm H}$, plotted as a function of inverse neutrino energy. Each panel shows the results for a different possible burst luminosity, ranging from $L_\nu = 10^{54} - 10^{52}\,{\rm erg\,s^{-1}}$, with identical Fermi-Dirac energy distributions.

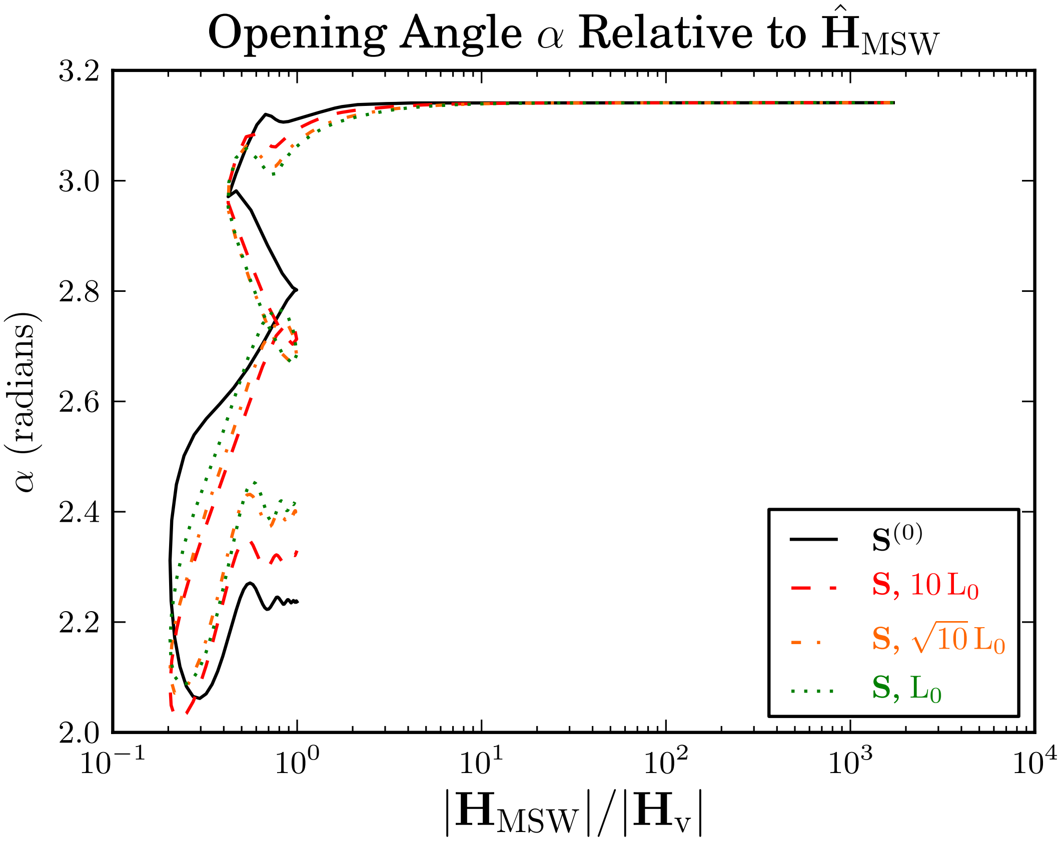

Figure 4.22: High luminosity evolution ($L_0 = 10^{53}\,\mathrm{erg\,s^{-1}}$): The opening angle α between the collective NFIS $\mathbf{S}^{(0)}$ and $\mathbf{H}_{\mathrm{MSW}}$, plotted as a function of $|\mathbf{H}_{\mathrm{MSW}}|\,/\,|\mathbf{H}_{\mathrm{v}}|$ as the system moves through resonance. The idealized NFIS (solid line) shows the evolution of $\mathbf{S}^{(0)}$ in the ideal, strong neutrino self-coupling case. The dashed line, dot-dashed line, and dotted line show the evolution of $\mathbf{S}$ as calculated for neutrino luminosities $10L_0$, $\sqrt{10}L_0$, and L_0 respectively.

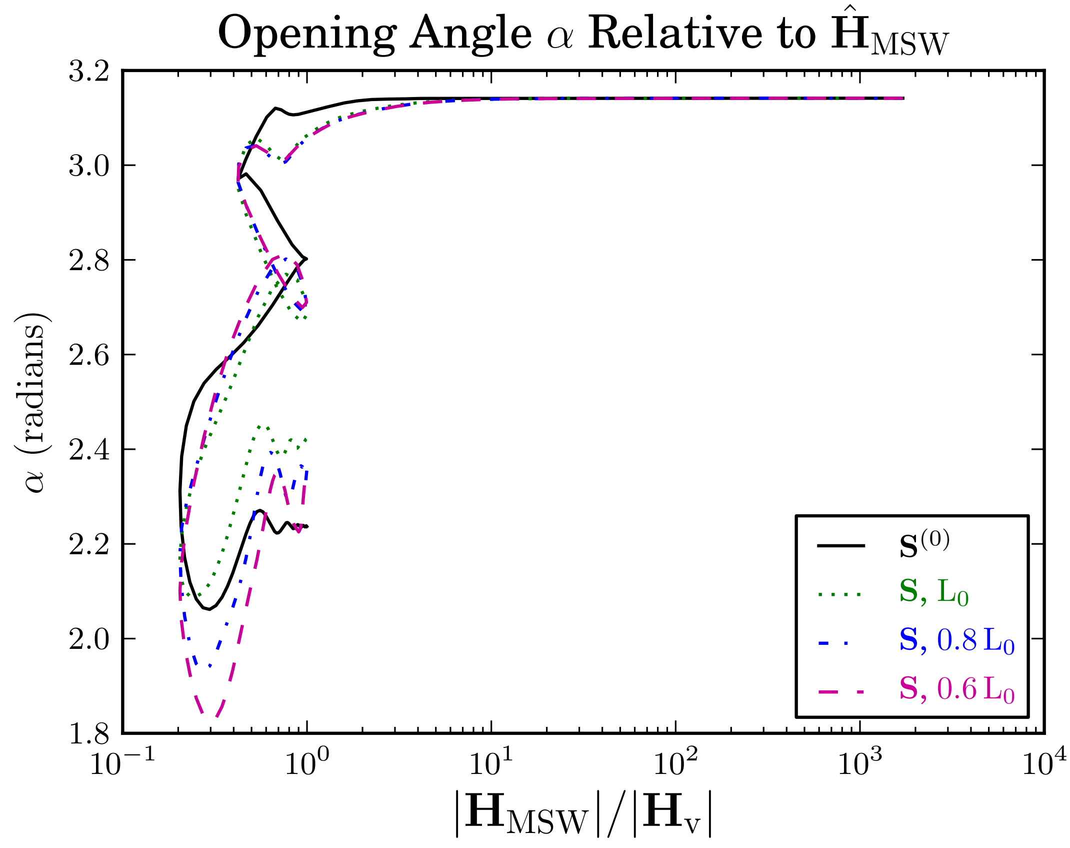

Figure 4.23: Moderate luminosity evolution ($L_0 = 10^{53}\,\mathrm{erg\,s}^{-1}$): The opening angle α between the collective NFIS $\mathbf{S}^{(0)}$ and $\mathbf{H}_{\mathrm{MSW}}$, plotted as a function of $|\mathbf{H}_{\mathrm{MSW}}|\,/\,|\mathbf{H}_{\mathrm{v}}|$ as the system moves through resonance. The idealized NFIS (solid line) shows the evolution of $\mathbf{S}^{(0)}$ in the ideal, strong neutrino self-coupling case. The dashed line, dot-dashed line, and dotted line show the evolution of $\mathbf{S}$ as calculated for neutrino luminosities $L_0,\ 0.8\,L_0,$ and $0.6\,\mathrm{L}_0$ respectively.

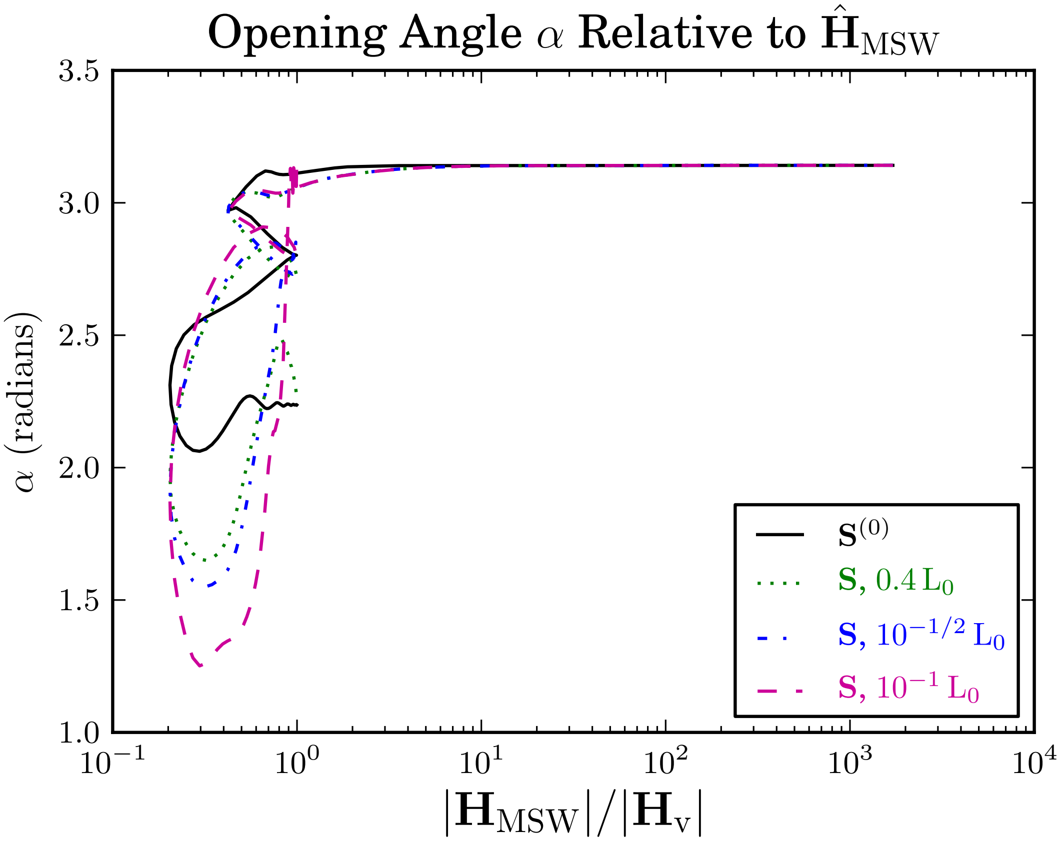

Figure 4.24: Low luminosity evolution ($L_0 = 10^{53}\,\mathrm{erg\,s^{-1}}$): The opening angle α between the collective NFIS $\mathbf{S}^{(0)}$ and $\mathbf{H}_{\mathrm{MSW}}$, plotted as a function of $|\mathbf{H}_{\mathrm{MSW}}|\,/\,|\mathbf{H}_{\mathrm{v}}|$ as the system moves through resonance. The idealized NFIS (solid line) shows the evolution of $\mathbf{S}^{(0)}$ in the ideal, strong neutrino self-coupling case. The dashed line, dot-dashed line, and dotted line show the evolution of $\mathbf{S}$ as calculated for neutrino luminosities $0.4\,L_0,\ 10^{-1/2}\,L_0,$ and $10^{-1}\,\mathrm{L}_0$ respectively.

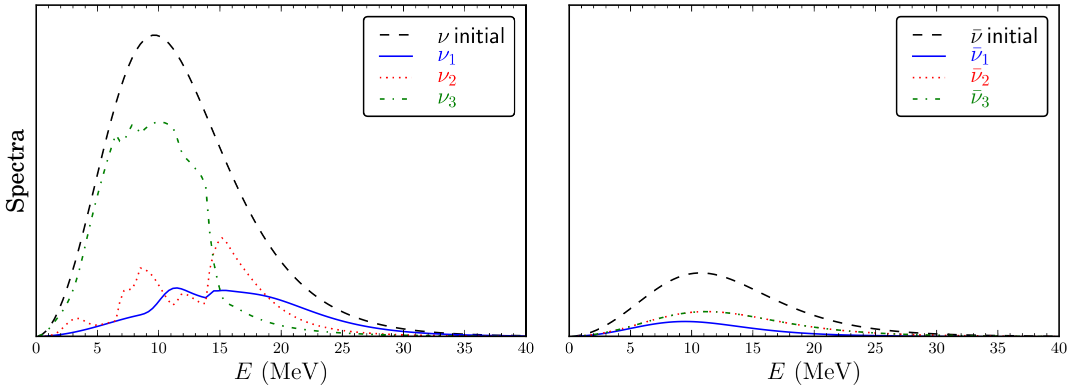

Figure 4.25: The expected signal from the neutronization burst of Ref. [4], in the normal neutrino mass hierarchy, created by integrating the final emission angle averaged neutrino spectral energy distribution and fluxes over the first 30 ms of the neutrino burst signal. Left: Scaled neutrino number flux, summed over all neutrino flavors, shown in the vacuum mass basis. Right: Scaled anti-neutrino number flux, summed over all neutrino flavors, shown in the vacuum mass basis.

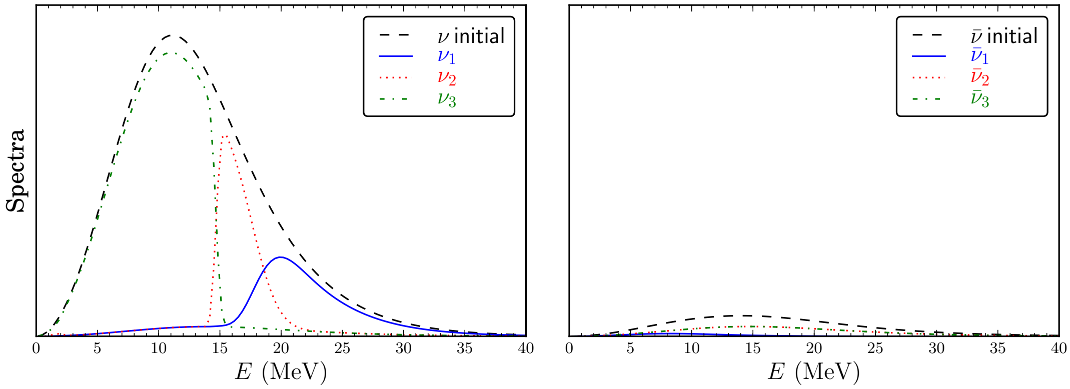

Figure 4.26: The expected signal from the neutronization burst of Ref. [5], in the normal neutrino mass hierarchy, created by integrating the final emission angle averaged neutrino spectral energy distribution and fluxes over the first 30 ms of the neutrino burst signal. Left: Scaled neutrino number flux, summed over all neutrino flavors, shown in the vacuum mass basis. Right: Scaled anti-neutrino number flux, summed over all neutrino flavors, shown in the vacuum mass basis.

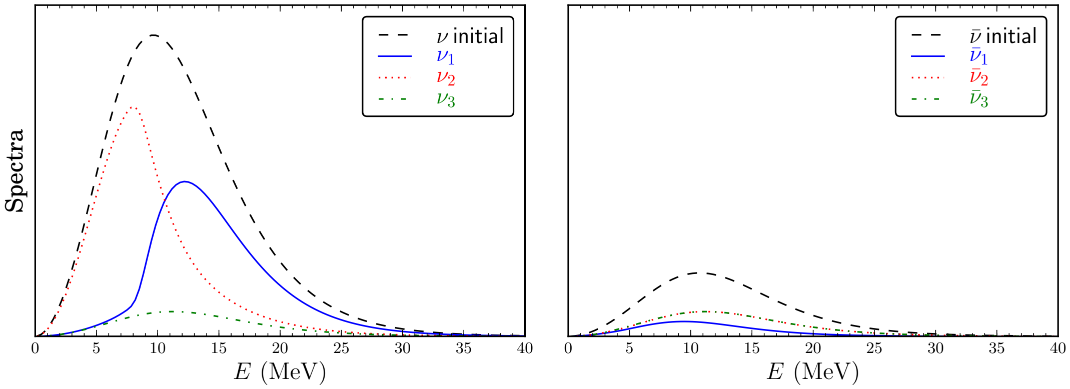

Figure 4.27: The expected signal from the neutronization burst of Ref. [4], in the inverted neutrino mass hierarchy, created by integrating the final emission angle averaged neutrino spectral energy distribution and fluxes over the first 30 ms of the neutrino burst signal. Left: Scaled neutrino number flux, summed over all neutrino flavors, shown in the vacuum mass basis. Right: Scaled anti-neutrino number flux, summed over all neutrino flavors, shown in the vacuum mass basis.

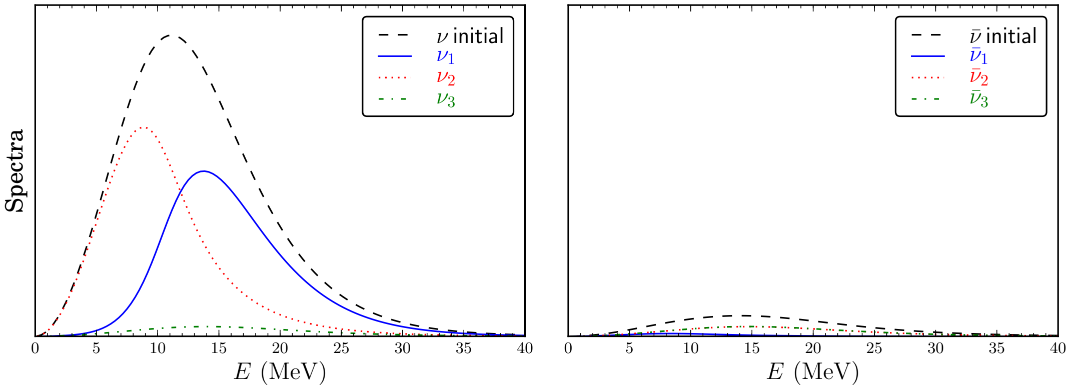

Figure 4.28: The expected signal from the neutronization burst of Ref. [5], in the inverted neutrino mass hierarchy, created by integrating the final emission angle averaged neutrino spectral energy distribution and fluxes over the first 30 ms of the neutrino burst signal. Left: Scaled neutrino number flux, summed over all neutrino flavors, shown in the vacuum mass basis. Right: Scaled anti-neutrino number flux, summed over all neutrino flavors, shown in the vacuum mass basis.

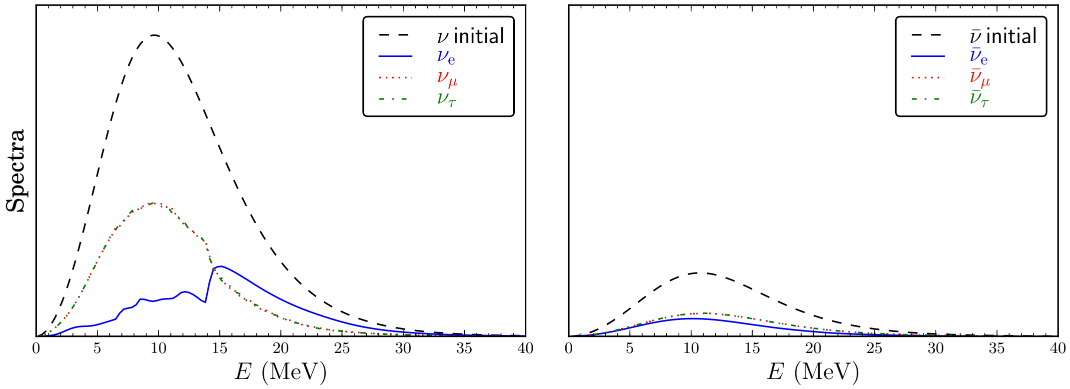

Figure 4.29: The expected signal from the neutronization burst of Ref. [4], in the normal neutrino mass hierarchy, created by integrating the final emission angle averaged neutrino spectral energy distribution and fluxes over the first 30 ms of the neutrino burst signal. Left: Scaled neutrino number flux, summed over all neutrino flavors, shown in the neutrino flavor basis. Right: Scaled anti-neutrino number flux, summed over all neutrino flavors, shown in the neutrino flavor basis.

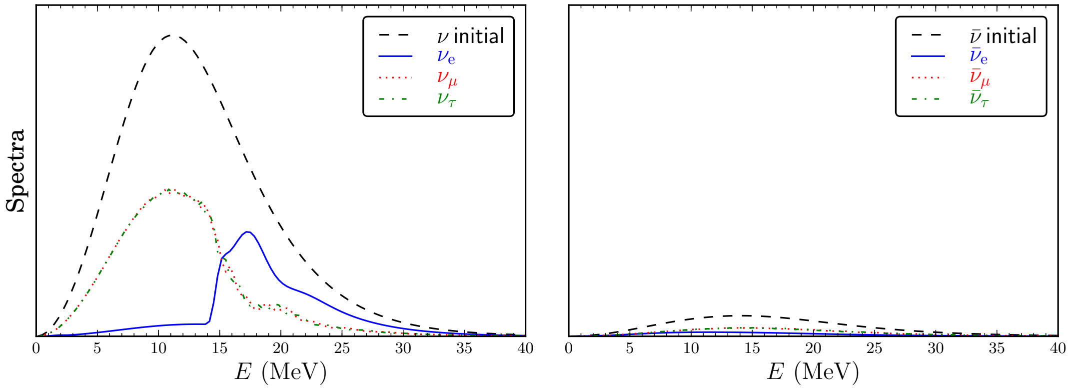

Figure 4.30: The expected signal from the neutronization burst of Ref. [5], in the normal neutrino mass hierarchy, created by integrating the final emission angle averaged neutrino spectral energy distribution and fluxes over the first 30 ms of the neutrino burst signal. Left: Scaled neutrino number flux, summed over all neutrino flavors, shown in the neutrino flavor basis. Right: Scaled anti-neutrino number flux, summed over all neutrino flavors, shown in the neutrino flavor basis.

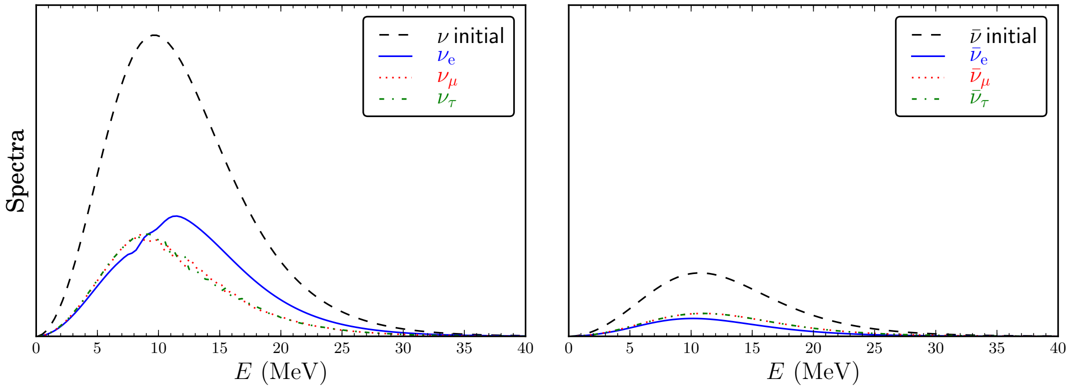

Figure 4.31: The expected signal from the neutronization burst of Ref. [4], in the inverted neutrino mass hierarchy, created by integrating the final emission angle averaged neutrino spectral energy distribution and fluxes over the first 30 ms of the neutrino burst signal. Left: Scaled neutrino number flux, summed over all neutrino flavors, shown in the neutrino flavor basis. Right: Scaled anti-neutrino number flux, summed over all neutrino flavors, shown in the neutrino flavor basis.

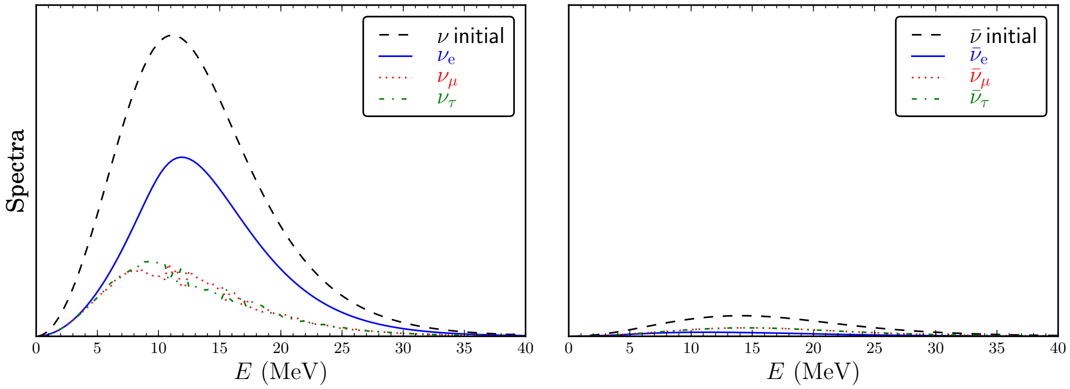

Figure 4.32: The expected signal from the neutronization burst of Ref. [5], in the inverted neutrino mass hierarchy, created by integrating the final emission angle averaged neutrino spectral energy distribution and fluxes over the first 30 ms of the neutrino burst signal. Left: Scaled neutrino number flux, summed over all neutrino flavors, shown in the neutrino flavor basis. Right: Scaled anti-neutrino number flux, summed over all neutrino flavors, shown in the neutrino flavor basis.

Chapter 5

The Neutrino Halo

5.1 Issues with Neutrino Scattering

Two roads diverged in a wood, and I —
I took the one less traveled by,
And that has made all the difference.
— Robert Frost, *Mountain Interval* (1920)

5.1.1 Direction Changing Scattering

Now I shall point out a surprising feature of neutrino flavor transformation in core-collapse supernovae. All collective neutrino flavor transformation calculations employ the “Neutrino Bulb” model, where neutrino emission is sourced from the neutrinosphere, taken to be a hard spherical shell from which neutrinos freely stream. This seems like a reasonable approximation because well above the neutrinosphere scattered neutrinos comprise only a relatively small fraction of the overall neutrino number density. However, this optically thin “halo” of scattered neutrinos nonetheless may influence the way flavor transformation proceeds. This result stems from a combination of the geometry of supernova neutrino emission, as depicted in Fig. 5.1, and the neutrino intersection angle dependence of neutrino-neutrino coupling.

Neutrinos are emitted in all directions from a neutrinosphere of radius R_ν,

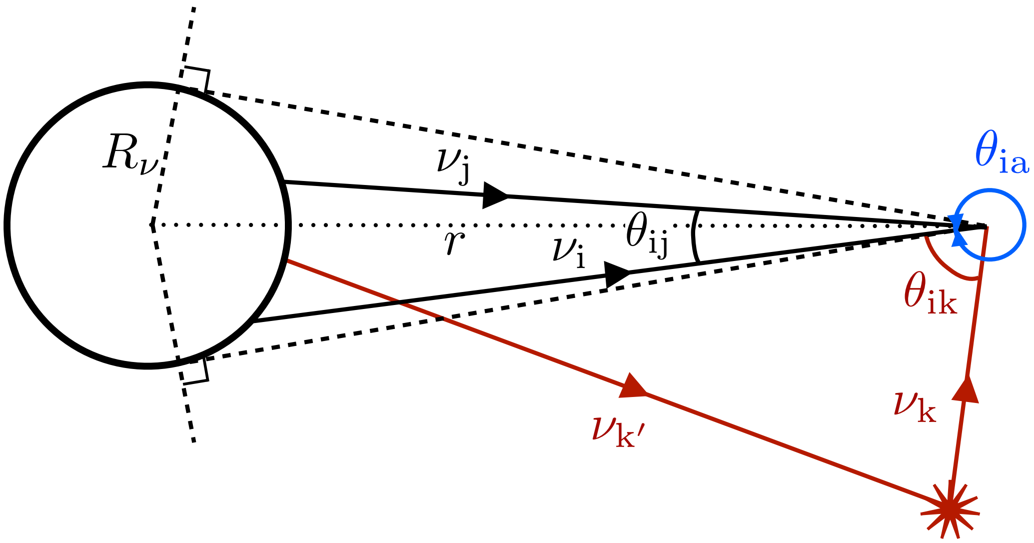

Figure 5.1: Supernova neutrino emission geometry.

but those that arrive at a location at radius r, and suffer only forward scattering, will be confined to a narrow cone of directions (dashed lines in Fig. 5.1) when $r \gg R_\nu$. In contrast, a neutrino which suffers one or more direction-changing scattering events could arrive at the same location via a trajectory that lies well outside this cone.

Following neutrino flavor evolution in the presence of scattering, in general, requires a solution of the quantum kinetic equations [95, 96, 97]. However, the rare nature of the scattering that generates the halo suggests a separation between the scattering-induced and coherent aspects of neutrino flavor evolution. In the coherent limit the neutrino-neutrino Hamiltonian, $\hat{H}_{\nu\nu}$, couples the flavor histories for neutrinos on intersecting trajectories [95, 56, 75, 46]. As shown in Fig. 5.1, a neutrino $\nu_{\rm i}$ leaving the neutrinosphere will experience a potential given by a sum over neutrinos and antineutrinos located at the same point as neutrino $\nu_{\rm i}$:

$$\begin{aligned} \hat{H}_{\nu\nu} &= \sqrt{2}\,G_{\rm F} \sum_{\rm a} (1-\cos\theta_{\rm ia})\, n_{\nu,{\rm a}}\, |\psi_{\nu,{\rm a}}\rangle\, \langle\psi_{\nu,{\rm a}}| \\ &- \sqrt{2}\,G_{\rm F} \sum_{\rm a} (1-\cos\theta_{\rm ia})\, n_{\bar\nu,{\rm a}}\, |\psi_{\bar\nu,{\rm a}}\rangle\, \langle\psi_{\bar\nu,{\rm a}}|, \end{aligned} \tag{5.1}$$

where the flavor state of neutrino $\nu_{\rm a}$ is represented by $|\psi_{\nu,{\rm a}}\rangle$, and $\theta_{\rm ia}$ is the angle of intersection between $\nu_{\rm i}$ and neutrino or antineutrino $\nu_{\rm a}/\bar\nu_{\rm a}$. Here $n_{\nu,{\rm a}}$ is the local number density of neutrinos in state a, and the $1 - \cos\theta_{\mathrm{ia}}$ factor disfavors small intersection angles, thereby suppressing the potential contribution of the forward-scattered-only neutrinos [24, 25]. Direction-altered scattered neutrinos may have larger intersection angles as shown in Fig. 5.1, and therefore can contribute significantly to the flavor-changing potentials, despite their small numbers.

In the mean-field, coherent approximation, neutrino flavor evolution is governed by a Schrödinger-like equation [64], $i\partial|\psi_{\nu,\mathrm{i}}\rangle/\partial t = \hat{H}|\psi_{\nu,\mathrm{i}}\rangle$, where t is an affine parameter along neutrino ν_{i}'s world line, and $\hat{H} = \hat{H}_{\mathrm{V}} + \hat{H}_{\mathrm{e}} + \hat{H}_{\nu\nu}$ is the appropriate neutrino propagation Hamiltonian, with vacuum and matter components $\hat{H}_{\mathrm{V}}$ and $\hat{H}_{\mathrm{e}}$, respectively. $\hat{H}_{\nu\nu}$ can be split into two pieces: $\hat{H}_{\nu\nu}^{\mathrm{bulb}}$, contributed by neutrinos (index j in Fig. 5.1) which propagate directly (straight lines) from the surface of the neutrinosphere; and $\hat{H}_{\nu\nu}^{\mathrm{halo}}$, contributed by neutrinos that suffer direction-changing scattering outside the neutrinosphere (index k in Fig. 5.1) and propagate coherently thereafter. To wit, $\hat{H}_{\nu\nu} = \hat{H}_{\nu\nu}^{\mathrm{bulb}} + \hat{H}_{\nu\nu}^{\mathrm{halo}}$.

The operators $\hat{H}_{\nu\nu}^{\mathrm{halo}}$ and $\hat{H}_{\nu\nu}^{\mathrm{bulb}}$ depend on the complex phases of the neutrino flavor states which contribute to them, so that the relative leverage of these operators in determining flavor transformation at any point requires numerical calculations. Some conditions have been shown to give phase locking, while other conditions give phase decoherence [56, 29, 37, 46, 51]. For the purpose of evaluating the validity of the Neutrino Bulb model, I ignore path length difference-induced phase averaging [56] and compute the *maximum* magnitude of the diagonal Hamiltonian elements, which I denote with $|\hat{H}_{\nu\nu}^{\mathrm{halo}}|$ and $|\hat{H}_{\nu\nu}^{\mathrm{bulb}}|$. A necessary condition for the validity of the Neutrino Bulb model is that $|\hat{H}_{\nu\nu}^{\mathrm{bulb}}| \gg |\hat{H}_{\nu\nu}^{\mathrm{halo}}|$.

5.1.2 The Safety Criterion

A simple argument can be made about which varieties of spherically symmetric density profiles could render the Neutrino Bulb model inadequate. Consider a series of spherical shells of matter stacked around the neutrinosphere. These shells are taken to isotropically scatter neutrinos, and, as I discuss below, neutral current neutrino-nucleon/nucleus scattering does just this. Some of these neutrinos will contribute number density and flavor information to the sum in Eq. 5.1, adding to $\hat{H}_{\nu\nu}^{\rm halo}$. For a point r well outside of these shells, the number density of neutrinos being scattered to this location from a shell at radius r', multiplied by the average value of $(1-\cos\theta_{\rm ik})$ for neutrinos coming from this shell, is $\propto \rho\,(r')\,\delta r'\,(r'/R_\nu)^2$, where $\delta r'$ is the thickness of the shell. As r' approaches r, the contribution from these shells is regulated. For small r', the shell contributions are regulated by the neutrinosphere.

These considerations imply that when $\rho\,(r') \propto r'^{-3}$, the potential contributed by a given shell will be $\propto \delta r'/r' \propto \delta \log\,(r')$. Any selection of logarithmically spaced shells with $r' < r$ will cause each shell to make an equal contribution of neutrino number density at r. Physically, one might expect density features of size r' at radius r'. This matter density configuration will cause the ratio of $|\hat{H}_{\nu\nu}^{\rm halo}|/|\hat{H}_{\nu\nu}^{\rm bulb}|$ to remain fixed with increasing radius.

To compare the contributions of the halo shells to $|\hat{H}_{\nu\nu}^{\rm bulb}|$, I observe that the neutrinosphere (more precisely, the *transport sphere* [98]) can be treated in the same spirit. The transport sphere is characterized by the neutrino optical depth, τ, equal to unity. Requiring that the logarithmic shells above the neutrinosphere contribute much less than the neutrinosphere itself results in

$$\rho\,(r) \ll \rho_{\tau=1}\left(\frac{R_\nu}{r}\right)^3 \; . \tag{5.2}$$

Early in the explosion epoch, the transport sphere corresponds to physical radii $R_\nu \sim 30-60$ km and densities $\rho_{\tau=1} \sim 10^{(11 \text{ to } 12)}\,\mathrm{g\,cm^{-3}}$ [98]. In fact, Eq. 5.2 assumes that the thickness ΔR_ν of the neutrinosphere is $\sim R_\nu$, whereas models show that $\Delta R_\nu < R_\nu$, implying a more stringent constraint by a factor of $\Delta R_\nu/R_\nu$.

If $|\hat{H}_{\nu\nu}^{\rm halo}|/|\hat{H}_{\nu\nu}^{\rm bulb}| < 1\,\%$ is taken as the limit where $\hat{H}_{\nu\nu}^{\rm halo}$ can be neglected, then by Eq. 5.2 the range of density profiles for which the Neutrino Bulb model is likely to be adequate is $\rho\,(r) < 0.01 \times \rho_{\tau=1}\,(R_\nu/r)^3$. As long as the matter density in the supernova remains below this limit, there is no danger that the fractional potential contribution from the scattered halo, $|\hat{H}_{\nu\nu}^{\rm halo}|$, will grow above $1\,\%$ anywhere in the supernova envelope. Fig. 5.2 shows the density profiles for several core-collapse supernova environments alongside the corresponding $1\,\%$ safety criterion for each profile. This $1\,\%$ criterion is chosen to be commensurate with the typical level of convergence accuracy in existing flavor transformation simulations.

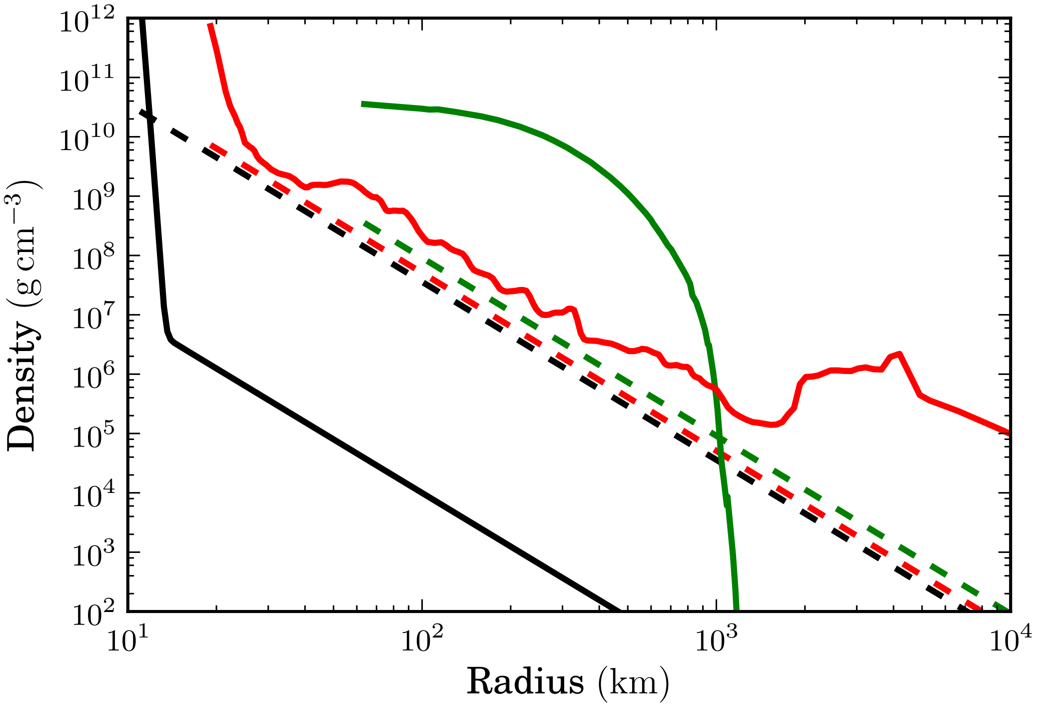

Figure 5.2: Solid lines show matter density profiles and dashed lines the corresponding Neutrino Bulb (1 %) safety criteria from Eq. 5.2. Black lines are for the late-time neutrino driven wind environment [6], green lines the neutronization burst O-Ne-Mg core-collapse environment [2, 3], and red lines the Fe-core-collapse shock revival environment [7].

As is evident in Fig. 5.2, the Fe-core-collapse shock revival environment will have a significant scattered halo. Even though the O-Ne-Mg core-collapse density profile [2, 3] drops into the safe zone at $r > 1000\,\mathrm{km}$, these models nevertheless will have a significant scattered halo originating from shells at lower radius where the density curve is above the $1\,\%$ safety margin. Only late-time neutrino-driven wind models avoid scattered halo complication [6, 99, 39, 43, 100, 5, 47]. Fe-core-collapse models (e.g., the red curve in Fig. 5.2), in general, exhibit an average density profile that is $\propto r^{-(2 \text{ to } 3)}$, which means that $|\hat{H}_{\nu\nu}^{\mathrm{halo}}|/|\hat{H}_{\nu\nu}^{\mathrm{bulb}}|$ is expected to increase with radius. Note, however, that though the relative contribution of the halo may grow with radius, at sufficiently large distance from the proto-neutron star the neutrino-neutrino potential ceases to be physically important.

5.1.3 Implicit Calculation of the Halo

Matter inhomogeneity, an essential feature of supernova explosion models [101, 102, 20, 12, 19, 7, 21], adds complexity to this issue. To study this effect I use the 2D matter density distribution, Fig. 5.3, taken from a supernova model derived from a $15\,M_\odot$ progenitor [7]. This snapshot corresponds to 500 ms after core bounce, during the shock revival epoch, after the onset of the SASI [12, 19]. I mock up a full 3D density profile by cloning the 2D profile into a 3D data cube. Starting with an initial flux of neutrinos from the neutrinosphere [65], and taking all baryons to be free nucleons, I use the full energy dependent neutral current neutrino-nucleon scattering cross sections [14] to calculate the number flux of neutrinos scattered out of each spatial zone and into every other spatial zone (retaining the necessary information about relative neutrino trajectories between zones). I compute the magnitude of $|\hat{H}_{\nu\nu}^{\mathrm{halo}}|$ at each location in the 2D slice that comprises the original density distribution.

The number density of forward-scattered-only neutrinos above the neutrinosphere can be approximated as,

$$dn_{\nu,\mathrm{a}}\left(r\right) = \frac{L_{\nu,\mathrm{a}}}{\langle E_{\nu,\mathrm{a}}\rangle \pi R_\nu^2} \frac{d\Omega_{\nu,\mathrm{a}}}{4\pi} f_{\nu,\mathrm{a}}\left(E_\nu\right) dE_\nu \ , \tag{5.3}$$

where $L_{\nu,\mathrm{a}}$ is the luminosity and $\langle E_{\nu,\mathrm{a}}\rangle$ is the average energy of the a^{th} neutrino or

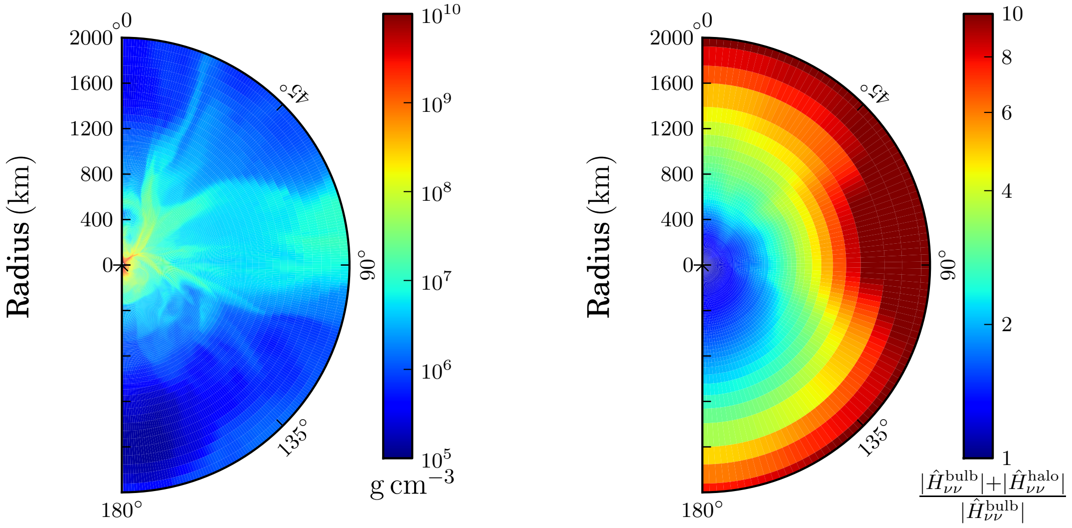

Figure 5.3: Left: Color scale indicates the density within the shock front in a $15\,M_\odot$ progenitor core-collapse supernova 500 ms after core bounce, during the shock revival epoch [7]. Right: Effect of the scattered neutrino halo for the matter distribution at Left. Color scale indicates the ratio of the sum of the maximum (no phase averaging) magnitudes of the constituents of the neutrino-neutrino Hamiltonian, $|\hat{H}^{\text{bulb}}_{\nu\nu}| + |\hat{H}^{\text{halo}}_{\nu\nu}|$, to the contribution from the neutrinosphere $|\hat{H}^{\text{bulb}}_{\nu\nu}|$.

anti-neutrino, $d\Omega_{\nu,\mathrm{a}}$ is a pencil of directions that connects the neutrinosphere and location $\vec{r}$, and $f_{\nu,\mathrm{a}}\left(E_\nu\right)$ is the normalized neutrino energy distribution function.

The local number density of neutrinos which have suffered direction-changing scattering is found by performing integrals over the neutrino number flux in Eq. 5.3, energy-dependent scattering kernels, and the geometry of the matter envelope above the proto-neutron star. I define $K_{\mathrm{g,k}'}\left(\vec{r}-\vec{r'},E_\nu\right)$ as the effective scattering kernel (with the dimensions of cross section) for process g to scatter neutrino k$'$ onto a trajectory that connects locations $\vec{r'}$ and $\vec{r}$, and $n_{\mathrm{g}}\left(\vec{r'}\right)$ as the local number density of scattering targets for process g. For scattering originating in volume element dV', for neutrinos of species a, the contribution to $|\hat{H}_{\nu\nu}^{\mathrm{halo}}|$ for a radially directed neutrino at location $\vec{r}$ is,

$$\left(1-\cos\theta_{\mathrm{ia}}\right)n_{\nu,\mathrm{a}}\left(\vec{r}\right)=\sum_{\mathrm{g}}\int_{V'}\int_{\Omega_{\nu,\mathrm{k}}}\int_{n_{\nu,\mathrm{a}}}\left(1-\frac{\vec{r}\cdot\left(\vec{r}-\vec{r'}\right)}{|\vec{r}\cdot\left(\vec{r}-\vec{r'}\right)|}\right)$$

$$\times K_{\mathrm{g,k}'}\left(\vec{r}-\vec{r'},E_\nu\right)n_{\mathrm{g}}\left(\vec{r'}\right)dn_{\nu,\mathrm{a}}\left(r'\right)\frac{d\Omega_{\nu,\mathrm{k}}}{4\pi^2\left(dr'_{\nu,\mathrm{k}}\right)^2}dV'\ , \tag{5.4}$$

where $d\Omega_{\nu,\mathrm{k}}$ is a pencil of directions connecting the scattering location and $\vec{r}$, and $dr'_{\nu,\mathrm{k}}$ is the length scale of the volume element at the scattering location, which I have included in the expression to make the effect of finite size volume elements in the numerical evaluation of Eq. 5.4 obvious. Note that in all limits, $\int\frac{d\Omega_{\nu,\mathrm{k}}}{\left(dr'_{\nu,\mathrm{k}}\right)^2}$ is finite. Once all the Hamiltonian contributions from Equation 5.4 have been computed, they can be directly taken and used in the sum in Equation 5.1, once one applies a consistent prescription for the elements of $|\psi_{\nu,\mathrm{a}}\rangle\langle\psi_{\nu,\mathrm{a}}|$. Because I am comparing $|\hat{H}_{\nu\nu}^{\mathrm{halo}}|$ and $|\hat{H}_{\nu\nu}^{\mathrm{bulb}}|$, the prescription that I employ is simply that $|\psi_{\nu,\mathrm{a}}\rangle\langle\psi_{\nu,\mathrm{a}}|\equiv I$, where I is the identity matrix, for all neutrino species.

In this example calculation the scattered halo is taken to be composed of neutrinos which have suffered only a single direction-changing scattering. Because the halo region is optically thin for neutrinos, multiple scatterings become increasingly rare with radius and do not have a geometric advantage in their contribution to $|\hat{H}_{\nu\nu}^{\mathrm{halo}}|$ relative to singly-scattered neutrinos. Neutrinos which experience direction-changing scattering that takes them into the same cone of directions as neutrinos forward scattering from the neutrinosphere are counted as contributing to the halo (these neutrinos contribute $\sim 10^{-6}$ of the halo potential). As before, I neglect the effects of neutrino flavor oscillations. Fig. 5.3 shows the results of this calculation out to a radius of $r = 2000\,\mathrm{km}$.

In supernova models the bulk of the direct neutrino-capture heating occurs at radius $\sim 100\,\mathrm{km}$. This will be below the region of collective oscillations in the *absence* of the halo. For example, absent the halo, neutrinos propagating through the density profile of Fig. 5.3 will begin flavor transformation at a radius of $r \sim 300-400\,\mathrm{km}$, and finish flavor transformation at $r \sim 1000\,\mathrm{km}$ [47]. The effects of the halo on this picture remain to be calculated. Disturbingly, neutrinos from the scattered halo in this 2D model nowhere contribute a maximum magnitude less than 14 % of the neutrino-neutrino potential magnitude, and in many places contribute 90 % or more of the total.

Fig. 5.3 also shows that matter inhomogeneities generate large corresponding scattered halo inhomogeneities. Furthermore, the inhomogeneity of the scattered halo is increased by several scattering processes which have been omitted from this illustrative calculation. I did not include neutrino-electron scattering. This scattering process has smaller cross sections and relatively forward peaked angular distributions and therefore produces a subdominant contribution to $|\hat{H}_{\nu\nu}^{\mathrm{halo}}|$. What is more important is that our calculation leaves out what is likely the dominant source of neutrino direction-changing scattering in the low entropy regions of the supernova envelope: coherent neutrino-nucleus neutral current scattering.

The cross sections for this process scale as the square of the neutrino energy and square of the nuclear mass number A. In fact, since the proper number density of nuclear targets is $\propto A^{-1}$, but the coherent scattering cross section $\propto A^2$, the overall scattered halo potential contribution stemming from this process is $\propto A$. This process, like neutral current neutrino-nucleon scattering, is flavor independent and flavor preserving, simply changing neutrino direction.

Since the heavy nucleus mass fraction, and the distribution of nuclear mass numbers, can depend sensitively on the entropy and electron fraction [9], coherent neutral current scattering could couple neutrino flavor transformation to macroscopic, multi-dimensional structures in the supernova envelope. For example, the model shown in Fig. 5.3 has relatively lower entropy, downward-flowing, higher nuclear mass fraction matter; and higher entropy, upward-flowing plumes, with relatively lower nuclear mass fraction. This could produce a scattered halo with a complicated 3D geometry and flavor content, creating a non-trivial enhancement to the inhomogeneities evident in the scattered halo potential shown in Fig. 5.3.

Because scattering processes are energy dependent, neutrinos in the scattered halo possess different energy spectra than forward-scattered only neutrinos. Furthermore, the flavor content of the scattered halo will not match that of neutrinos emerging from the neutrinosphere. For example, consider emergent ν_{e} and $\bar{\nu}_{\mathrm{e}}$ number fluxes that are equal, yet have different energy spectra. Taken alone, unmolested by neutrino flavor oscillations, these fluxes give $|\hat{H}_{\nu\nu}^{\mathrm{bulb}}| = 0$. However, passing through the energy-dependent scattering processes, they yield $|\hat{H}_{\nu\nu}^{\mathrm{halo}}| \neq 0$.

Anticipating the course of neutrino flavor evolution in this environment is clearly challenging. $|\hat{H}_{\mathrm{e}}|$ is by far the largest contribution to $|\hat{H}|$ during the shock revival epoch. However, considering the Bulb neutrinos alone, current coherent calculations show that neutrino collective flavor oscillations can proceed despite a large matter potential [30, 32, 6, 33]. The criterion for the matter suppression of collective oscillations [103], $\Delta|\hat{H}_{\mathrm{e}}| \sim \Delta|\hat{H}_{\mathrm{V}}|$, where Δ denotes the *dispersion* in these potentials for Bulb neutrinos, is not met where the matter densities in Fig. 5.3 drop below $\sim 10^{7\text{ to }8}\,\mathrm{g\,cm^{-3}}$ (the wide range is due to the geometric dependence of $\Delta|\hat{H}_{\mathrm{e}}|$). In a further complication, neutrinos from the spatially extended scattered halo could arrive at a given location along many different trajectories with different path lengths, so that significant neutrino oscillation phase averaging [56] could come into play. This has been shown to suppress collective oscillations in some conditions [47]. Inhomogeneity and the intersection angle dependence of the neutrino-neutrino interaction may make phase averaging incomplete. Ascertaining the role of decoherence and phase averaging processes requires detailed calculation with specific supernova models [51]. Even if collective oscillations are found to be suppressed at small radius, they may be operating, e.g. above the shock, because the halo extends the collective oscillation region.

Though validating coherent flavor transformation studies for late-time neutrino driven wind models, our calculations demonstrate the potential inadequacy of these treatments in an environment important for the understanding of the supernova explosion mechanism and nucleosynthesis. Ultimately, the scattered halo changes the nature of the neutrino flavor transformation problem: it broadens the region influencing flavor evolution from just the neutrinosphere to a much larger fraction of the supernova envelope; and it introduces essential multi-dimensional effects. The standard Neutrino Bulb model by its nature is an initial value problem at each radius r, while the scattered halo makes it necessary to consider how flavor transformations at large radii can feed back into the evolution at smaller radii. With this additional source of nonlinearity, qualitatively new phenomena could, in principle, occur. Further, the extended scattered halo can couple neutrino flavor evolution to the nuclear composition and complex 3D flow geometries which are characteristics of the supernova explosion epoch. A self-consistent solution of this problem likely will demand new computational capabilities and approaches. Given the importance of neutrinos and the supernova phenomenon for so many aspects of our understanding of the cosmos, it may be that there is no choice but to seek such a solution.

5.2 Flavor Transformation During the Accretion and SASI phases

A widely used method for evaluating the flavor transformation properties of a system of neutrinos is called the linearized stability analysis. This method is explained in great detail in Ref. [49]. The essence of the linearized stability analysis prescription is to insist on solutions to Equation 2.25 that are of the form $\mathbf{s}_{\mathrm{i}} = \mathbf{A}_{\mathrm{i}} e^{-i\Omega r}$ where Ω is complex. One can then expand Equation 2.25 to linear order and solve a set of integral eigenvalue equations at fixed radius. If a solution is discovered where the imaginary portion of $\Omega = \gamma + i\kappa$ is large and positive, then there exists the possibility that neutrinos will rapidly alter their flavor states, which is refered to as flavor “instability”. Broadly speaking, if $\kappa r < 1$ at some fixed radius r, then there will be no large scale flavor oscillations, and hence the neutrino flavor states are stable in their initial configurations. The analysis is then repeated, stepping outward in radius and re-evaluating the stability of the neutrino flavor states.

One of the key features of this analysis is the effect that dispersion has on collective neutrino flavor oscillations. The NFISs of all neutrinos emitted from the neutrinosphere will oscillate about the total potential vector $\mathbf{H}_{\mathrm{i}}$ at some frequency. The degree to which these neutrinos can engage in collective phenomena is dependent on how closely their flavor oscillation frequencies match up, i.e. how much dispersion is present. This dispersion depends not only on the neutrino energies and relative path lengths of the neutrino trajectories, but on both matter [103] and neutrino-neutrino [47] interactions as well. Depending on the details of the neutrino emission geometry and spectra, and on the matter density, the dispersion across different neutrino trajectories emerging from the neutrinosphere may or may not suppress collective oscillations (e.g. damping the magnitude of κ [49]).

5.2.1 Flavor Transformation is now a Boundary Value Problem

In order to include the neutrino halo in a neutrino flavor transformation analysis or calculation it must first and foremost be recognized that the halo itself represents a set of outer boundary conditions that must be accounted for. Neutrinos which scatter onto trajectories that take them deeper into the supernova envelope exist all the way out to the edge of the collapsing star. The halo starts at zero neutrino number density at the edge of the envelope, but has a positive gradient as one moves inward. Furthermore, the initial flavor content of the halo neutrinos is set by neutrino flavor oscillations that are taking place tens of thousands of kilometers deeper within the core.

This is quite distinct from the neutrino bulb model, and the associated linearized stability analysis. These are fundamentally initial value problems. The initial neutrino flavor states and emission energy spectra are set by the conditions near the surface of the proto-neutron star. In such an initial value problem the neutrino flavor evolution is then entirely determined by how the forward scattering potentials at the present radius change / do not change the flavor states of neutrinos as one moves further out in radius. The evolution of neutrino flavor states is directed entirely *downstream*, as the neutrinos propagate outward.

Ref. [104] uses this downstream method to attempt to include the halo in a linearized stability analysis. In order to do this, they exclude halo neutrinos which propagate from larger to smaller radii entirely from their analysis, calling them "backwards-going modes". The most strongly interacting neutrinos are on trajectories which intersect head-on or nearly so, and, as result, the neutrinos that scatter backwards after leaving the neutrinosphere have an enhanced purchase on the neutrino-neutrino potential for neutrinos emitted from the neutrinosphere. These so called "backwards-going modes" in fact constitute the bulk of the neutrino halo potential out to large radii (specifically, large compared to the shock front radius for the accretion and shock revival epochs) for massive star progenitors. Using the neutrino emission spectra and an analytic fit to the density profile of the calculations in [8] and [104], I have computed the fractional contribution that the outward directed and inward directed halo neutrinos make to the total halo potential. This is shown if Figure 5.4. From this plot it is clear that within the inner portions of the supernova envelope, the neutrinos which have scattered backward from larger radius are far from negligible, and constitute some $\sim 80\,\%$ of the total halo potential or more within the shock front at $r = 70\,\mathrm{km}$ [8].

5.2.2 Multi-dimensionality

If one wishes to include the neutrino halo in any initial value problem analysis of neutrino flavor transformation in the supernova environment, the fundamentally multi-dimensional nature of the halo must be addressed. Figure 5.4 brings precisely this problem to the foreground. To make a genuine calculation of $\mathbf{H}_{\nu\nu}^{\mathrm{halo}}$, one must also calculate the evolution of neutrino flavor states for neutrinos traveling backwards in radial coordinate. This is a process which is manifestly absent from any from initial value formulation of neutrino flavor transformation.

While the halo neutrinos obey Eq. 2.25 as they propagate along their trajectories, oscillating about the instantaneous mass eigenbasis just as neutrinos

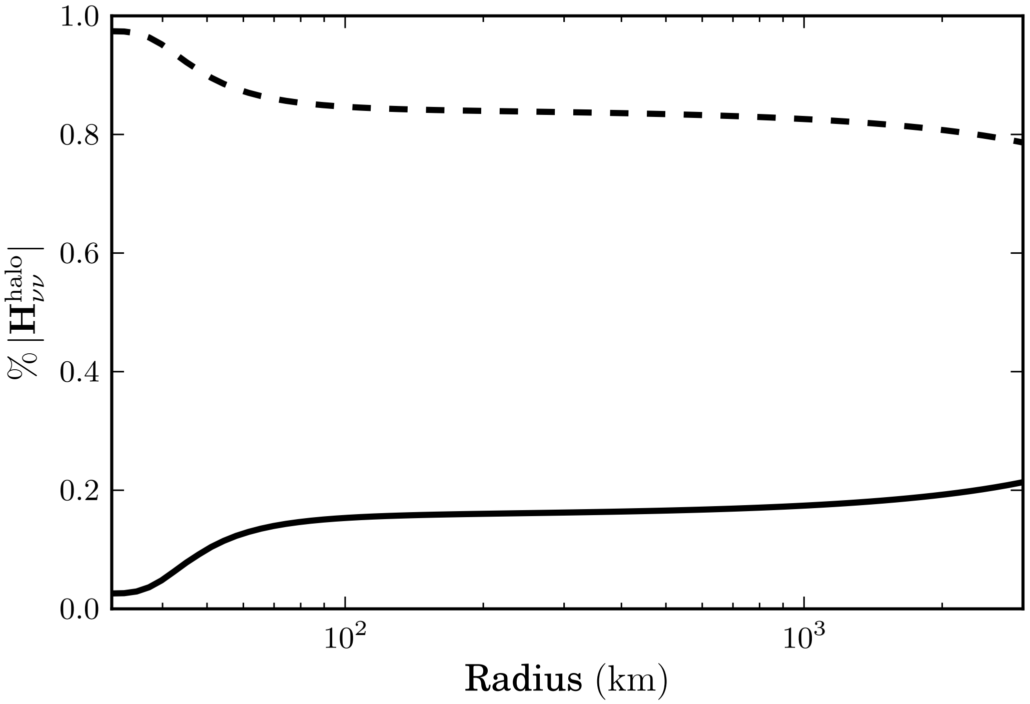

Figure 5.4: Fractional contribution of inward directed neutrinos (dashed line) and outward directed neutrinos (solid line) to the magnitude of the halo neutrino potential $|\mathbf{H}_{\nu\nu}^{\mathrm{halo}}|$ at fixed radius, using the density profile and neutrino emission spectra of Ref. [8].

emerging from the neutrinosphere do, the evolution of $\mathbf{H}_{\rm i}$ along a given halo neutrino's world line will be utterly different from that of a neutrino propagating outward from the neutrinosphere. The halo neutrinos will pass through a matter density profile that is quite distinct from the matter density experienced by neutrinos emerging form the neutrinosphere, and halo neutrinos have a much larger coupling to $\mathbf{H}_{\nu\nu}^{\rm bulb}$ due to the wide angles with which they intersect the neutrinos propagating out from the core.

Without a self consistent solution for the flavor transformation of the halo neutrinos both before and after their direction changing scattering, it is an open question how adiabatic their flavor evolution has been (e.g. do the halo neutrinos maintain a constant opening angle between $\mathbf{s}_{\rm i}$ and $\mathbf{H}_{\rm i}$ as they propagate). Due to the large volume over which the halo neutrinos originate, there will be significant phase cancellation of the halo neutrino contributions to Eq. 5.1 when the opening angle between $\mathbf{s}_{\rm i}$ and $\mathbf{H}_{\rm i}$ is large for halo neutrinos [56] (this is likely to happen when matter densities are relatively low, such that $|\mathbf{H}_{\nu\nu}| \sim |\mathbf{H}_{\rm e}|$). Within the context of the linearized stability analysis, the magnitude of this phase cancellation is an entirely free parameter.

5.2.3 Multi-composition

The largest effect on the number density of halo neutrinos, absent in Ref. [104], is coherent enhancement of neutrino-nucleus neutral current scattering. The cross sections for this process scale as the square of the neutrino energy and square of the nuclear mass number A. In fact, since the proper number density of nuclear targets is $\propto A^{-1}$, but the coherent scattering cross section $\propto A^2$, the overall scattered halo potential contribution stemming from this process is $\propto A$. One of the key reasons that the initial bounce shock stalls to become an accretion shock in the early stages of a core-collapse supernova is that the shock must photo-dissociate heavy nuclei streaming downward. At the time of the snapshot used in [104], 280 ms post bounce, most of this material is likely to be silicon group elements, with $A \approx 28$. This means that during the shock revival epoch, and especially the accretion epoch, the magnitude of the neutrino halo potential will be enhanced by an order of magnitude or more [105].

5.2.4 Dispersion and Interference

We discussed briefly in the introduction the importance of dispersion in the development of collective neutrino oscillation and in the linearized stability analysis. For neutrinos streaming outward from the neutrinosphere, the build up of flavor oscillation phase difference between adjacent neutrino trajectories can suppress flavor transformation [56]. However, these flavor oscillation phases are simply combined in superposition, and it is entirely possible that some sources of phase build up interfere destructively with other sources.

Because neutrino-nucleus neutral current scattering processes depend on E_ν^2, neutrinos in the scattered halo possess different energy spectra than bulb neutrinos. Furthermore, it is a general feature of supernova neutrino emission that $\bar{\nu}_\mathrm{e}$ posses hotter spectral energy distributions than ν_e. As a result, $\bar{\nu}_\mathrm{e}$ are preferentially scattered into the halo neutrino population. This means that the *sign* of the halo contribution to Eq. 5.1 is not necessarily the same as that of $\mathbf{H}_{\nu\nu}^{\mathrm{bulb}}$. Because the neutrino-neutrino coupling for halo neutrinos to bulb neutrinos obeys precisely the same geometric relationship as the coupling of bulb neutrinos to each other, one can quickly discover from Ref. [47] that when $\mathbf{H}_{\nu\nu}^{\mathrm{bulb}}$ and $\mathbf{H}_{\nu\nu}^{\mathrm{halo}}$ have a relative sign difference, their contributions to the dispersion will also have a relative sign difference. This means that under certain conditions, the dispersion created by the halo potential contributions will, in fact, destructively interfere with dispersion from $\mathbf{H}_\mathrm{e}$ and $\mathbf{H}_{\nu\nu}^{\mathrm{bulb}}$. Denoting the total number flux of bulb ν_e's and $\bar{\nu}_\mathrm{e}$'s as $\Phi_{\nu_\mathrm{e}}^{\mathrm{bulb}}$ and $\Phi_{\bar{\nu}_\mathrm{e}}^{\mathrm{bulb}}$, Table 5.1 shows (in the absence of collective flavor oscillations) under what conditions the contributions to the dispersion from the halo and bulb neutrinos will interfere constructively and destructively. Table 5.2 shows (in the absence of collective flavor oscillations) under what conditions the contributions to the dispersion from the halo neutrinos and the matter potential will interfere constructively and destructively.

Table 5.1: The conditions under which dispersion from the neutrino halo and dispersion from the bulb neutrinos will interfere constructively or destructively. Note that the neutrino emission spectra of Ref. [8] lies in the upper right box.

	$\frac{\Phi^{\mathrm{bulb}}_{\nu_{\mathrm{e}}}\langle E^2_{\nu_{\mathrm{e}}}\rangle^{\mathrm{bulb}}}{\Phi^{\mathrm{bulb}}_{\bar{\nu}_{\mathrm{e}}}\langle E^2_{\bar{\nu}_{\mathrm{e}}}\rangle^{\mathrm{bulb}}} > 1$	$\frac{\Phi^{\mathrm{bulb}}_{\nu_{\mathrm{e}}}\langle E^2_{\nu_{\mathrm{e}}}\rangle^{\mathrm{bulb}}}{\Phi^{\mathrm{bulb}}_{\bar{\nu}_{\mathrm{e}}}\langle E^2_{\bar{\nu}_{\mathrm{e}}}\rangle^{\mathrm{bulb}}} < 1$
$\frac{\Phi^{\mathrm{bulb}}_{\nu_{\mathrm{e}}}}{\Phi^{\mathrm{bulb}}_{\bar{\nu}_{\mathrm{e}}}} > 1$	Constructive	Destructive
$\frac{\Phi^{\mathrm{bulb}}_{\nu_{\mathrm{e}}}}{\Phi^{\mathrm{bulb}}_{\bar{\nu}_{\mathrm{e}}}} < 1$	Destructive	Constructive

Table 5.2: The conditions under which dispersion from the neutrino halo and dispersion from the matter potential will interfere constructively or destructively. Note that the neutrino emission spectra and matter potential of Ref. [8] lies in the upper right box.

	$\frac{\Phi^{\mathrm{bulb}}_{\nu_{\mathrm{e}}}\langle E^2_{\nu_{\mathrm{e}}}\rangle^{\mathrm{bulb}}}{\Phi^{\mathrm{bulb}}_{\bar{\nu}_{\mathrm{e}}}\langle E^2_{\bar{\nu}_{\mathrm{e}}}\rangle^{\mathrm{bulb}}} > 1$	$\frac{\Phi^{\mathrm{bulb}}_{\nu_{\mathrm{e}}}\langle E^2_{\nu_{\mathrm{e}}}\rangle^{\mathrm{bulb}}}{\Phi^{\mathrm{bulb}}_{\bar{\nu}_{\mathrm{e}}}\langle E^2_{\bar{\nu}_{\mathrm{e}}}\rangle^{\mathrm{bulb}}} < 1$
$n_{\mathrm{e}^-} > n_{\mathrm{e}^+}$	Constructive	Destructive
$n_{\mathrm{e}^-} < n_{\mathrm{e}^+}$	Destructive	Constructive

5.2.5 Compounding Unknowns

We have repeated the analyses of Refs. [8, 104], essentially to illustrate the range of possible outcomes for a linearized stability analysis. I employ the neutrino emission spectra outlined in these papers, and use the analytic fit the authors suggest for their matter density profile at a time snapshot of 280 ms post core bounce. I also follow the convention of Ref. [104] by considering halo neutrinos which originate from within the a given radial coordinate to be co-evolving in physical and flavor space with the bulb neutrinos.

Results of performing the linearized stability analysis under several different sets of assumed conditions are shown in Figure 5.5. The physical interpretation of the information shown in Figure 5.5 is that when the density profile (shown in black) passes through the $\kappa r \geq 1$ isosurface (shown in color), the flavor states of the bulb neutrinos become unstable, and large scale collective neutrino flavor transformation can begin.

For a narrow range of conditions, where there is no appreciable phase averaging of halo neutrino flavor states and the matter in the supernova envelope is

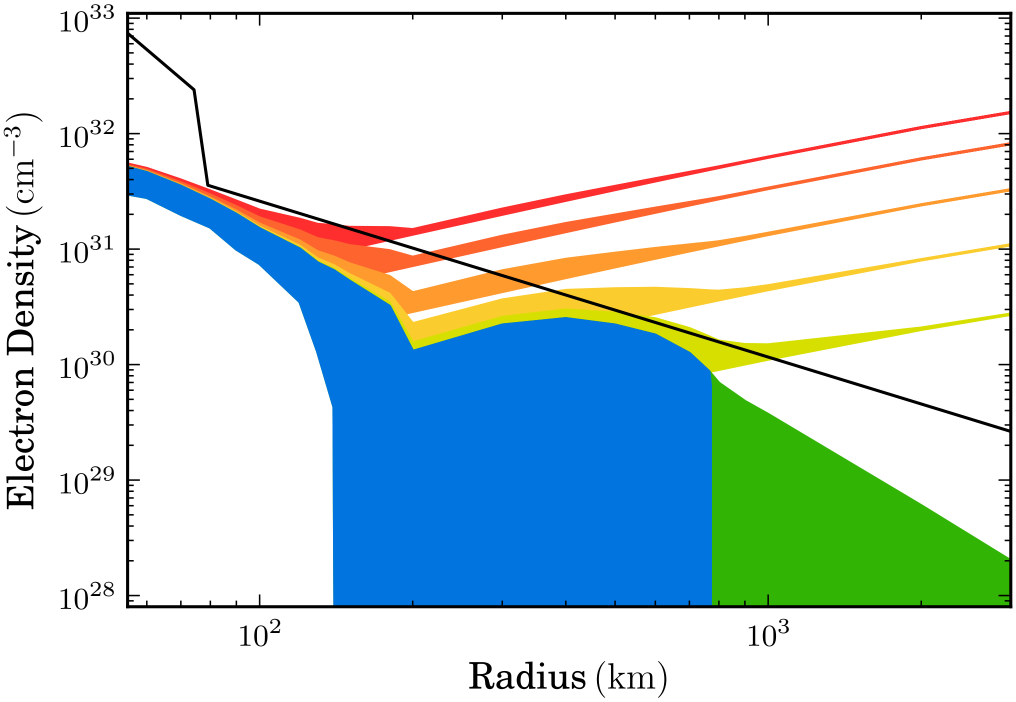

Figure 5.5: (Color Online) The isosurfaces for $\kappa r \geq 1$ using the density profile (shown in black) and neutrino emission spectra of Ref. [8]. The halo neutrinos originating inside the current radial coordinate are considered to be co-evolving with neutrinos from the core. Red: $\langle A \rangle = 56$, Blood Orange: $\langle A \rangle = 28$, Orange: $\langle A \rangle = 12$, Tangerine: $\langle A \rangle = 4$, Yellow: $\langle A \rangle = 1$, Green: $\langle A \rangle = 1$ with no halo neutrinos propagating backwards in radial coordinate, Blue: no halo potential.

assumed to be free nucleons and electrons, our results agree with those found in Refs. [8, 104] in the absence of the neutrino halo (blue) and when I exclude from the analysis halo neutrinos propagating inward (green).

However, with the neutrino emission parameters used in Ref. [8], the neutrino halo potential will interfere *destructively* with the dispersion contributions from both the bulb neutrinos and the matter potential. Moreover, all of the effects discussed at the beginning of this paper have been left out of the analysis in Ref. [104], and these have varying effects on the dispersion contribution of the halo potential.

The effect of including the dispersion from halo neutrinos propagating inward is shown in yellow, where the average nuclear mass number is taken to be $\langle A \rangle = 1$. Bulb neutrino flavor states, using this analysis, seemingly are found to become unstable at $r \sim 600\,\mathrm{km}$. This is in contrast to the results in Ref. [104], which were taken to imply generic suppression of collective neutrino flavor oscillations throughout the accretion phase.

Also shown in Figure 5.5 are the $\kappa r \geq 1$ isosurface contours when the matter outside the shock is taken to have $\langle A \rangle$ typical of the composition in the various burning shells that may be accreting through the shock. The dispersion created by the neutrino halo in these cases is so strong that the instability region may be pushed back as far as $r \sim 150\,\mathrm{km}$. Interestingly, our calculations show that the halo potential itself can create enough dispersion to suppress instability, at least when matter density is below some critical value.

There is a further complication which cannot be explicitly shown in Figure 5.5, and that is the effect of phase averaging. Because the linearized stability analysis contains no method for solving for the flavor evolution of neutrinos propagating inward, there is no way to gauge the effect of phase averaging on the total neutrino halo potential. The phase averaging must be considered as an unknown free parameter that contributes an overall multiplicative pre-factor to $\mathbf{H}_{\nu\nu}^{\mathrm{halo}}$. This pre-factor may be anywhere between 0 and 1 and may also vary with radius. This means that the isosurfaces shown in Figure 5.5 cannot be taken literally, and may in reality be distorted along a seemingly arbitrary deformation between a hotter color contour (depending on the appropriate value of $\langle A \rangle$ for a given time) and the blue contour (where phase averaging removes the halo potential entirely).

Ultimately there is a final difficulty associated with interpreting the outcome of the linearized stability analysis. If it is found that the bulb neutrinos do undergo collective flavor oscillations, this discovery immediately invalidates the initial conditions on halo neutrino flavor states that have been used to conduct the analysis. If there is any collective flavor oscillation deep within the envelope, this will change the flavor states of any neutrinos which scatter into the halo. This in turn changes the effect that the halo potential will have on the flavor state stability of bulb neutrinos all the way down to the neutrinosphere. Initial value formulations of neutrino flavor transformation, such as the linearized stability analysis, completely omit this physics.

Attempting to include the neutrino halo in an initial value problem formalism for neutrino flavor evolution is fraught with difficulties that cannot be addressed within the context of such models. The flavor evolution of neutrinos after scattering, their coupling to matter densities and composition, and the subsequent non-linear feedback onto the flavor transformation of neutrinos deeper inside the envelope are all outside the scope of a linearized stability analysis. The breadth of physically reasonable assumptions one might make about how these phenomena might feed into the analysis show that one can make a plausible case for both the suppression and enhancement of collective neutrino oscillations during the accretion and SASI phases of the supernova explosion.

Chapter 5, in part, is a reprint of material has appeared in Physical Review Letters, 2012 and material that will be shortly submitted to Physical Review D, 2012. Cherry, J. F.; Carlson, J.; Friedland, A.; Fuller, G. M.; Vlasenko, A., the American Physical Society, 2012. The dissertation author was the primary investigator and author of these papers.

Bibliography

[1] H. Duan, http://panda.unm.edu/∼duan/research/neutrino_oscillations/index.html.

[2] K. Nomoto, Astrophys. J. **277**, 791 (1984).

[3] K. Nomoto, Astrophys. J. **322**, 206 (1987).

[4] C. Lunardini, B. Müller and H. Janka, Phys. Rev. D **78**, 023016 (2008), [0712.3000].

[5] T. Fischer, S. C. Whitehouse, A. Mezzacappa, F.-K. Thielemann and M. Liebendörfer, Astronomy and Astrophysics **517**, A80 (2010), [0908.1871].

[6] H. Duan, G. M. Fuller, J. Carlson and Y. Qian, Phys. Rev. D **74**, 105014 (2006), [arXiv:astro-ph/0606616].

[7] S. W. Bruenn, A. Mezzacappa, W. R. Hix, J. M. Blondin, P. Marronetti, O. E. B. Messer, C. J. Dirk and S. Yoshida, Mechanisms of Core-Collapse Supernovae: Simulation Results from the CHIMERA Code, in *American Institute of Physics Conference Series*, edited by G. Giobbi, A. Tornambe, G. Raimondo, M. Limongi, L. A. Antonelli, N. Menci, & E. Brocato, , American Institute of Physics Conference Series Vol. 1111, pp. 593–601, 2009, [1002.4909].

[8] S. Sarikas, G. G. Raffelt, L. Hüdepohl and H.-T. Janka, Physical Review Letters **108**, 061101 (2012), [1109.3601].

[9] H. A. Bethe, G. E. Brown, J. Applegate and J. M. Lattimer, Nuclear Physics A **324**, 487 (1979).

[10] H. A. Bethe, J. H. Applegate and G. E. Brown, Astrophys. J. **241**, 343 (1980).

[11] H. A. Bethe and J. R. Wilson, Astrophys. J. **295**, 14 (1985).

[12] J. M. Blondin, A. Mezzacappa and C. DeMarino, Astrophys. J. **584**, 971 (2003), [arXiv:astro-ph/0210634].

[13] S. Chandrasekhar, Reviews of Modern Physics **56**, 137 (1984).

[14] D. L. Tubbs and D. N. Schramm, Astrophys. J. **201**, 467 (1975).

[15] M. Liebendörfer, M. Rampp, H.-T. Janka and A. Mezzacappa, Astrophys. J. **620**, 840 (2005), [arXiv:astro-ph/0310662].

[16] W. D. Arnett, Astrophys. J. **218**, 815 (1977).

[17] R. Bowers and J. R. Wilson, Astrophys. J. **263**, 366 (1982).

[18] H. A. Bethe and J. R. Wilson, Astrophys. J. **295**, 14 (1985).

[19] J. M. Blondin and A. Mezzacappa, Nature **445**, 58 (2007), [arXiv:astro-ph/0611680].

[20] L. Scheck, H.-T. Janka, T. Foglizzo and K. Kifonidis, Astronomy and Astrophysics **477**, 931 (2008), [0704.3001].

[21] T. D. Brandt, A. Burrows, C. D. Ott and E. Livne, Astrophys. J. **728**, 8 (2011), [1009.4654].

[22] A. Arcones, H.-T. Janka and L. Scheck, Astronomy and Astrophysics **467**, 1227 (2007), [arXiv:astro-ph/0612582].

[23] N. J. Hammer, H. Janka and E. Müller, Astrophys. J. **714**, 1371 (2010), [0908.3474].

[24] G. M. Fuller, R. W. Mayle, J. R. Wilson and D. N. Schramm, Astrophys. J. **322**, 795 (1987).

[25] G. M. Fuller, R. Mayle, B. S. Meyer and J. R. Wilson, Astrophys. J. **389**, 517 (1992).

[26] A. B. Balantekin and G. M. Fuller, Physics Letters B **471**, 195 (2000), [arXiv:hep-ph/9908465].

[27] S. Pastor, G. Raffelt and D. V. Semikoz, Phys. Rev. D **65**, 053011 (2002), [arXiv:hep-ph/0109035].

[28] A. B. Balantekin and H. Yüksel, New Journal of Physics **7**, 51 (2005), [arXiv:astro-ph/0411159].

[29] H. Duan, G. M. Fuller, J. Carlson and Y. Qian, Physical Review Letters **97**, 241101 (2006), [arXiv:astro-ph/0608050].

[30] S. Hannestad, G. G. Raffelt, G. Sigl and Y. Y. Y. Wong, Phys. Rev. D **74**, 105010 (2006), [arXiv:astro-ph/0608695].

[31] G. M. Fuller and Y. Qian, Phys. Rev. D **73**, 023004 (2006), [arXiv:astro-ph/0505240].

[32] H. Duan, G. M. Fuller and Y. Qian, Phys. Rev. D **74**, 123004 (2006), [arXiv:astro-ph/0511275].

[33] H. Duan, G. M. Fuller and Y. Qian, Phys. Rev. D **76**, 085013 (2007), [0706.4293].

[34] H. Duan, G. M. Fuller, J. Carlson and Y. Qian, Phys. Rev. D **75**, 125005 (2007), [arXiv:astro-ph/0703776].

[35] H. Duan, G. M. Fuller, J. Carlson and Y. Qian, Physical Review Letters **99**, 241802 (2007), [0707.0290].

[36] A. Friedland and A. Gruzinov, ArXiv Astrophysics e-prints (2006), [arXiv:astro-ph/0607244].

[37] A. Esteban-Pretel, S. Pastor, R. Tomàs, G. G. Raffelt and G. Sigl, Phys. Rev. D **76**, 125018 (2007), [0706.2498].

[38] A. B. Balantekin and Y. Pehlivan, Journal of Physics G Nuclear Physics **34**, 47 (2007), [arXiv:astro-ph/0607527].

[39] G. Fogli, E. Lisi, A. Marrone and A. Mirizzi, Journal of Cosmology and Astro-Particle Physics **12**, 10 (2007), [0707.1998].

[40] H. Duan, G. M. Fuller, J. Carlson and Y. Qian, Physical Review Letters **100**, 021101 (2008), [0710.1271].

[41] H. Duan, G. M. Fuller and J. Carlson, Comput. Sci. Dis. **1**, 015007 (2008), [0803.3650].

[42] H. Duan, G. M. Fuller and Y. Qian, Phys. Rev. D **77**, 085016 (2008), [0801.1363].

[43] B. Dasgupta, A. Dighe, G. G. Raffelt and A. Y. Smirnov, Physical Review Letters **103**, 051105 (2009), [0904.3542].

[44] J. F. Cherry, G. M. Fuller, J. Carlson, H. Duan and Y. Qian, Phys. Rev. D **82**, 085025 (2010), [1006.2175].

[45] J. F. Cherry, M.-R. Wu, J. Carlson, H. Duan, G. M. Fuller and Y.-Z. Qian, Phys. Rev. D **84**, 105034 (2011), [1108.4064].

[46] H. Duan, G. M. Fuller and Y.-Z. Qian, Annual Review of Nuclear and Particle Science **60**, 569 (2010), [1001.2799].

[47] H. Duan and A. Friedland, Physical Review Letters **106**, 091101 (2011), [1006.2359].

[48] Y. Pehlivan, A. B. Balantekin, T. Kajino and T. Yoshida, Phys. Rev. D **84**, 065008 (2011), [1105.1182].

[49] A. Banerjee, A. Dighe and G. Raffelt, Phys. Rev. D **84**, 053013 (2011), [1107.2308].

[50] B. Dasgupta, E. P. O'Connor and C. D. Ott, ArXiv e-prints (2011), [1106.1167].

[51] H. Duan and A. Friedland, Collective neutrino flavor phase coherence, In preparation, 2012.

[52] I. Gil-Botella and A. Rubbia, Journal of Cosmology and Astro-Particle Physics **10**, 9 (2003), [arXiv:hep-ph/0307244].

[53] J. P. Kneller, G. C. McLaughlin and J. Brockman, Phys. Rev. D **77**, 045023 (2008), [0705.3835].

[54] J. Gava, J. Kneller, C. Volpe and G. C. McLaughlin, Physical Review Letters **103**, 071101 (2009), [0902.0317].

[55] J. Kneller and C. Volpe, Phys. Rev. D **82**, 123004 (2010), [1006.0913].

[56] Y. Qian and G. M. Fuller, Phys. Rev. D **51**, 1479 (1995), [arXiv:astro-ph/9406073].

[57] A. B. Balantekin, Journal of Physics Conference Series **49**, 99 (2006), [arXiv:nucl-th/0608047].

[58] Y.-Z. Qian and G. J. Wasserburg, Phys. Rep. **442**, 237 (2007), [0708.1767].

[59] H. Ning, Y. Qian and B. S. Meyer, Astrophys. J.l **667**, L159 (2007), [0708.1748].

[60] H. Duan, A. Friedland, G. C. McLaughlin and R. Surman, Journal of Physics G Nuclear Physics **38**, 035201 (2011), [1012.0532].

[61] J. W. Murphy and A. Burrows, Astrophys. J. **688**, 1159 (2008), [0805.3345].

[62] M. Maltoni, T. Schwetz, M. Tórtola and J. W. F. Valle, arXiv:hep-ph/0405172v6.

[63] F. P. An, J. Z. Bai, A. B. Balantekin, H. R. Band, D. Beavis, W. Beriguete, M. Bishai, S. Blyth, R. L. Brown, G. F. Cao and et al., ArXiv e-prints (2012), [1203.1669].

[64] A. Halprin, Phys. Rev. D **34**, 3462 (1986).

[65] M. T. Keil, G. G. Raffelt and H.-T. Janka, Astrophys. J. **590**, 971 (2003), [arXiv:astro-ph/0208035].

[66] R. Mayle and J. R. Wilson, Astrophys. J. **334**, 909 (1988).

[67] F. S. Kitaura, H. Janka and W. Hillebrandt, Astron. Astrophys. **450**, 345 (2006), [arXiv:astro-ph/0512065].

[68] L. Dessart, A. Burrows, E. Livne and C. D. Ott, Astrophys. J. **645**, 534 (2006), [arXiv:astro-ph/0510229].

[69] D. Nötzold and G. Raffelt, Nuclear Physics B **307**, 924 (1988).

[70] J. Pantaleone, Phys. Rev. D **46**, 510 (1992).

[71] Y. Qian, G. M. Fuller, G. J. Mathews, R. W. Mayle, J. R. Wilson and S. E. Woosley, Physical Review Letters **71**, 1965 (1993).

[72] S. Samuel, Phys. Rev. D **48**, 1462 (1993).

[73] V. A. Kostelecký and S. Samuel, Phys. Rev. D **52**, 621 (1995), [arXiv:hep-ph/9506262].

[74] S. Samuel, Phys. Rev. D **53**, 5382 (1996), [arXiv:hep-ph/9604341].

[75] S. Pastor and G. Raffelt, Physical Review Letters **89**, 191101 (2002), [arXiv:astro-ph/0207281].

[76] R. F. Sawyer, Phys. Rev. D **72**, 045003 (2005), [arXiv:hep-ph/0503013].

[77] G. Fogli, E. Lisi, A. Marrone and A. Mirizzi, Journal of Cosmology and Astro-Particle Physics **12**, 10 (2007), [0707.1998].

[78] B. Dasgupta, A. Dighe, A. Mirizzi and G. G. Raffelt, Phys. Rev. D **77**, 113007 (2008), [0801.1660].

[79] A. Friedland, ArXiv e-prints (2010), [1001.0996].

[80] A. Mezzacappa, A. C. Calder, S. W. Bruenn, J. M. Blondin, M. W. Guidry, M. R. Strayer and A. S. Umar, Astrophys. J. **495**, 911 (1998), [arXiv:astro-ph/9709188].

[81] S. Hannestad, G. G. Raffelt, G. Sigl and Y. Y. Y. Wong, Phys. Rev. D **74**, 105010 (2006), [arXiv:astro-ph/0608695].

[82] Daya Bay Collaboration, ArXiv High Energy Physics - Experiment e-prints (2007), [arXiv:hep-ex/0701029].

[83] S. R. Elliott, C. E. Aalseth, M. Akashi-Ronquest, M. Amman, J. F. Amsbaugh, F. T. Avignone, Iii, H. O. Back, C. Baktash, A. S. Barabash, P. Barbeau, J. R. Beene, M. Bergevin, F. E. Bertrand, M. Boswell, V. Brudanin, W. Bugg, T. H. Burritt, Y. Chan, T. V. Cianciolo, J. Collar, R. Creswick, M. Cromaz, J. A. Detwiler, P. J. Doe, J. A. Dunmore, Y. Efremenko, V. Egorov, H. Ejiri, J. Ely, J. Esterline, H. Farach, T. Farmer, J. Fast, P. Finnerty, B. Fujikawa, V. M. Gehman, C. Greenberg, V. E. Guiseppe, K. Gusey, A. L. Hallin, R. Hazama, R. Henning, A. Hime, T. Hossbach, E. Hoppe, M. A. Howe, D. Hurley, B. Hyronimus, R. A. Johnson, M. Keillor, C. Keller, J. Kephart, M. Kidd, O. Kochetov, S. I. Konovalov, R. T. Kouzes, K. T. Lesko, L. Leviner, P. Luke, S. MacMullin, M. G. Marino, A. B. McDonald, D. Mei, H. S. Miley, A. W. Myers, M. Nomachi, B. Odom, J. Orrell, A. W. P. Poon, G. Prior, D. C. Radford, J. H. Reeves, K. Rielage, N. Riley, R. G. H. Robertson, L. Rodriguez, K. P. Rykaczewski, A. G. Schubert, T. Shima, M. Shirchenko, V. Timkin, R. Thompson, W. Tornow, C. Tull, T. D. Van Wechel, I. Vanyushin, R. L. Varner, K. Vetter, R. Warner, J. F. Wilkerson, J. M. Wouters, E. Yakushev, A. R. Young, C. Yu, V. Yumatov and Z. Yin, Journal of Physics Conference Series **173**, 012007 (2009), [0807.1741].

[84] L. M. Sehgal, Physics Letters B **162**, 370 (1985).

[85] F. J. Botella, C.-S. Lim and W. J. Marciano, Phys. Rev. D **35**, 896 (1987).

[86] B. Dasgupta, G. G. Raffelt and I. Tamborra, Phys. Rev. D **81**, 073004 (2010), [1001.5396].

[87] J. F. Cherry, http://www.cass.ucsd.edu/∼jcherry/.

[88] R. F. Sawyer, Phys. Rev. D **42**, 3908 (1990).

[89] F. N. Loreti and A. B. Balantekin, Phys. Rev. D **50**, 4762 (1994), [arXiv:nucl-th/9406003].

[90] F. N. Loreti, Y.-Z. Qian, G. M. Fuller and A. B. Balantekin, Phys. Rev. D **52**, 6664 (1995), [arXiv:astro-ph/9508106].

[91] A. B. Balantekin, J. M. Fetter and F. N. Loreti, Phys. Rev. D **54**, 3941 (1996), [arXiv:astro-ph/9604061].

[92] J. P. Kneller, ArXiv e-prints (2010), [1004.1288].

[93] W. C. Haxton, Physical Review Letters **57**, 1271 (1986).

[94] W. C. Haxton, Phys. Rev. D **35**, 2352 (1987).

[95] G. Sigl and G. Raffelt, Nuclear Physics B **406**, 423 (1993).

[96] P. Strack and A. Burrows, Phys. Rev. D **71**, 093004 (2005), [arXiv:hep-ph/0504035].

[97] A. Vlasenko and V. Cirigliano, Neutino quantum kinetic equations, In preparation, 2012.

[98] G. G. Raffelt, Astrophys. J. **561**, 890 (2001), [arXiv:astro-ph/0105250].

[99] F. S. Kitaura, H.-T. Janka and W. Hillebrandt, Astronomy and Astrophysics **450**, 345 (2006), [arXiv:astro-ph/0512065].

[100] A. Friedland, Physical Review Letters **104**, 191102 (2010), [1001.0996].

[101] M. Herant, W. Benz, W. R. Hix, C. L. Fryer and S. A. Colgate, Astrophys. J. **435**, 339 (1994), [arXiv:astro-ph/9404024].

[102] A. Burrows, J. Hayes and B. A. Fryxell, Astrophys. J. **450**, 830 (1995), [arXiv:astro-ph/9506061].

[103] A. Esteban-Pretel, A. Mirizzi, S. Pastor, R. Tomàs, G. G. Raffelt, P. D. Serpico and G. Sigl, Phys. Rev. D **78**, 085012 (2008), [0807.0659].

[104] S. Sarikas, I. Tamborra, G. Raffelt, L. Hüdepohl and H.-T. Janka, ArXiv e-prints (2012), [1204.0971].

[105] J. F. Cherry, J. Carlson, A. Friedland, G. M. Fuller and A. Vlasenko, Phys. Rev. Lett. **108**, 261104 (2012), [1203.1607].